Advances in Raw Material Industries for Sustainable Development Goals – Litvinenko (Ed)

Increasing the degree of nepheline raw materials use based on the conversion of sludge from alumina production

M.A. Gorbachev
Postgraduate student, Saint-Petersburg Mining University, Saint-Petersburg, Russia

V.M. Sizyakov
Professor, Metallurgy Department, Saint-Petersburg Mining University, Saint-Petersburg, Russia

R.V. Kurtenkov
PhD, Associate professor, Saint-Petersburg Mining University, Saint-Petersburg, Russia

I.S. Bormotov
Student, Saint-Petersburg Mining University, Saint-Petersburg, Russia

ABSTRACT: A modern approach to metallurgical production requires the implementation of technological solutions to reduce the amount of waste generated. The possibility of processing nepheline sludge into a calcareous component by means of combined conversion is proposed. The product of sludge disposal in this case is calcium carbonate, silica gel and soda solution. The developed methods for processing nepheline sludge are simple, low cost of implementation and can be carried out on typical equipment for alumina production, that will allow to diversify production. The described approach allows to increase the economic efficiency of production.

1 INTRODUCTION

Modern metallurgical production is characterized by the use of technologies that ensure the extraction of a significant amount of valuable components in the processing of ore raw materials of natural and technogenic origin. At the same time, low-value impurity components and minerals of waste rock are released into the sludge products in their original or chemically modified form, followed by storage in sludge storages (Lainer 1961, Eremin et al. 1980). Currently, these processes are on a global scale, which pose a serious problem for the industrial and environmental safety of existing enterprises and adjacent territories. This problem is especially acute in relation to the processing of aluminum-containing raw materials (ElDeeb et al. 2019, Sizyakov et al. 2016, Brichkin et al. 2019). For example, in the processing of bauxite per 1 ton of the final product (aluminum), at least 2 tons of waste sludge is formed, and in the processing of nepheline, this amount is already 12 or more tons, depending on the quality of the feedstock. The existing integrated method of processing nepheline into alumina and associated products allows the disposal of nepheline sludge in the production of cement and cementitious components, however, in the current situation in the market of building materials and the economic inexpediency of transporting cement over long distances leads to the accumulation of solid waste in sludge storages Figure 1.

Thus, it is of interest to develop a cost-effective technology aimed at separating the calcareous component into an independent product with its subsequent application in the alumina production cycle, obtaining products of the carboaluminate series for the chemical industry and the production of materials with high added value.

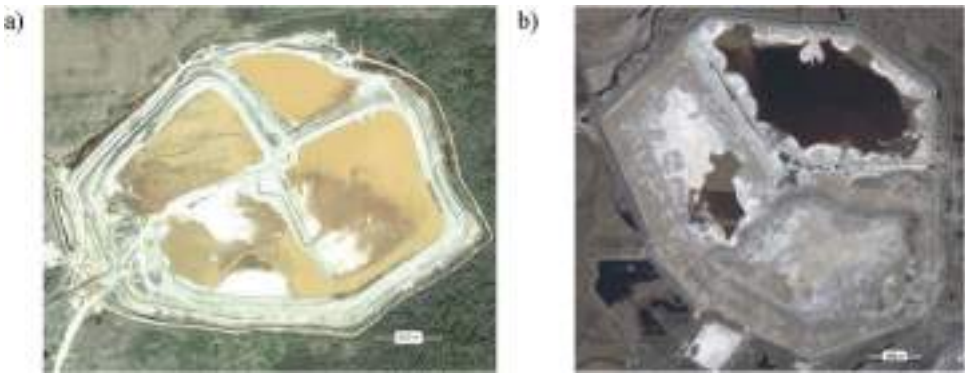

Figure 1. Sludge storage facilities for alumina refineries in Pikalevo (a) and Achinsk (b).

2 MATERIALS AND RESEARCH METHODS

Nepheline sludge is a multicomponent system, the composition of which depends on the chemical interactions during sintering, leaching of nepheline concentrate and subsequent washing, the chemical composition of the sludge is presented in Table 1. The solid waste obtained during production has a physical density of 3150-3200 kg/m3, bulk density in the range of 1000-1500 kg/m3. According to its mineralogical composition, it is 80% composed of β-modification of dicalcium silicate (belite).

In the works of P.I. Bozhenov (Bozhenov & Kavalerova 1966), the dependence of the activity of dicalcium silicate C_2S in the nepheline sludge on the alkaline module (molar ratio R_2O:Al_2O_3) of the nepheline-limestone charge was determined. This dependence is shown in Figure 2.

Thus, taking into account the production requirements for the alkaline module of the nepheline-limestone charge, it can be concluded that the activity obtained at the Russian production facilities of nepheline sludge is in the optimal region for its processing. At the same time, it should be remembered that in the production of alumina from nepheline, one of the key tasks of sintering is the binding of silicon to dicalcium silicate in the form of a low-active β-modification (β-C_2S). In turn, α-modification is more preferable and would greatly simplify the processing of sludge due to its activity, but this solution is not practical, since it will lead to significant contamination of aluminate solutions during leaching, and additional heat treatment of the sludge to transfer dicalcium silicate from β-modification to the α-modification is economically disadvantageous, since it requires heating the material. Therefore, comprehensive approaches to hydrochemical treatment are needed, which make it possible to utilize nepheline sludge without additional heat treatment.

The fundamental possibility of the soda-carbon dioxide conversion of nepheline sludge to calcium carbonate and the separation of silicon in the form of a silicate solution was previously shown and are associated with the thermodynamic instability of calcium silicates formed under high-temperature sintering processes in relation to hydration, hydrolysis, and ion exchange (Abramov et al. 1990, Shmorgunenko & Korneev 1982). Soda and carbon dioxide conversion is characterized by the following stoichiometric ratios, respectively:

$$Ca_2SiO_4 + 2Na_2CO_3 = 2CaCO_3 + Na_4SiO_4, \quad (1)$$

Table 1. The chemical composition of nepheline sludge,% (mass.) (Abramov et al. 1990).

Refinery	Loss on calcination	SiO_2	Al_2O_3	Fe_2O_3	CaO	R_2O	Others
Pikalevo	2,6	29,6	2,6	3,0	56,8	1,8	3,6
Achinsk	3,4	28,8	4,2	3,6	54,6	2,6	2,8

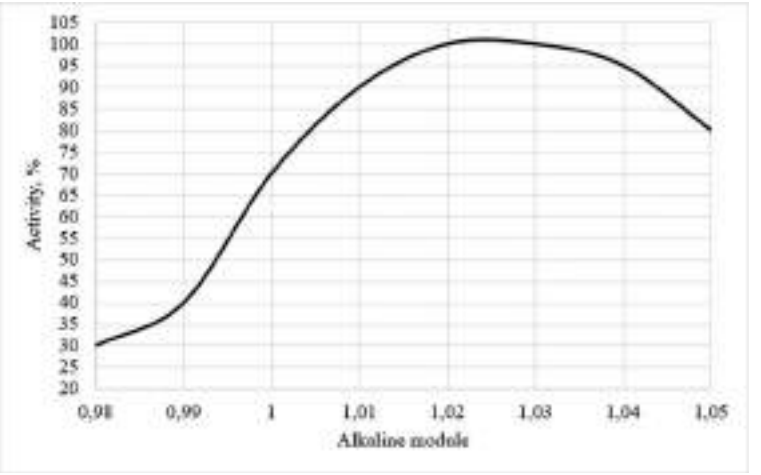

Figure 2. The dependence of the activity of C_2S in nepheline sludge on the alkaline module of charge.

$$Ca_2SiO_4 + 2Na_2CO_3 + H_2O = 2CaCO_3 + Na_2SiO_3 + 2NaOH, \quad (2)$$

$$2CaO \cdot SiO_2 + 2CO_2 = 2(CaO \cdot CO_2) + 2SiO_2. \quad (3)$$

However, the proposed methods and technical solutions do not allow a high degree of conversion and can be used mainly to obtain a single-component cement mixture, which necessitates further studies aimed at achieving the conversion of belite in the composition of nepheline sludge to 95-100%, and increasing the efficiency and the complexity of its processing.

The main indicators of the soda conversion of nepheline sludge were determined in laboratory conditions using a factory sample of a nepheline sludge of an average composition and synthetic soda solutions. The chemical composition is presented in Table 1.

3 EXPERIMENTAL

The methodology for experimental research includes the preparation of synthetic solutions of soda, repulpation of nepheline sludge with a soda solution with a given concentration (from 52,5-233,8 g/l) at a constant concentration of solid in the pulp, corresponding to Liquid: Solid=1÷10. The conversion was carried out in a single reactor AutoLAB system for 0,5-6 hours. After completion of the process, the pulp was filtered off on a laboratory vacuum filter to obtain technological products. The liquid phase was analyzed for the content of total and caustic alkali by the titrimetric method in accordance with the accepted industry method and silicon dioxide by the photometric method. The degree of conversion was calculated by determining the carbonate carbon content in solid products by spectral analysis using a TOC-L analyzer.

During the experiment, the influence of various technological factors on the soda leaching of unmilled nepheline sludge (processing time, soda solution concentration) was studied. Graphic processing of the results of the study at the indicators of soda conversion of unmilled nepheline sludge L:S=10, process temperature 50-95 ℃, the concentration of soda solution 52,5-233.8 g/l, is presented in Figures 3, 4.

The results obtained suggest that the temperature and concentration of soda solution are factors that have a significant effect on the change in the phase and chemical composition of the products. The dependence of the degree of conversion on the concentration of soda solution reflects the effects of stoichiometric, kinetic and thermodynamic nature. The shape of the kinetic curves suggests a noticeable diffusion inhibition of the conversion of belite, presumably due to

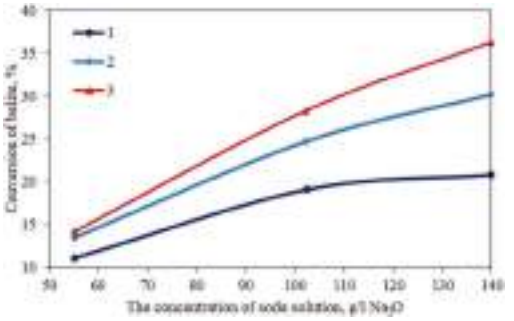

Figure 3. Effect of soda solution concentration on the decomposition of unmilled sludge at various temperatures: 1 - 50 ℃, 2 - 75 ℃, 3 - 95 ℃.

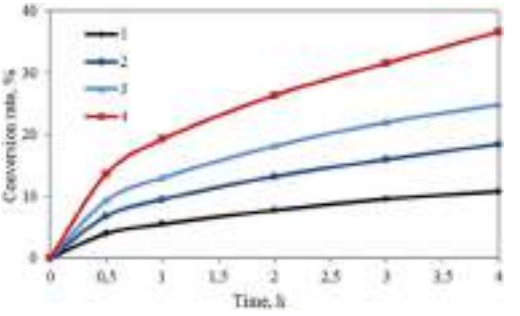

Figure 4. Kinetics of soda conversion of unmilled nepheline sludge at a temperature of 95 ℃ and a concentration of Na_2CO_3: 1 - 52,5 g/l, 2 - 110,3 g/l; 3 - 187,1 g/l; 4 - 233,8 g/l.

the formation of solid products on the surface of the initial solid phase. The calculated values of the Pilling-Bedwards test for conversion products by reactions (1) and (2) are 1,27 and 1,33, which also indicates the possibility of the formation of stable passivating films.

To intensify the conversion process and achieve higher values, an experiment was carried out for a three-stage hydrochemical treatment of nepheline sludge based on the transition to the region of pearsonite ($Na_2CO_3 \cdot CaCO_3 \cdot 2H_2O$) formation using soda solutions with a Na_2O concentration of more than 220 g/l according to the reaction:

$$CaCO_3 + Na_2CO_3 + 2H_2O = Na_2CO_3 \cdot CaCO_3 \cdot 2H_2O \quad (4)$$

To carry out the research, a laboratory setup based on the AutoLAB single-reactor system was assembled (Figure 5). The experimental design is shown in Figure 6.

The selection of technological parameters and processing methods was carried out on the basis of the analysis of scientific and technical literature in the field of processing of nepheline

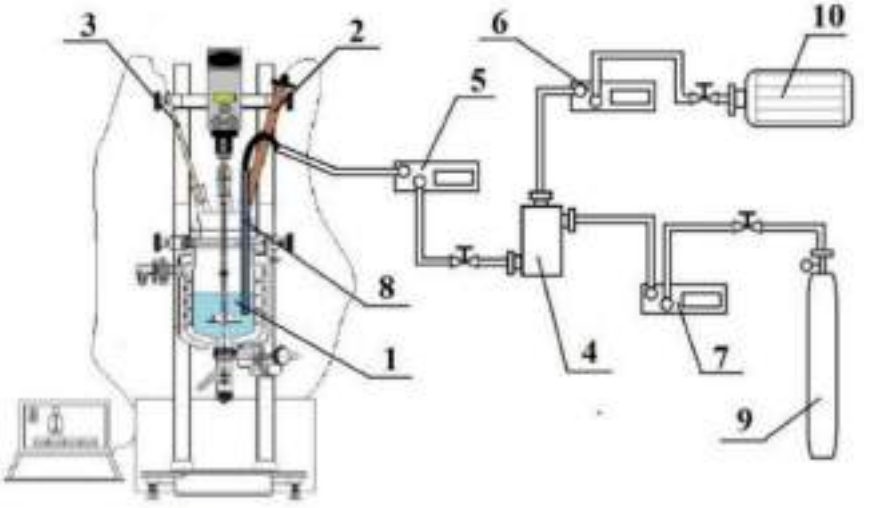

Figure 5. Scheme of a laboratory setup for a three-stage hydrochemical treatment. 1 - steel reactor 2,0 l. Single reactor AutoLab system (HEL); 2- pH electrode; 3 - temperature sensor; 4 - gas mixer; 5, 6, 7 - gas meter RGS-1; 8 - gas supply pipe; 9 - a cylinder with technical carbon dioxide; 10 – compressor.

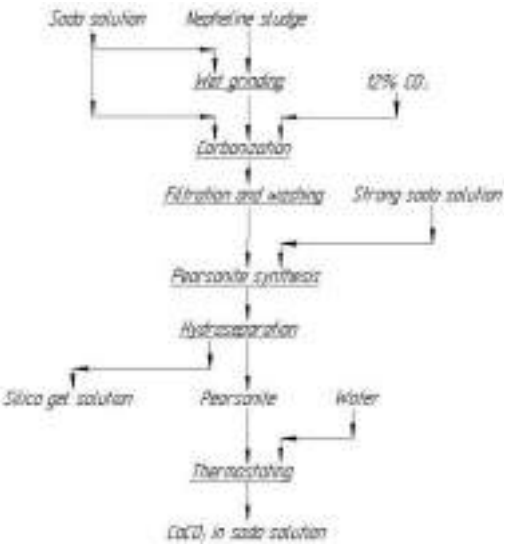

Figure 6. Scheme of the experiment.

and its sludges. In order to intensify the decomposition process, mechanical activation of nepheline sludge particles in a ball mill Pulverisette 6 (Fritsch) is built into the beginning of the scheme. As a result of the action of the balls and soda solution, the particles of the sludge are destroyed (hence, the increase in the reaction surface) and the process of its decomposition by reaction 1 begins. Wet grinding was carried out with the ratio L:S=1. After grinding, the size of the sludge corresponded to the residue on a sieve of 80 μm - 5-6%. The concentration of soda solution during grinding was 120 g/l N_2O. After grinding, the suspension was brought with a soda solution with a concentration of 120 g/l Na_2O to the ratio L:S=10 in pulp and was sent for further carbonization at a temperature of 85 ℃ for 5 hours. The composition of the gas phase corresponded to 12% vol. CO_2, the flow rate of the gas mixture was maintained at 2.0 l/min. At this stage, the formation of the first pearsonite crystals, which subsequently at the stage of synthesis, act as seeds.

Due to inactivity of stale nepheline sludge, it was determined that a precondition for the creation of a working scheme is pearsonite transformation, i.e. transition of the calcareous component to the double carbonate salt state according to reaction 4. The main reason for this solution is the need to separate the calcareous component from the silica gel solution. For this, at the second stage, the obtained slurry after washing was subjected to additional treatment with a strong soda solution with a concentration of 220 g/l Na_2O for 6 hours at L:S=4 and a temperature of 90 ℃. Due to this operation, the synthesis of pearsonite in the field of its stable state is carried out. Then, the resulting pulp was separated on a laboratory vacuum filter and the solid phase was washed.

The third stage of the experiment consisted in thermostating of the solid residue in water to go into the region of metastable state of pearsonite and its decomposition to produce calcium carbonate and soda solution.

According to the results of the experiment, the resulting material was analyzed for inorganic carbon using a TOC-L analyzer. The calculated degree of conversion was 72%, a rather low rate is associated with incomplete decomposition of sludge, however, it shows the possibility of their processing by the considered method. Additional confirmation that during the conversion of nepheline sludge decomposes pearsonite with the formation of calcium carbonate and alkali is the result of a titrimetric analysis of the solution after filtration to total alkali which showed an alkali content of 130 g/l.

4 CONCLUSION

The results showed the fundamental possibility of modifying nepheline sludges to produce a calcareous component. Further research should be aimed at studying the influence of the parameters of mechanochemical activation of nepheline sludge, the processes of carbonization and synthesis of pearsonite to achieve a degree of nepheline sludge conversion at the level of 95-100%. Presumably, an increase in the concentration of soda solution and the time of the carbonization process will increase the degree of decomposition of nepheline sludge due to a deeper hydrochemical preparation for the synthesis of pearsonite. The gas mixture used in the experiment in terms of carbon dioxide content is similar to the composition of the exhaust gases from sintering furnaces, which reduces the emission of carbon dioxide into the environment.

The application of this approach allows to increase the economic efficiency of the technology by obtaining new products, as well as reducing the cost of measures to protect the environment from the effects of industrial wastes.

ACKNOWLEDGMENTS

The study was carried out with the financial support of the Ministry of Education and Science of the Russian Federation (registration number of the project 11.4098.2017/ПЧ of 01.01.2017).

REFERENCES

Abramov, V.Y. & Alekseev, A.I. & Badalyants, Ch.A. 1990. Complex processing of apatite-nepheline raw materials. Moscow: Metallurgy.

Bozhenov, P.I. & Kavalerova, V.I. 1966. Nepheline sludges. Moscow: Stroyizdat.

Brichkin, V.N. & Kurtenkov, R.V. & ElDeeb, A.B. & Bormotov, I.S. 2019. State and development options for the raw material base of aluminium in non-bauxite regions. Obogashchenie Rud 4: 31–37. St.-Petersburg: Ore&Metals.

ElDeeb, A.B. & Brichkin, V.N. & Kurtenkov, R.V. & Bormotov, I.S. 2019. Extraction of alumina from kaolin by a combination of Pyro- and hydrometallurgical Processes. Applied Clay Science 172: 146–154. Amsterdam: Elsevier Science Publishing Company, inc.

Eremin, N.I. & Naumchik, A.N. & Kazakov, V.G. 1980. Processes and apparatuses of alumina production. Moscow: Metallurgy.

Lainer A.I. 1961. Alumina production. Moscow: Metallurgy.

Shmorgunenko N.S. & Korneev V.I. 1982. Complex processing and use of slime dump alumina production, Moscow: Metallurgy.

Sizyakov, V.M. & Brichkin, V.N. & Kurtenkov, R.V. 2016. Increasing all-round utilization of nepheline raw materials through belite sludge soda conversion. Obogashchenie Rud 1: 54–59. St.-Petersburg: Ore&Metals.

Advances in Raw Material Industries for Sustainable Development Goals – Litvinenko (Ed)

Development of methods for calculating non-stationary heat transfer between multilayer structures

A. Gorshkov
Saint Petersburg State University of Industrial Technologies and Design, Saint Petersburg, Russia

A. Demidov
Rector, Saint Petersburg State University of Industrial Technologies and Design, Saint Petersburg, Russia

A. Makarov
Vice-Rector of Science, Saint Petersburg State University of Industrial Technologies and Design, Saint Petersburg, Russia

ABSTRACT: When solving various problems of heat transfer between multilayer structures separating physical media with different temperature characteristics, various heat exchangers or devices are used (Gorshkov et al., 2018; Korniyenko et al., 2016; Gorshkov et al., 2015). Examples of heat exchange devices may include a heater and various heat utilization appliances. In real operating conditions of multilayer structures separating media with different temperatures, the heat transfer behaviour through their boundaries is almost always unsteady (Gorshkov et al., 2014; Grinfeldi et al., 2014; Vatin et al., 2014). However, for the overwhelming majority of practical problems, as a rule, a quasi-stationary heat transfer mode is considered, characterized by the time constancy of the heat flux through the structure. The quasi-stationary heat transfer mode can only be established in very short time intervals. The convenience of such a mode of heat transfer is stipulated by the fact that when considering it, all thermotechnical calculations that are used in design practice are greatly simplified (Gorshkov et al., 2013a; Gorshkov et al., 2013b; Zimin et al., 2013). Unsteady heat transfer also occurs when solving problems of heating and cooling objects, damping temperature fluctuations in structures and some others. However, their practical use is often happens to be limited.

1 INTRODUCTION

To solve a number of practical problems of heat transfer between multilayer structures separating physical media with different temperature characteristics, the existing calculation methods have a number of significant inconveniences. For example, when considering a structure of several layers, differing in temperature characteristics, in order to determine the temperature fields at each boundary of the corresponding layer, it becomes necessary to merge solutions, which leads to unnecessary complication of calculations (Gorshkov et al., 2013c; Romanova et al., 2007; Romanova et al., 2005a). Moreover, the direct input from each layer is often far from obvious. There are also known problems with the setting of boundary conditions, and the constructions of some formulas when solving problems of unsteady heat transfer are so voluminous that their use for engineering calculations is difficult (Romanova et al., 2005b; Perevoznikov et al., 2004; Gorshkov et al., 2003). In the stationary mode of heat transfer, the equations and calculation methods are greatly simplified, however the reserves of energy saving when considering them, especially when considering multilayer rather massive material structures, are largely exhausted. In this respect at the present stage of the development of constructional thermal physics, reserves of energy savings should be sought with considering

engineering problems in the non-stationary heat transfer mode (Makarov et al., 2015). Therefore, the search for optimal solutions with considering modes of non-stationary heat transfer is relevant when creating engineering calculation methods. The authors propose a description of the processes of heat transfer through multilayer structures in a non-stationary mode in the terms of the transport theory (Makarov et al., 2016).

2 DEVELOPMENT OF A METHODOLOGY FOR SOLVING PROBLEMS OF NON-STATIONARY HEAT TRANSFER

The process of heat transfer from the standpoint of the theory of transport can be considered as the diffusion of an additive scalar property - thermal energy. Let the heat transfer be carried out along some axis Ox. Since thermal energy propagates both along and against the Ox axis, it is expedient to introduce the corresponding heat flow densities $q_{\leftrightarrow}(x,t)$ as a local characteristic which can be considered as vectors in two-dimensional space As one of the local characteristics of the medium we can introduce the rate of propagation of thermal energy c (x) (Pereborova et al., 2018e; Makarov et al., 2018a; Pereborova et al., 2019).

It is obvious that the heat current density - $q(x,t) = q_{\rightarrow}(x,t) + q \quad (x,t)$. The transferred part of the internal energy can be interpreted as a nonequilibrium phonon gas, diffusing in a general way by different mechanisms. The density of the transferred part of the energy - $U(x,t) = 1/c \cdot [q_{\rightarrow}(x,t) + q \quad (x,t)]$. Moreover, it can be assumed that $U = c_v \rho T$ where c_v – specific heat, ρ – local density of the medium, $T(x,t)$- desired temperature field $(dU = c_v \rho dT)\leftarrow$ (Demidov et al., 2006a; Demidov et al., 2006b; Demidov et al., 2007a).

From the general view of the theory of transport, the spread of the additive property is determined not only by the property itself, but also by the properties of one-dimensional space, which we will call the medium. The characteristics of the medium can be determined by the distribution of other properties (for example, moisture transfer, mechanical loads, etc.), and they can also depend (in the general case, nonlinearly) on the distribution of the studied property itself (thermal energy) (Stalevich et al., 2003; Makarov et al., 2002; Stalevich et al., 2002a).

Let us consider a section of the Ox axis - $[x_1; x_2]$, which we will call a layer of the medium. Let us assume that a heat current $[x_1; x_2]$ "falls" on the layer $q_0(x_1 - 0, t)$. First we consider the case when $q_0 = \delta(t' - t)$, where t' - current time, t - fixed point in time. Let us introduce the following characteristics of the medium layer (Stalevich et al., 2002b; Stalevich et al., 2000):

- transmission coefficient - $\Lambda(t, x_1 | x_2, \tau) = q_{\rightarrow}(x_2 - 0, t + \tau)$ - heat current density passing through the layer $(x_1; x_2)$ in time τ; it is being understood that outside the boundaries of the layer $[x_1; x_2]$ there are screens completely absorbing heat;
- reflection coefficient - $\mathrm{P}(t, x_1 | x_2, \tau) = q \quad (x_1 + 0, t + \tau)$ - the density of the heat current reflected from the layer $(x_1; x_2)$ in time τ; i.e, the first reflection without a preceding crossing boundaries $x = x_1$ and $x = x_2$ earlier;
- absorption coefficient - $R(t, x_1 | x_2, \tau)$ - heat current absorbed (born) in the layer $(x_1; x_2)$ in time $(t + \tau)$.

Note that the introduced coefficients and the currents themselves $q_{\leftrightarrow}$ will be considered complex numbers (in terms of multichannel theory the coefficients Λ, P, R will be square matrices). The absorption coefficient R introduced above does not imply that there are permanent sources (leaks) of heat in the medium. By the heat source we understand the generation of heat energy U at the moment $t > t_0$, if it was absent before, and the interval is completely limited by screens. The introduction of the properties of absorbing, reflecting, semitransparent screens has a simple meaning and serves only as a way of visual description (Pereborova et al., 2020a).

All coefficients (distributions) Λ, P, R are assumed to be zero for $\tau \prec 0$ (principle of causality). For distributions Λ, P, R we can compose recurrence relations.

In the most general case in terms of the ring $R_{\overline{\otimes}}$ [4] these relations have the form:

$$\begin{aligned}
&\Lambda(x_1|x_3) = \Lambda(x_1|x_2)\overline{\otimes}[\delta - \mathrm{P}(x_2|x_3)\overline{\otimes}\mathrm{P}(x_2|x_1)]^{\overline{\otimes}-1}\overline{\otimes}\Lambda(x_2|x_3),\\
&\mathrm{P}(x_1|x_3) = \mathrm{P}(x_1|x_2) + \Lambda(x_1|x_2)\overline{\otimes}[\delta - \mathrm{P}(x_2|x_3)\overline{\otimes}\mathrm{P}(x_2|x_1)]^{\overline{\otimes}-1}\overline{\otimes}\mathrm{P}(x_2|x_3)\overline{\otimes}\Lambda(x_2|x_1),\\
&R(x_1|x_3) = R(x_1|x_2) + \Lambda(x_1|x_2)\overline{\otimes}[\delta - \mathrm{P}(x_2|x_3)\otimes\mathrm{P}(x_2|x_1)]^{\otimes-1}\overline{\otimes}\\
&\overline{\otimes}[\mathrm{P}(x_2|x_3)\otimes R(x_2|x_1) + R(x_2|x_3)]
\end{aligned} \tag{1}$$

The mathematical apparatus is based on non-commutative multiplication. To clarify the introduced symbols let us consider the set of functions $C_{t,\tau}$ of two real variables t and τ, which are definite and piecewise continuous for $\tau \geq 0$ and analytic with respect to the variable $t \in (-\infty; +\infty)$ (Pereborova et al., 2020b).

Let $a(t,\tau),\ b(t,\tau),\ c(t,\tau) \in C_{t,\tau}$ Let us define the product of functions in the form:

$$c(t,\tau) = a(t,\tau)\overline{\otimes}b(t,\tau) \stackrel{Def}{=} \int_0^{\tau} a(t,\tau_1)b(t+\tau_1, \tau-\tau_1)d\tau_1 \tag{2}$$

Let us denote $R_{\overline{\otimes}}$ - the ring of functions $C_{t,\tau}$ with natural definite addition and multiplication in the sense of (2).

Let us see an ordered sequence of functions $a, b, c\ldots \in R_{\overline{\otimes}}$. In some problems $a(t,\tau)$ can be interpreted as a distribution function of some event A, that started at time t and distributed over the duration of the event $\tau \geq 0$. In this case, we will call the above sequence of functions a process consisting of sequential execution of events $A, B, C, \ldots$.

The need to use a ring $R_{\overline{\otimes}}$ means that most of the natural phenomena around us are some ordered chains of certain events (Pereborova et al., 2020c).

In the simplest case if $a, b, c, \ldots$ do not depend on a variable t expressly (for example, the start time of an event), then integral (2) represents the usual convolution of functions, i.e. $c(\tau) = a(\tau) * b(\tau)$. Consequently, $R_* \subset R_{\overline{\otimes}}$. To describe specific processes, it is more convenient to use not the ring $R_{\overline{\otimes}}$, itself, but the ring $R_{\overline{\otimes}}$. Isomorphism between rings $R_{\overline{\otimes}}$ and $R_{\overline{\otimes}}$ is determined using the Laplace transformation

$$A(t,S) = \int_0^{\infty} a(t,\tau)e^{-S\tau}d\tau \tag{3}$$

where $A(t,S)$ - analytic function in both variables (real t and complex S) (Pereborova et al., 2020d).

We define the product of functions $A(t,S) \otimes B(t,S) = C(t,S); A, B, C \in R_{\otimes}$, describing the multiplicative semigroup of the ring $R_{\otimes}$ as follows:

$$C(t,S) \stackrel{Def}{=} \sum_{n=0}^{\infty} \frac{(-1)^n}{n!} \cdot \frac{\partial^n A(t,S)}{\partial S^n} \cdot \frac{\partial^n B(t,S)}{\partial t^n} = A(t,S) \otimes B(t,S) \tag{4}$$

The associativity of the ring $R_{\otimes}$ follows from the associativity of the ring $R_{\overline{\otimes}}$. Multiplication in the sense of (3) is associated with addition due to the laws of distributivity. $R_{\otimes}$ - a ring with a unit element, while the unit element of the ring $R_{\otimes}$ is the function $E(t,S) \equiv 1$.

We will consider the physical meaning of equations (1) using the example of the first equation of this system. Event - the passage of a heat carrier (phonon) through the layer $[x_1; x_3]$ is possible only by crossing the imaginary boundary an odd number of times (Pereborova et al., 2018a).

Then, according to theorems on addition and multiplication of probabilities for distributions, we have

$$\begin{aligned}
&\Lambda(t,x_1|x_2,\tau)=\int\limits_0^{\tau}\Lambda(t,x_1|x_2,\tau_1)\cdot\Lambda(t+\tau_1,x_2|x_3,\tau-\tau_1)+\\
&+\Lambda(x_1|x_2)\overline{\otimes}\mathrm{P}(x_2|x_3)\overline{\otimes}\mathrm{P}(x_2|x_1)\overline{\otimes}\Lambda(x_2|x_3)+\ldots=\\
&=\Lambda(x_1|x_2)\overline{\otimes}[\delta-\mathrm{P}(x_2|x_3)\overline{\otimes}\mathrm{P}(x_2|x_1)]^{\overline{\otimes}-1}\overline{\otimes}\Lambda(x_2|x_3)
\end{aligned}\tag{5}$$

Instead of distributing Λ, P, R it is advisable to immediately use their Laplace images, that is $\overline{\Lambda}, \overline{\mathrm{P}}, \overline{R}$. In this case, instead of the symbol $\overline{\otimes}$ it is necessary to use multiplication $\otimes$ in the sense of (4) (Makarov et al., 2018b).

The theory of transfer formulates the transition from one ring to another in the form of the "non-stationary principle". The essence of it is as follows. Let some additive quantity M, that has no structure be described by coefficients $\bar{\Lambda}, \bar{\mathrm{P}}, \bar{R}$, and one with a structure - by analogous elements $\widetilde{\Lambda}, \widetilde{\mathrm{P}}, \widetilde{R}$, while $\widetilde{\Lambda}, \widetilde{\mathrm{P}}, \widetilde{R}$ belong to a more complex ring R_0. Then the transition from the description of the propagation of the property M to the description of the propagation of the property $\widetilde{M}$ is reduced to replacing the operation $\otimes$ with the operation of multiplication and replacing 1 by the unit element of the ring R_0 without changing the form of equations (Pereborova et al., 2019a; Pereborova et al., 2018b; Makarov et al., 2014a). In other words, system (1) is also valid for the multichannel case with the corresponding substitution of symbols.

Accordingly, in a general way, system (1) will take the form:

$$\begin{aligned}
&\overline{\Lambda}(x_1,t|x_3,S)=\overline{\Lambda}(x_1|x_2)\otimes\left[I-\overline{\mathrm{P}}(x_2|x_3)\otimes\overline{\mathrm{P}}(x_2|x_1)\right]^{\otimes-1}\otimes\widetilde{\Lambda}(x_2|x_3)\\
&\overline{\mathrm{P}}(x_1,t|x_3,S)=\overline{\mathrm{P}}(x_1|x_2)+\overline{\Lambda}(x_1|x_2)\otimes\left[I-\overline{\mathrm{P}}(x_2|x_3)\overline{\otimes}\overline{\mathrm{P}}(x_2|x_1)\right]^{\otimes-1}\otimes\\
&\otimes\overline{\mathrm{P}}(x_2|x_3)\otimes\Lambda(x_2|x_1)\\
&\overline{R}(x_1,t|x_3,S)=\overline{R}(x_1|x_2)+\overline{\Lambda}(x_1|x_2)\otimes\left[I-\overline{\mathrm{P}}(x_2|x_3)\otimes\overline{\mathrm{P}}(x_2|x_1)\right]^{\otimes-1}\otimes\\
&\otimes\left[\overline{\mathrm{P}}(x_2|x_3)\otimes\overline{R}(x_2|x_1)+\overline{R}(x_2|x_3)\right]
\end{aligned}\tag{6}$$

The relations (6) make it possible to successively determine the properties of a system of layers, with knowing the properties of each layer, i.e. give a constructive way to solve the problems of heat transfer (Demidov et al., 2006c).

The non-commutativity of the rings $R_{\overline{\otimes}}$ and $R_{\otimes}$ is essential for strongly non-stationary processes, when the properties of the medium change over the mean time of heat passage, i.e., each time the "wandering" phonon enters a new medium. If all the coefficients do not depend on time t explicitly or this dependence can be neglected, then the multiplication "$\otimes$" is an ordinary multiplication, i.e.

$$\begin{aligned}
&\overline{\Lambda}(x_1|x_3,S)=\frac{\overline{\Lambda}(x_1|x_2)\overline{\Lambda}(x_2|x_3)}{1-\overline{\mathrm{P}}(x_2|x_3)\overline{\mathrm{P}}(x_2|x_1)}\\
&\overline{\mathrm{P}}(x_1|x_3,S)=\overline{\mathrm{P}}(x_1|x_2)+\frac{\overline{\Lambda}(x_1|x_2)\overline{\Lambda}(x_2|x_1)\overline{\mathrm{P}}(x_2|x_3)}{1-\overline{\mathrm{P}}(x_2|x_3)\overline{\mathrm{P}}(x_2|x_1)}\\
&\overline{R}(x_1|x_3,S)=\overline{R}(x_1|x_2)+\frac{\overline{\Lambda}(x_1|x_2)\left[\overline{\mathrm{P}}(x_2|x_3)\overline{R}(x_2|x_1)+\overline{R}(x_2|x_3)\right]}{1-\overline{\mathrm{P}}(x_2|x_3)\overline{\mathrm{P}}(x_2|x_1)}
\end{aligned}\tag{7}$$

Non-commutativity is also essential in those cases when the medium is inhomogeneous or there are inclusions in the medium layer. In this case, it is necessary to introduce the concept of a propagation channel and all coefficients $\overline{\Lambda}, \overline{\mathrm{P}}, \overline{R}$ are square matrices. In reality, Fourier's law is rather approximate and functions well only for the stationary case. This is explained by the fact that heat transfer even in a homogeneous medium does not follow just one mechanism (there are also internal heat transfer channels) (Rymkevich et al., 2013).

The existence of several mechanisms of heat conduction leads to a slightly different system of equations describing the process of heat transfer (Pereborova et al., 2019b; Pereborova et al., 2018c; Pereborova et al., 2018d).

For the majority of engineering calculations all these "subtleties" may be disregarded and the above relations (7) can be used.

The described method of heat transfer makes it possible to establish correlations between energy densities (i.e., temperature) and heat currents at different points in space. Indeed, let us consider the two-point identity for heat fluxes. Given $x = x_1$ we know the heat currents $q_{1\leftrightarrow}(S)$Let us define these heat currents at an arbitrary point x_2 (for greater certainty let it be $x_2 > x_1$).

Using the developed method, we have:

$$\begin{aligned}
&\overline{q_{\rightarrow}}(x_2|S) = \left[\overline{q_0}_{\rightarrow} + \overline{q_0}_{\leftarrow} \otimes \overline{\mathrm{P}}(x_1|-\infty)\right] \otimes \left[I - \overline{\mathrm{P}}(x_1|+\infty) \otimes \overline{\mathrm{P}}(x_1|-\infty)\right]^{\otimes -1} \otimes \\
&\otimes \overline{\Lambda}(x_1|x_2) \otimes \left[I - \overline{\mathrm{P}}(x_2|+\infty) \otimes \overline{\mathrm{P}}(x_2|x_1)\right]^{\otimes -1}, \\
&\overline{q_{\rightarrow}}(x_2|S) = \overline{q_{\rightarrow}}(x_2|S) \otimes \overline{\mathrm{P}}(x_2|+\infty)
\end{aligned} \tag{8}$$

It is not difficult to express currents q_1 by means of q_2. In particular, with $x_2 = x_1 = x$ we obtain a true identity that connects $\overline{\Lambda}$ and $\overline{\mathrm{P}}$ with each other. In general, by splitting a certain layer in different ways, we can get useful results, sometimes greatly simplifying the solution of specific problems. Thus, the property currents at one point in one-dimensional space completely determine the property currents for all other points. The method of accounting for multiple border crossings can be generalized to the three-dimensional case (Makarov et al., 2017b).

For continuous space, it is advisable to consider an infinitely thin layer dx. We have $\overline{\Lambda}(x|\cancel{x}) \equiv 1, \overline{\mathrm{P}}(x|x) = \overline{R}(x|x) \equiv 0$, if there are no singularities (the existing singularities will be called screens). Expanding $\overline{\mathrm{P}}(x|x \pm dx)$ and $\overline{R}(x|x \pm dx)dx > 0$ in a series and leaving the first terms of the expansion, we will have:

$$\begin{aligned}
&\overline{\mathrm{P}}(x|x \pm dx) = a(x,t)dx + 0(dx) \\
&\overline{R}(x|x \pm dx) = \chi(x,t)dx + 0(dx)
\end{aligned} \tag{9}$$

where $a(\cancel{x},t)$ and $\chi(\cancel{x},t)$ will be called reflection and absorption indices respectively. Thus, a and χ are the local characteristics of the medium in relation to the propagation of heat (Demidov et al., 2017).

Let us introduce the notion of the average time for the passage of heat by the layer Δx as follows:

$$t_{\lambda}\Delta x \overset{Def}{=} -\frac{\partial}{\partial S}\left[\ln \overline{\Lambda}(x|x+\Delta x)\right]_{S=0} \tag{10}$$

For a homogeneous medium $\overline{\Lambda}, \overline{\mathrm{P}}, \overline{R}$ have a simple form:

$$\begin{aligned}
&\overline{\Lambda}(z,S) = \frac{2\mu(S-\mu)e^{-\mu z}}{a^2 - (S-\mu)^2 e^{-2\mu z}}, \infty \\
&\overline{\mathrm{P}}(z,S) = \frac{a(S-\mu)\left[1 - e^{-2\mu z}\right]}{a^2 - (S-\mu)^2 e^{-2\mu z}}, \\
&\overline{R}(z,S) = \frac{\sqrt{2}\chi\sqrt{S-\mu}}{\sqrt{S-a}} \cdot \frac{[1 - e^{-\mu z}]}{[a + (S-\mu)e^{-\mu z}]}
\end{aligned} \tag{11}$$

Here we introduce the symbols $z = x_2 - x_1$, $\mu = \sqrt{\widetilde{S}^2 - a^2}$, $\widetilde{S} = \frac{S}{c} + (a + \chi)$.

3 NON-STATIONARY HEAT TRANSFER THROUGH MULTILAYER TEXTILES

One of the problems that arises when solving problems of unsteady heat transfer through multilayer textiles is the correct setting of the boundary conditions at the media interface. Another problem is limiting the rate of transfer of thermal energy, that is, heat is transferred with some delay (Makarov et al., 2017b). The calculations of the delay in heat transfer between textiles lead to equations of the form:

$$\begin{aligned} \tau_P \frac{\partial \overrightarrow{q}}{\partial t} + \overrightarrow{q} &= -\lambda \overrightarrow{\nabla} \overrightarrow{T} \\ \tau_P \frac{\partial^2 T}{\partial t^2} + \frac{\partial T}{\partial t} &= div[a_T \operatorname{grad} T] \end{aligned} \tag{12}$$

Here $T(x, y, z, t)$ – is the required temperature field; $\overrightarrow{q}$ - heat flux density; λ - coefficient of thermal conductivity, $a_T = \frac{\lambda}{c_V \rho}$ - coefficient of heat diffusion (coefficient of thermal diffusivity); c_V and ρ accordingly, the specific heat and density of the material; τ_P - relaxation time. The equations (12) characterize most of the heat transfer phenomena between textiles. Nevertheless, theoretical estimates show that the relaxation time τ_P for most textile materials is very short, although the empirically introduced τ_P corrects non-stationary thermal fields (Makarov et al., 2015a).

The polymeric materials that the studied textiles are composed of have a heterogeneous structure. However, even for a homogeneous medium, there is more than one heat transfer mechanism. The transferred part of the internal energy can be interpreted as a nonequilibrium phonon gas diffusing in the general case by different mechanisms (longitudinal and transverse waves) (Makarov et al., 2015b).

The process of transferring heat between textiles can be viewed as the diffusion of an additive scalar property - thermal energy with an internal structure.

Let us assume that heat energy propagates through N various mechanisms, which we will call heat propagation channels. It is the amount of heat energy on each channel that determines the structure of the heat flow. The transferred part of the internal energy $U(x, t)$ is equal to the sum of the energies on each channel (internal energy reservoirs) (Demidov et al., 2009).

$$U(x,t) = \sum_{n=1}^{N} \frac{1}{c_n} \left[q_{\overrightarrow{n}}(x,t) + q_{\overleftarrow{n}}(x,t) \right] = \sum_{n=1}^{N} \left[U_{\overrightarrow{n}}(x,t) + U_{\overleftarrow{n}}(x,t) \right] \tag{13}$$

It should be noted that $T(x, t)$ – some average temperature over a physically small volume. Since the transfer of heat is an irreversible and nonequilibrium process, it is more accurate to talk about the local temperature on each channel (the principle of local equilibrium). Therefore, in the case of non-stationary heat transfer, two physical processes take place: the first is the transfer of energy from a more heated body to a less heated one; the second is the exchange of energy between different distribution channels, i.e. relaxation processes. Part of the electromagnetic energy is absorbed according to the well-known exponential Bouguer law, i.e. passes to other channels of heat propagation (Makarov et al., 2014b).

The heat flux density $q(x, t)$ is

$$q(x,t) = \sum_{n=1}^{N} q_n(x,t) = \sum_{n=1}^{N} \left[q_{\overrightarrow{n}}(x,t) - q_{\overleftarrow{n}}(x,t) \right] \tag{14}$$

To derive the heat transfer equations generally it is sufficient to write 2N equations of continuity for the linear energy density on each channel in accordance with the law of conservation of energy (Demidov et al., 2007a).

Thereat we will have

$$\frac{\partial U_{\overrightarrow{n}}(x,t)}{\partial t} = -\frac{\partial}{\partial x}\left[U_{\overrightarrow{n}}(x,t)c_n\right] - \sum_{k=1}^{N}\left[\tilde{a}_{\overrightarrow{nk}} + \tilde{b}_{\overrightarrow{nk}}\right]U_{\overrightarrow{n}}(x,t) + \sum_{k=1}^{N}\tilde{a}_{\overleftarrow{kn}}U_{\overleftarrow{k}}(x,t) + \sum_{k=1}^{N}\tilde{b}_{\overrightarrow{kn}}U_{\overrightarrow{k}}(x,t)$$
$$\frac{\partial U_{\overleftarrow{n}}(x,t)}{\partial t} = \frac{\partial}{\partial x}\left[U_{\overleftarrow{n}}(x,t)c_n\right] - \sum_{k=1}^{N}\left[\tilde{a}_{\overleftarrow{nk}} + \tilde{b}_{\overleftarrow{nk}}\right]U_{\overleftarrow{n}}(x,t) + \sum_{k=1}^{N}\tilde{a}_{\overrightarrow{kn}}U_{\overrightarrow{k}}(x,t) + \sum_{k=1}^{N}\tilde{b}_{\overleftarrow{kn}}U_{\overleftarrow{k}}(x,t) \tag{15}$$

Here $\widetilde{a}_{nk}(x,t)\leftarrow$ is the reflection rate constant, i.e. the share of thermal energy per unit oftime that has passed from channel n to channel k with a change in the direction of propagation; $\widetilde{a}_{nk}(x,t) = \frac{\widetilde{a}_{nk}}{c_n}$ - is called the matrix element of the heat flux dissipation indicators; $\widetilde{b}_{nk}(x,t)$ - matrix of constants of transition rate from channel n to channel number k, i.e. the proportion of thermal energy per unit of time ($\widetilde{q}_{nk} \equiv 0$), that has passed from channel number n to channel number k without changing the direction of movement; the quantity $\left(\widetilde{\theta}_{nk} = \frac{\widetilde{b}_{nk}}{c_n}\right.$ is called the matrix element of the transition indicators (Demidov et al., 2007b).

The system equations express the law of conservation of energy transfer with taking into account the internal exchange between the channels. The distribution channel can also be understood as a homogeneous part of a heterogeneous system. In the absence of asymmetry: i.e. without the presence of external fields, fluxes of quantities of the same nature, etc. $\underset{nk=\leftarrow}{\widetilde{a}}_{nk=\leftarrow} = \widetilde{a}_{nk}$, $\underset{nk=\leftarrow}{\widetilde{b}}_{nk=\leftarrow} = \widetilde{b}_{nk}$.

We restrict ourselves to considering the case of a quasi-homogeneous medium whose properties do not change with time (for example, aging). Such a medium will be described by the following constants: $\widetilde{a}_{nk}$ - N^2 - quantities, $\widetilde{b}_{nk}$ - $N(N-1)$ quantities and $c_n - N$- quantities, i.e. totally $2N^2$ material characteristics. In reality there are much less of them due to the presence of equilibrium equations (Demidov et al., 2006d).

Let us rewrite system (6) in a slightly different form, adding and subtracting the equations of the system term by term, introducing the matrix elements

$$\theta_{kn} = \frac{1}{c_n}\sum_{n=1}^{N}\left[\tilde{a}_{kn} + \tilde{b}_{kn}\right]\delta_{kn} + \frac{1}{c_k}\left[\tilde{a}_{kn} - \tilde{b}_{kn}\right]$$
$$G_{kn} = \sum_{m=1}^{\infty}\left[\tilde{a}_{km} + \tilde{b}_{km}\right]\delta_{kn} - \left[\tilde{a}_{kn} + \tilde{b}_{kn}\right] \tag{16}$$

In this case, system (5) will be rewritten as follows:

$$\frac{\partial U_n}{\partial t} + \frac{\partial q_n}{\partial x} + \sum_{k=1}^{N} U_k G_{kn} = 0$$
$$\frac{1}{c_n}\frac{\partial q_n}{\partial t} + c_n\frac{\partial U_n}{\partial x} + \sum_{k=1}^{N} q_k\theta_{kn} = 0 \tag{17}$$

The first N of equations are equations of continuity with internal energy transfers from channel to channel. The second N of equations express the generalized Fourier law. From the system of equations $N = 1$ hyperbolic heat conductivity equations follow (12) (Leusheva et al., 2019).

If the thickness of the medium layer is sufficiently large, then in the stationary case (steady state) the Fourier law is fulfilled, i.e.

$$\begin{aligned} &\sum_{k=1}^{N} U_k^p G_{kn} = 0 \\ &c_n \frac{\partial U_k^p}{\partial x} + \sum_{k=1}^{N} q_k^p \theta_{kn} = 0 \end{aligned} \tag{18}$$

The index "p" means that equilibrium has been established between the channels and the principle of local equilibrium is in effect, i.e. the system has a local temperature $T(x)$ and other local characteristics. Let ω_k^p - is the fraction of thermal energy propagating through the channel number n $\left(\sum_{n=1}^{N} \omega_k^p = 1\right)$, then the system (Nikolaev et al., 2018)

$$\begin{aligned} &\sum_{k=1}^{N} \omega_k^p G_{kn} = 0 \\ &\sum_{n=1}^{N} \omega_k^p = 1 \end{aligned} \tag{19}$$

uniquely determines the value ω_k^p (Lapshin, 2014).

In addition, for such a stationary quasi-equilibrium, the principle of detailed equilibrium can be applied - the amount of energy passing from channel number k to channel n is equal to the amount of energy passing from channel n to channel number k.

This way

$$\begin{aligned} \omega_k^p \tilde{a}_{kn} &= \omega_n^p \tilde{a}_{nk} \\ \omega_k^p \tilde{b}_{kn} &= \omega_n^p \tilde{b}_{nk} \end{aligned} \tag{20}$$

that significantly reduces the number of linearly independent characteristics of the environment. In particular, for the stationary case, we have the following equality:

$$\frac{1}{a_T} c_n \omega_n^p - \omega_k^p \theta_{kn} = 0 \tag{21}$$

With additional N - constraint equations (Gryazev et al., 2017)

4 CONCLUSION

As a result, a mathematical model has been developed for calculating multilayer structures in the non-stationary heat transfer mode. In engineering problems, when assessing the energy saving potential, equations and models obtained in a stationary heat transfer mode are usually considered. The reserves of thermal energy savings for them are well studied, and their potential at the present stage of development of science in the area of knowledge under consideration is largely realized. In this regard, an additional potential for energy saving can be identified when considering the heat transfer process in a non-stationary mode.

The developed mathematical model is based on the methods of the general transport theory. An equation is obtained to determine the difference in the average transit times of a heat flux through a multilayer structure that separates media with different temperatures for

a different sequence of layers arrangements. The influence of the order of the layers on its thermal stability is shown. An expression is obtained that shows the difference in the average transit times of a heat flux through a multilayer structure with different arrangements of its layers. The obtained equations can be used, inter alia, when describing the process of heat transfer through multilayer textiles.

FUTURE RESEARCH AND ACKNOWLEDGEMENTS

The study was funded within the framework of the state assignment of the Ministry of Science and Higher Education of the Russian Federation, Project No. FSEZ-2020-0005.

REFERENCES

Demidov, A.V., Makarov, A.G., Stalevich, A.M. (2006a) Methods of computer analysis of viscoelasticity of technical materials. *Izvestiya Vysshikh Uchebnykh Zavedenii, Seriya Teknologiya Tekstil'noi Promyshlennosti*, Vol. 291, No 3, pp. 13–17. eid=2-s2.0-37849188658

Demidov, A.V., Makarov, A.G., Stalevich, A.M. (2006b) Definition of the mechanical characteristics of textile stuffs at variable temperature. *Izvestiya Vysshikh Uchebnykh Zavedenii, Seriya Teknologiya Tekstil'noi Promyshlennosti*, Vol. 291, No 3, pp. 13–17. eid=2-s2.0-37849188658

Demidov, A.V., Makarov, A.G., Stalevich, A.M. (2006c) The criteria of optimal selection of mathematical model of textile materials viscoelasticity. *Izvestiya Vysshikh Uchebnykh Zavedenii, Seriya Teknologiya Tekstil'noi Promyshlennosti*, Vol. 293, No 5, pp. 21–25. eid=2-s2.0-34247548784

Demidov, A.V., Makarov, A.G., Stalevich, A.M., Petrova, L.N., Chelishev, A.M. (2006d) Research of changes of deformation properties of polyester threads depending on twist amount. *Izvestiya Vysshikh Uchebnykh Zavedenii, Seriya Teknologiya Tekstil'noi Promyshlennosti*, Vol. 292, No 4, pp. 9–13. eid=2-s2.0-33845499474

Demidov, A.V., Makarov, A.G., Stalevich, A.M. (2007a) Definition of the computer forecasting trends of deformation properties of textile stuffs. *Izvestiya Vysshikh Uchebnykh Zavedenii, Seriya Teknologiya Tekstil'noi Promyshlennosti*, Vol. 297, No 2, pp. 14–17. eid=2-s2.0-38849203122

Demidov, A.V., Makarov, A.G., Stalevich, A.M. (2007b) Predicting the nonlinear hereditary viscoelasticity of polymers. *Journal of Applied Mechanics and Technical Physics*, Vol. 48, No 6, pp. 897–904. DOI: 10.1007/s10808-007-0114-8

Demidov, A.V., Makarov, A.G., Stalevich, A.M. (2007c) System analysis of viscoelasticity of textile stuffs. Izvestiya Vysshikh Uchebnykh Zavedenii, Seriya Teknologiya Tekstil'noi Promyshlennosti, Vol. 298, No 3, pp. 11–14. eid=2-s2.0-34648822922

Demidov, A.V., Makarov, A.G., Stalevich, A.M. (2009) A version of modeling of nonlinear-hereditary viscoelasticity of polymer materials. *Mechanics of Solids*, Vol. 44, No 1, pp. 122–130. DOI: 10.3103/S0025654409010130

Demidov, A.V., Makarov, A.G., Pereborova, N.V., Egorova, M.A. (2017) Forecasting of deformation-relaxation properties of poly amide fabric used to make the canopy. *Izvestiya Vysshikh Uchebnykh Zavedenii, Seriya Teknologiya Tekstil'noi Promyshlennosti*, Vol. 367, No 1, pp. 250–258. eid=2-s2.0-85033239149

Gorshkov, A.S. (2003) 75 years Soyuzteplostroi. *Montazhnyei Spetsial'nye Raboty v Stroitel'stve*, 9, pp. 15–19. eid=2-s2.0-0142041513

Gorshkov, A.S., Vatin, N.I. (2013a) Properties of the wall structures made of autoclaved cellular concrete products on the polyurethane foam adhesive. *Magazine of Civil Engineering*, Vol. 40, No 5, pp. 5–19. DOI: 10.5862/MCE.40.1

Gorshkov, A.S., Sokolov, N.A. (2013b) Inconsistency in Russian and international standards in the determination of the design values of thermal conductivity of building materials and products. *Magazine of Civil Engineering*, Vol. 42, No 7, pp. 7-14+78-80. DOI: 10.5862/MCE.42.2

Gorshkov, A.S., Makarov, A.G., Romanova, A.A., Rymkevich, P.P. (2013c) Modelling of directed polymers deformation processes based on the description of the kinetics of supramolecular structures separated by energy barriers. *Magazine of Civil Engineering*, Vol. 44, No 9, pp. 76-83+103-104. DOI: 10.5862/MCE.44.10

Gorshkov, A.S., Rymkevich, P.P., Vatin, N.I. (2014) Simulation of non-stationary heat transfer processes in autoclaved aerated concrete-walls. *Magazine of Civil Engineering*, Vol. 52, No 8, pp. 38-48 and 65-66. DOI: 10.5862/MCE.52.5

Gorshkov, A.S., Rymkevich, P.P. (2015) A diagram method of describing the process of non-stationary heat transfer. *Magazine of Civil Engineering*, Vol. 60, No 8, pp. 68–82. DOI: 10.5862/MCE.60.8

Gorshkov, A.S., Vatin, N.I., Rymkevich, P.P., Kydrevich, O.O. (2018) Payback period of investments in energy saving. *Magazine of Civil Engineering*, Vol. 78, No 2, pp. 65–75. DOI: 10.18720/MCE.78.5

Grinfeldi, G.I., Gorshkov, A.S., Vatin, N.I. (2014) Tests results strength and thermophysical properties of aerated concrete block wall samples with the use of polyurethane adhesive. *Advanced Materials Research*, 941-944, pp. 786–799. DOI: 10.4028/www.scientific.net/AMR.941-944.786

Gryazev, M.V., Kachurin, N.M. and Vorob'ev, S.A. (2017) Mathematical models of gas-dynamic and thermophysical processes in underground coal mining at different stages of mine development. *Journal of Mining Institute*, 223, p. 99. DOI: 10.18454/pmi.2017.1.99.

Korniyenko, S.V., Vatin, N.I., Gorshkov, A.S. (2016) Thermophysical field testing of residential buildings made of autoclaved aerated concrete blocks. *Magazine of Civil Engineering*, Vol. 64, No 4, pp. 10–25. DOI: 10.5862/MCE.64.2

Lapshin, A. A. (2014) "Mathematical modeling of mine air conditioning in the zone of mine works", *Journal of Mining Institute*, 210, p. 53. Available at: http://pmi.spmi.ru/index.php/pmi/article/view/5265 (Accessed: 18 August 2020).

Leusheva, Ekaterina & Morenov, Valentin & Martel, A.S. (2019). Combined cooling heat and power supplying scheme for oil and gas fields development. 10.1201/9780429327070-53.

Makarov, A.G. (2002) Determining the analytical correlation between the standardized nuclei of relaxation and creep in textile materials. *Izvestiya Vysshikh Uchebnykh Zavedenii, Seriya Teknologiya Tekstil'noi Promyshlennosti*, Vol. 266, No 2, pp. 13–17. eid=2-s2.0-0036931214

Makarov, A.G., Pereborova, N.V., Egorova, M.A., Wagner, V.I. (2014a) Modeling and forecasting viscoelastic properties of textile materials with a complex structure. *Izvestiya Vysshikh Uchebnykh Zavedenii, Seriya Teknologiya Tekstil'noi Promyshlennosti*, Vol. 354, No 6, pp. 120–124. eid=2-s2.0-84937439497

Makarov, A.G., Pereborova, N.V., Egorova, M.A., Wagner, M.A. (2014b) Ways of modeling deformation and relaxation properties of textile materials with a complex structure. *Izvestiya Vysshikh Uchebnykh Zavedenii, Seriya Teknologiya Tekstil'noi Promyshlennosti*, Vol. 351, No 3, pp. 110–115. eid=2-s2.0-84937410003

Makarov, A.G., Demidov, A.V., Pereborova, N.V., Egorova, M.A. (2015a) Modeling and prediction of estimated relaxation and deformation properties of the polymer parachute line. *Izvestiya Vysshikh Uchebnykh Zavedenii, Seriya Teknologiya Tekstil'noi Promyshlennosti*, Vol. 360, No 6, pp. 194–205. eid=2-s2.0-84976560627

Makarov, A.G., Pereborova, N.V., Wagner, V.I., Vasileva, E.K. (2015b) Development of methodology for the comparative analysis of deformation and relaxation properties of aramid yarns and textile materials based on them. *Izvestiya Vysshikh Uchebnykh Zavedenii, Seriya Teknologiya Tekstil'noi Promyshlennosti*, Vol. 359, No 5, pp. 48–58. eid=2-s2.0-84971636036

Makarov, A.G., Slutsker, G.Y., Drobotun, N.V. (2015c) Creep and fracture kinetics of polymers. *Technical Physics*, Vol. 60, No 2, pp. 240–245. DOI: 10.1134/S1063784215020152

Makarov, A.G., Slutsker, G.Y., Gofman, I.V., Vasil'eva, V.V. (2016) Initial stage of stress relaxation in oriented polymers. *Physics of the Solid State*, Vol. 58, No 4, pp. 840–846. DOI: 10.1134/S1063783416040132

Makarov, A.G., Pereborova, N.V., Egorova, M.A., Egorov, I.M. (2017a) Quality analysis of deformation-relaxation properties of aramid cords mountain rescue appointments. *Izvestiya Vysshikh Uchebnykh Zavedenii, Seriya Teknologiya Tekstil'noi Promyshlennosti*, Vol. 368, No 2, pp. 309–313. eid=2-s2.0-85035207042

Makarov, A.G., Pereborova, N.V., Egorova, M.A., Egorov, I.M. (2017b) Mathematical modeling of deformation-relaxation processes polymeric materials in conditions of variable temperatures. *Izvestiya Vysshikh Uchebnykh Zavedenii, Seriya Teknologiya Tekstil'noi Promyshlennosti*, Vol. 370, No 4, pp. 287–292. eid=2-s2.0-85057142312

Makarov, A.G., Pereborova, N.V., Vagner, V.I., Egorova, M.A., Klimova, N.S. (2018a) Spectral Analysis of Viscoelastic Creep of Geotextiles. *Fibrie Chemistry*, Vol. 50, No 4, pp. 378–382. DOI 10.1007/s10692-019-09993-4

Makarov A.G., Pereborova N.V., Kozlov A.A., Shvankin A.M. (2018b) Computer-Assisted Prediction and Qualitative Analysis for Polymer Parachute Cords. *Fibre Chemistry*, Vol. 50, No. 3, pp. 239–242. DOI 10.1007/s10692-018-9968-1

Nikolaev, A & Dokoukin, V & Lykov, Yuri & Fetisov, Vadym. (2018). Research of processes of heat exchange in horizontal pipeline. *IOP Conference Series: Materials Science and Engineering*. 327. 032041. 10.1088/1757-899X/327/3/032041.

Pereborova N.V., Demidov A.V., Makarov A.G., Klimova N.S. (2018a) Modeling of Deformation-Relaxation Processes of Aramid Textile Materials – the Foundation for Analyzing Their Operational Properties. *Fibre Chemistry*, Vol. 50, No. 2, pp. 104–107. DOI 10.1007/s10692-018-9941-z

Pereborova, N.V., Makarov, A.G., Egorova, M.A., Kozlov, A.A., Konovalov, A.S. (2018b) Methods of simulation and comparative analysis of shadow and deformation-reducing properties of aramide textile materials. *Izvestiya Vysshikh Uchebnykh Zavedenii, Seriya Teknologiya Tekstil'noi Promyshlennosti*, Vol. 375, No 3, pp. 253–257. eid=2-s2.0-85059766891

Pereborova, N.V., Makarov, A.G., Egorova, M.A., Klimova, N.S. (2018c) Methods of increasing the competitiveness of domestic aramid textile materials based on complex analysis of their functional properties. Izvestiya Vysshikh Uchebnykh Zavedenii, Seriya Teknologiya Tekstil'noi Promyshlennosti, Vol. 378, No 6, pp. 267–272. eid=2-s2.0-85072335464

Pereborova, N.V., Demidov, A.V., Makarov, A.G., Klimova, N.S., Vasileva, E.K. (2018d) Methods of mathematical modeling and qualitative analysis of relaxation-deformation processes of aramide textile materials. *zvestiya Vysshikh Uchebnykh Zavedenii, Seriya Teknologiya Tekstil'noi Promyshlennosti*, Vol. 374, No 2, pp. 251-255. eid=2-s2.0-85056451197

Pereborova, N.V., Makarov, A.G., Kozlov, A.A., Vasil'eva, E.K. (2018e) Development of Integral Optimality Criteria for Mathematical Modeling of Relaxation/Recovery Processes in Polymer Textile Materials. *Fibrie Chemistry*, Vol. 50, No 4, pp. 306–309. DOI 10.1007/s10692-019-09981-8

Pereborova N.V., Makarov A.G., Vasil'eva E.K., Shvankin A.M., Egorov I.M. (2019a) Mathematical Modeling and Computed Prediction of Viscoelastic Creep in Geotextile Nonwoven Fabrics. *Fibre Chemistry*, Vol. 50, No 6, pp. 487–490. DOI 10.1007/s10692-019-10015-6

Pereborova N.V., Makarov A.G., Egorova M.A., Klimova N.S. (2019b) Improving the Competitiveness of Aramid Textile Materials Based on Mathematical Modeling and Analysis of Their Performance Properties. *Fibre Chemistry*, Vol. 50, No 6, p. 569–572. DOI 10.1007/s10692-019-10030-7

Pereborova, N.V., Makarov, A.G., Egorova, M.A., Kozlov, A.A. (2019c) Mathematical Modeling and Comparative Analysis of Deformation/Recovery Properties and Shrinkage of Aramid Textile Materials. *Fibre Chemistry*, Vol. 50, No 5, pp. 468–472. DOI 10.1007/s10692-019-10010-x

Pereborova, N.V., Makarov, A.G., Shvankin, A.M., Egorova, M.A., Abramova, I.V. (2020a) Modeling and Qualitative Analysis of Creep Processes of Geotextile Nonwovens -A Foundation for Enhancing their Competitiveness. *Fibre Chemistry*, Vol. 51 No. 5, pp. 397–400. DOI 10.1007/s10692-020-10119-4

Pereborova, N.V., Makarov, A.G., Shvankin, A.M., Egorova, M.A., Korobovtseva, A.A. (2020b) Predicting Creep and Deformation and Recovery Processes of Geotextile Nonwovens. *Fibre Chemistry*, Vol. 51, No. 5, pp. 401–403. DOI 10.1007/s10692-020-10120-x

Pereborova, N.V., Makarov,A.G., Egorova,M.A., Egorov,I.M. (2020c) Methods of Modeling and Computer-Aided Prediction of Relaxation of Medical-Purpose Textile Elastomers. *Fibre Chemistry*, Vol. 51, No. 6, pp.467–470. DOI 10.1007/s10692-020-10136-3

Pereborova, N.V.,Makarov,A.G., Egorova,M.A., Egorov,I.M. (2020d) Methods modeling and Computer-Aided Prediction of Strain and Relaxation Processes of Medical-Purpose Textile Elastomers. *Fibre Chemistry*, Vol. 51, No. 6, pp.471–474. DOI 10.1007/s10692-020-10137-2

Perevoznikov, E.N., Gorshkov, A.S. (2004) Amplitude modulation mechanism of the free longitudinal vibrations in stressed filament yarns. *Izvestiya Vysshikh Uchebnykh Zavedenii, Seriya Teknologiya Tekstil'noi Promyshlennosti*, Vol. 280, No 5, pp. 73–76. eid=2-s2.0–19344363321

Romanova, A.A., Rymkevich, P.P., Gorshkov, A.S., Stalevich, A.M. (2005a) Dynamic relaxation of synthetic fibres. *Khimicheskie Volokna*, No 4, pp. 44–46. eid=2-s2.0-29144510616

Romanova, A.A., Rymkevich, P.P., Gorshkov, A.S., Stalevich, A.M. (2005b) Dynamic relaxation of synthetic fibres. *Fibre Chemistry*, Vol. 37, No 4, pp. 289–292. DOI: 10.1007/s10692-005-0097-2

Romanova, A.A., Rymkevich, P.P., Gorshkov, A.S., Stalevich, A.M. (2007) Young relaxing modulus of synthetic threads. *Izvestiya Vysshikh Uchebnykh Zavedenii, Seriya Teknologiya Tekstil'noi Promyshlennosti*, Vol. 299, No 4, pp. 3–5. eid=2-s2.0-36148930530

Rymkevich, P.P., Romanova, A.A., Golovina, V.V., Makarov, A.G. (2013) The energy barriers model for the physical description of the viscoelasticity of synthetic polymers: Application to the uniaxial orientational drawing of polyamide films. *Journal of Macromolecular Science, Part B: Physics*, Vol. 52, No 12, pp. 1829–1847. DOI: 10.1080/00222348.2013.808906

Stalevich, A.M., Makarov, A.G. (2000) Determining the inherent viscoelastic relaxation spectrum for synthetic filaments. *Izvestiya Vysshikh Uchebnykh Zavedenii, Seriya Teknologiya Tekstil'noi Promyshlennosti*, Vol. 255, No 3, pp. 8–12. eid=2-s2.0-0034436083

Stalevich, A.M., Makarov, A.G. (2002a) Forecasting the deformation recovery process and the reverse relaxation in polymer materials. *Izvestiya Vysshikh Uchebnykh Zavedenii, Seriya Teknologiya Tekstil'noi Promyshlennosti*, Vol. 268, No 4-5, pp. 15–18. eid=2-s2.0-0037742684

Stalevich, A.M., Makarov, A.G., Saidov, E.D. (2002b) Elastic components in the stress/strain curve for a synthetic fibre yarn. *IzvestiyaVysshikh Uchebnykh Zavedenii, Seriya Teknologiya Tekstil'noi Promyshlennosti*, (4-5), pp. 15–18. eid=2-s2.0-0037742684

Stalevich, A.M., Makarov, A.G., Saidov, E.D. (2003) Relaxation spectrometry of synthetic yarns. *Izvestiya Vysshikh Uchebnykh Zavedenii, Seriya Teknologiya Tekstil'noi Promyshlennosti*, Vol. 270, No 1, pp. 16–22. eid=2-s2.0–2642532049

Vatin, N.I., Gorshkov, A.S., Nemova, D.V., Staritcyna, A.A., Tarasova, D.S. (2014) The energy-efficient heat insulation thickness for systems of hinged ventilated facades. *Advanced Materials Research*, 941-944, pp. 905–920. DOI: 10.4028

Zimin, Z.S., Orlovich, R.B., Gorshkov, A.S. (2013) Application of stones of high voidage in the facing layer of the multilayer walls. *Magazine of Civil Engineering*, Vol. 43, No 8, pp. 14-23+77-78. DOI: 10.5862/MCE.43.3

Advances in Raw Material Industries for Sustainable Development Goals – Litvinenko (Ed)
© 2021 Taylor & Francis Group, London, ISBN 978-0-367-75881-3

Effect of sintering temperature on the alumina extraction from kaolin

A.B. ElDeeb
Ph.D. student, Metallurgy Department, Saint-Petersburg Mining University, Saint-Petersburg, Russia
Assistant lecturer, Mining and petroleum department, Faculty of Engineering, Al-Azhar University in Cairo, Egypt

V.M. Sizyakov
Professor, Metallurgy Department, Saint-Petersburg Mining University, Saint-Petersburg, Russia

V.N. Brichkin
Professor, Head of Metallurgy Department, Saint-Petersburg Mining University, Saint-Petersburg, Russia

R.V. Kurtenkov
Assistant, Metallurgy Department, Saint-Petersburg Mining University, Saint-Petersburg, Russia

ABSTRACT: Solid state, phase transformation mechanism during the thermal decomposition of kaolin-limestone mixture sintered at different temperatures were investigated. The effect of sintering temperature on the phase transformation and alumina extraction efficiency were studied. Sintering of the mixture was carried out in the temperature range 800-1400°C, followed by leaching with sodium carbonate solution. Leaching was carried out under the following conditions; sodium carbonate solution concentration of 120 g/l at a temperature of 70° C for 30 minutes and at a stirring speed of 600 rpm. During sintering, kaolinite decomposes and transferred into the metakaolinite phase, which in turn reacts with the decomposed calcium carbonate and forms at a certain temperature calcium aluminate phases ($12CaO.7Al_2O_3$) that are readily soluble in sodium carbonate solution. The obtained results indicate that is the sintering temperature has a significant effect on the phase transformation and the efficiency of alumina extraction. Low sintering temperatures are not enough for the main phase transformations and the formation of readily soluble forms of calcium aluminate. It is clear that, increasing the temperature to 1360°C increases the degree of extraction of alumina in the solution to 80.49%. At the same time, the increase in the sintering temperature has a positive effect on the degree of completion of the self-disintegration process.

Keywords: alumina extraction, kaolin, solid state transformation, sintering temperature, kaolin-limestone mixture, self-disintegration process, microstructure composition

1 INTRODUCTION

Alumina is an important industrial material, which can be used as an abrasive material and as adsorbent (Salahudeen et al., 2015). Alumina has been widely used in advanced technological applications including its use for the processing of high-quality insulators (Ueki et al., 2010), semiconductors (Lee et al., 2013), microelectronics (Imanaka, 2015), high-strength materials (Lee et al., 2009), ceramics, refractories (Andrews et al., 2014), biofuel and cell-fuel (Phung et al., 2014), fireproof plastics, high-grade polishes (Lei et al., 2012), catalysts (Osman et al., 2017), electrochemical anodic oxidation (Wan et al., 2018), metal-matrix composites (Garg et al., 2019), the production of aluminum metal (Kvande, 2014) and a plurality of other uses.

The aluminum industry is one of the fastest growing global sectors in the world, especially among developing countries. Increased worldwide demand for aluminum oxide, currently at more than 160 million tons per year, is expected to lead to a gradual global decline of high-grade bauxite, the ore from which alumina is mainly produced using the Bayer process. Many aluminum-producing countries have thus become increasingly interested in the investigation of producing alumina from non bauxitic sources (ElDeeb et al., 2019, Cohen & Mercier, 2016, Protosenya & Trushko, 2007).

Low-grade bauxites and non-bauxite resources such as nepheline, coal fly ash, clays and red mud are widely distributed in the world (Brichkin, et al., 2019, ElDeeb & Brichkin, 2018, Dubovikov & Brichkin, 2016, Sizyakov & Brichkin, 2018, Sizyakov, 2005).

Clay is one of the numerous aluminous raw materials that are distributed on a large scale in the world. Among the clay group kaolin and kaolinite-based solid wastes such as coal fly ash and oil shale have attracted considerable attention for alumina extraction due to the high content of alumina in these ores (Brichkin et al., 2019, ElDeeb & Brichkin, 2018, Olaremu, 2015, Seyed, et al., 2011, Sizyakov et al., 2019, Guo et al., 2014, Lima et al., 2014, Suss et al., 2014; Xiao et al., 2015).

Among the different clays, kaolin seems to be a more attractive candidate for alumina production and an aluminum resource alternative to bauxite, due to its high aluminium content (35-38%) and the reactivity of kaolin increases after the dehydration transformation of the kaolin to amorphous metakaolinite, which is more reactive and from which alumina can be easily extracted by acidic or alkaline leaching agents (ElDeeb & Brichkin, 2018, Seyed et al., 2011).

The lime sinter process for processing clay consists of the following sequential steps: 1) mixing the ground clay and calcium carbonate in proportions to give after sintering at a suitable temperature a mixture corresponding to the composition of ($2CaO{\cdot}SiO_2$), ($12CaO{\cdot}7Al_2O_3$) and ($CaO{\cdot}Al_2O_3$) (2) leaching of the calcium aluminate compounds by dilute sodium carbonate solution to extract alumina in the form of sodium aluminate, (3) treating the sodium aluminate solution with carbon dioxide to precipitate alumina trihydrate (gibbsite) and (4) calcining the gibbsite at 1350°C to produce alumina (αAl_2O_3) phase (Al Ajeel et al., 2014, Sizyakov, 2016).

Thermal treatments at a controlled temperature range were generally applied to increase the activity of kaolin before the acidic and alkaline extraction procedure due to the low chemical reactivity of kaolinite (Sizyiakov et al., 2013). The process is generally thought to increase clay reactivity by affecting dehydration transformation of the kaolin to amorphous metakaolinite ($Al_2Si_2O_7$), which is known to be more reactive and from which alumina can be easily extracted by acidic or alkaline leaching agents (Cohen & Mercier, 2016, Sizyiakov, 2006).

In this work, the effect of sintering temperature, solid state and phase transformation mechanism on the alumina extraction efficiency from kaolin ore processed using lime-sinter process were investigated. The efficiency of the self-disintegration process as a result of the sintering process was also studied. The micro structure changes in the produced sinters and sludges due to the sintering process were investigated.

2 MATERIALS AND METHODS

The current study was carried out using kaolin ore which was obtained from Irkutsk mining site, while limestone ore sample was obtained from Pikalevo region, Russia. Chemically pure grade up to 99.8% sodium carbonate was used for the leaching process.

The chemical composition of the kaolin and limestone ores was determined using XRF-1800 sequential X-ray fluorescence spectrometer (40 kV, 90 mA, Re anode) (USA) in order to estimate the chemical composition of the raw materials and the chemical changes that took place after the sintering and the leaching processes. Structural phase analysis of the kaolin ore was carried out using a bruker D8 focus X-ray diffractometer having siemens diffractometer 7000 with Cu-Kα radiation (40 kV, 30 mA, $\lambda = 1.5406$Å) (USA).

Differential scanning calorimetry (DSC) and thermal gravimetric analysis (TGA) for kaolin-limestone mixture were investigated using simultaneous DSC-TGA instrument (SDT Q600) (USA) in the temperature range from ambient to 1300°C and heating rate of 20°C/min in the air conditions in order to clarify the thermal decomposition behavior of kaolin-limestone mixture. The particle size analysis for the produced sinter and sludge was carried out by laser microanalysis using the domestic microsizer 201C analyzer and the range of analysis was 0.2 to 600 μm.

The microstructure changes of the sintered kaolin-limestone mixture as a result of the sintering process at different temperatures and the sludge produced as a result of the subsequently leaching were characterized using a tescan TS 5130MM scanning electron microscope equipped with an X-ray energy dispersive detector (manufactured by Oxford Instruments, active crystal area - 50 MM^2) with the INCA energy microanalysis system and YAG crystal as a reflected electron detector.

The kaolin-limestone mixture was prepared according to the stoichiometric calculations on the basis of the molar ratios of oxides [CaO/SiO_2 = 2, CaO/Al_2O_3 = 1.8 and CaO/Fe_2O_3 = 1] and the prepared charge according to this stoichiometry composed of 265.8 g limestone and 100 g kaolin. These ratios provide the required phases suitable for the leaching process and the higher recovery of alumina (Al-Ajeel et al., 2014, ElDeeb et al., 2019).

The kaolin-limestone mixture was effectively mixed in a drum mixer for 4hr then formed on the form of cylindrical briquettes. Briquetting was carried out on the hydraulic press "Laptuls" using the press mould of 30 mm diameter and 30 mm height at 5 MPa briquetting pressure (ElDeeb et al., 2019). The produced briquettes was sintered in a laboratory high-temperature chamber furnace in closed air conditions in the temperature range from 800°C to 1400°C and for 1hr. In the sintering process, the briquettes were inserted in the furnace then the furnace started to heat at the predetermined temperature with a rate of 10°C/minute. After reaching the desired temperature, the duration of the isothermal holding at the given temperature was 1hr. After finishing the sintering time, the furnace was allowed to cool down to the room temperature in order to allow the sintered material to be annealed and achieve the self-disintegration process. The obtained sintered material was characterized chemically using XRF analysis in order to determine the oxides content in the produced sinter and mineralogically using XRD analysis in order to determine the new phases as a result of the sintering process at different temperatures. The microstructure changes of the sintered kaolin-limestone charge as a result of the sintering process and the sludge produced as a result of the subsequently leaching were characterized using scanning electron microscope (SEM-EDX).

The sinters obtained from the sintering process were leached using Na_2CO_3 solution. The leaching process was carried out in the HEL Auto-Mate II reactor system equipped with mechanical stirring. All leaching experiments for the produced sinter at differant temperatures were carried out under the following conditions: 70°C leaching temperature, Na_2CO_3 solution with a concentration 120 g/l solution, 1/5 solid to liquid ratio, 30 min. leaching time and 600 rpm stirring speed according to the best condition obtained before (ElDeeb et al., 2019). The produced pulp from the leaching process was filtered out using a vacuum and the obtained sludge was washed with hot distilled water then dried in the draying furnace. The obtained sludge's were analyzed chemically by XRF analysis in order to determine the oxides content in the sludge. The alumina extraction degree was calculated using the following formula: $Al_{extracted} = (Al_{sinter} - Al_{sludge})/Al_{sinter}$.

3 RESULTS AND DISCUSSION

3.1 *The physical and chemical characterization of the used raw materials*

The mineralogical analysis of the kaolin ore sample using XRD analysis shown in Figure 1, revealed that the kaolin ore composed mainly from kaolinite mineral ($Al_2O_3.2SiO_2.2H_2O$) barring aluminium oxide and silica contributions, which were also detected as quartz mineral. The chemical analysis of the kaolin ores using XRF analysis shown in Table 1 indicates that is

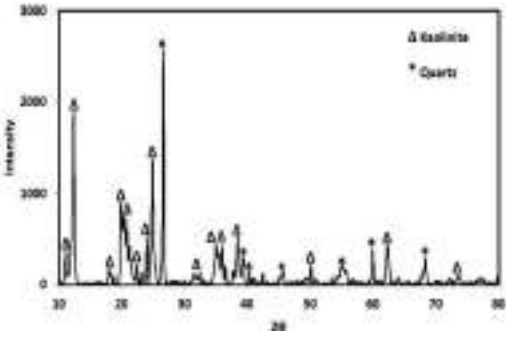

Figure 1. XRD analysis of the kaolin ore.

Table 1. The chemical analysis of the kaolin and limestone ores.

Materials	SiO_2	Al_2O_3	Fe_2O_3	TiO_2	CaO	Na_2O	K_2O	others	L.O.I
Kaolin ore	52.2	31.9	1.4	0.58	0.59	0.15	0.15	0.03	13
Limestone	2.01	0.41	0.56	0.58	53.3	-	-	-	43.14

the kaolin ore contains 31.9% Al_2O_3 and 52.2% SiO_2 which represent the main components of the kaolin ore in addition to other oxides. The loss on ignition of 13% in the chemical analysis is as a result of organic matter, some non-metals and the chemical and physical water lost. This alumina content in kaolin ore is considered as economic percentage for the extraction of alumina in comparison with bauxite ore (Brichkin et al., 2019).

The TGA and DSC analysis for the kaolin-limestone mixture is shown in Figure 2. The TGA curve of the kaolin-limestone mixture sample show three well-defined weight loss regions, the first is below 200°C and the endothermic peak in the DSC curve at 111.20°C is due to the loss of physisorbed water. The seconded weight loss region in the TGA curve is above 450°C and the endothermic peak in the DSC curve at 507.51°C is due to the dehydroxylation of coordinated and structural water with a weight loss of 3.27%. The third weight loss regions in the TGA curve is in the range (650-850°C) and the endothermic peak in the DSC curve at 844.43°C can be attributed to the complete dissociation of the limestone and the further release of CO_2 from $CaCO_3$ with a weight loss of 29.69%. Compared with the

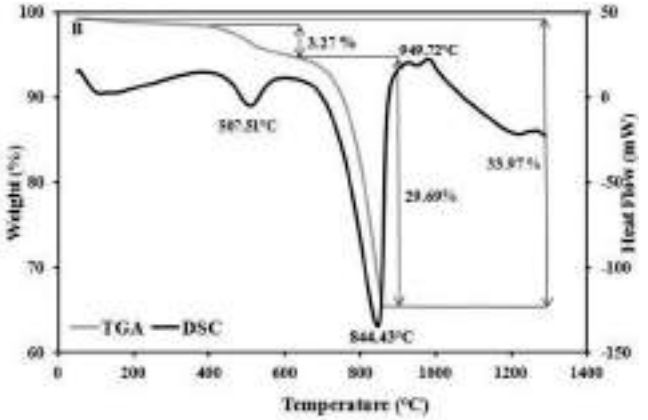

Figure 2. DSC and TGA analysis for the kaolin-limestone mixture.

decomposition temperature of pure $CaCO_3$ (650-900°C), the existence of kaolinite obviously decreased the decomposition temperature of $CaCO_3$ in the mixture, which suggested that the solid-state reaction between kaolinite and $CaCO_3$ occurred during the heating process (Tian et al., 2016, Yan et al., 2017, Zhang et al., 2015). The sharp exothermic peak at 949.52°C could be assigned to the phase transformation from metakaolinite to Al-Si spinel or mixture of γ-alumina, amorphous silica and mullite and the total weight loss is 33.97% at 1300°C (Zhang et al., 2015, ElDeeb et al., 2019). Also it is clear that the existence of calcite ($CaCO_3$) obviously decreased the phase transformation temperature from metakaolinite to Al-Si spinel or the mixture of γ-alumina, amorphous silica and mullite compared to this temperature for the TGA and DSC analysis of the kaolin ore.

3.2 *The effect of sintering temperature on the percent recovery of alumina*

The most important factor affecting on the physico-chemical transformation of the kaolin-limestone mixture and hence the extraction of alumina from kaolin ore is the sintering temperature. The effect of the sintering temperatures on the percent recovery of alumina from kaolin ore was investigated in the range from 800 to 1400°C. The obtained sinters at different sintering temperatures and the sludges as a result of the subsequently leaching of these sinters were characterized chemically using XRF analysis in order to determine the oxides content in both the sinters and sludges. The effect of the sintering temperatures on the oxides content in the sinters is shown in Figure 3A. The oxides content in the sludges produced from the subsequently leaching of the sinter is shown in Figure 3B. The chemical composition indicates that both the sinter and sludge composed mainly from the following oxides CaO, SiO_2, Al_2O_3 in addition to other oxides. The difference between the alumina content in the sinter and its content in the sludge represent the percent recovery of alumina in the solution and the alumina extraction degree was calculated using the following formula: $Al_{extracted} = (Al_{sinter} - Al_{sludge})/Al_{sinter}$ as shown in Figure 4.

It is clear that is the percent recovery of alumina increases with increasing the sintering temperature from 800 to 1360°C and then with more increasing of the sintering temperature up to

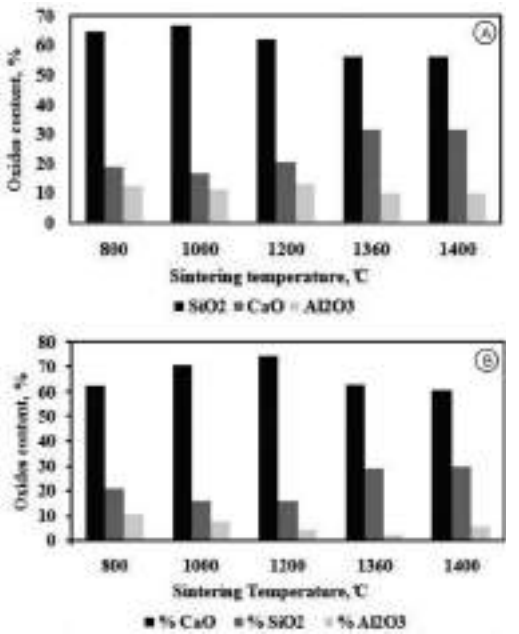

Figure 3. The effect of the sintering temperature on the oxides content obtained in a) the sintered kaolin-limestone mixture and b) the sludge produced from the leaching process.

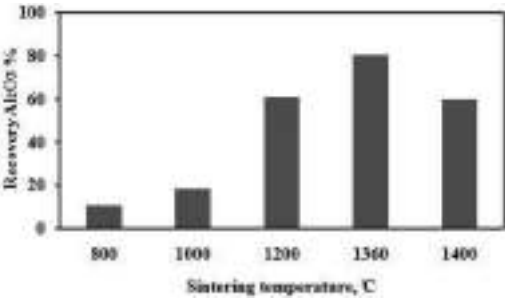

Figure 4. The effect of sintering temperature on the percent recovery of alumina.

1400°C the percent recovery of alumina decreases. The percentage recovery of alumina increases from 10.51% at 800°C to 80.49 at 1360°C then decrease to 59.70% at 1400°C. This can be attributed to that is the sintering temperature of 1360°C is the most suitable temperature for the formation of C_2S and $C_{12}A_7$ compounds in the sinter at which alumina can be extracted easily from the $C_{12}A_7$ using sodium carbonate solution. The low temperature isn't sufficient for the complete decomposition of the calcium carbonate and the formation of the C_2S and $C_{12}A_7$ compounds hence the lost of alumina in the form of Al_2SiO_5 and $Ca_2Al_2SiO_7$. On the other hand, decreasing the percent recovery of alumina with more increasing of the sintering temperature up to 1400°C can be attributed to the high temperature which leads to the formation of mullite ($Al_2O_3.SiO_2$) phase from which alumina is difficulty extracted (Qiao, et al., 2008).

3.3 *The effect of sintering temperature on the solid state and phase transformation mechanism*

The effect of the sintering temperature on the phase transformation mechanism of kaolin- limestone mixture was carried out by studying the microstructure changes in both the sinters and sludges produced at differant temperatures. The main structural components of both the sinter produced at 800°C and the sludge obtained from its subsequently leaching are shown in Figure 5. The results indicate that the main structural components in both the sinter and sludge include: relics of the original charge minerals including kaolinite and calcite. Other components including particles of silicon dioxide, magnetite, rutile, ilmenite, iron-chromium spinels and calcite which are strictly subordinate. In addition, traces of the sludge contain traces of finely dispersed highly porous carbonate mass surrounding the relics of kaolin particles.

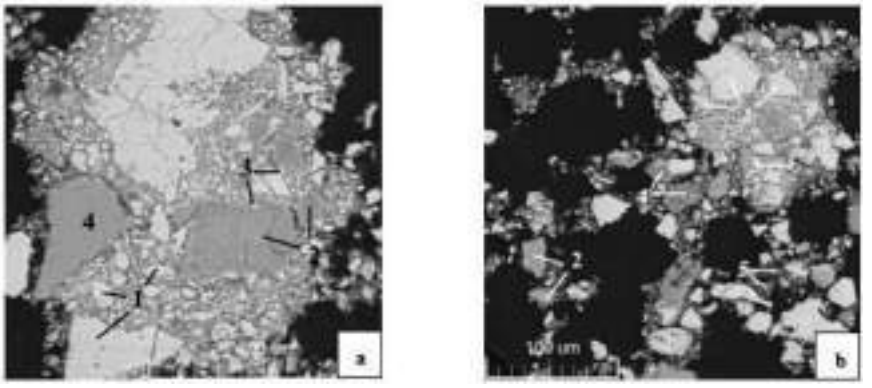

Figure 5. The main structural components of (a) the sinter and (b) the sludge samples produced at 800°C where, 1- calcium carbonate, 2- relics of kaolin, 3- particles of magnetite/rutile/other heavy impurities components of the charge, 4- silicon dioxide and 5- fine carbonate mass.

It can be concluded, that is the sintering temperature of 800°C is not sufficient to the decomposition and dissociation of the calcium carbonate. There for, there is no solid state reaction between metakaolinite produced from the dehydroxylation of kaolin ore and the calcium carbonate. It was also noted that the formation of calcium aluminates in the sintered material is not marked and this means that this temperature is not sufficient to the formation of this phase from which alumina can be extracted easily. This explains the lower recovery of alumina from the sinter produced at this temperature as shown in Figure 4 and this means that is the extraction of alumina is carried out from the metakaolinite particles. It was also detected that is the aluminum in the samples of both sinter and sludge produced at 800°C is concentrated in kaolin relics.

The main structural components of both the sinter and sludge produced at 1000°C are illustrated in Figure 6. It Indicate that both of them have mainly the same composition of relics of calcium carbonates, relics of kaolin, secondary aluminosilicate rims, and silicon dioxide except the sludge contains fine carbonate mass. It was found that the degree of change of these structures are much higher than that occurred at 800°C. It can be seen that; nearly most of calcium carbonates is characterized by a high degree of decomposition up to complete destruction. On the other hand for kaolin, it is shown that secondary aluminosilicate rims of a wide range of composition are present on the surface.

The main structural components of the sinter produced at 1360°C are illustrated in Figure 7a. The most common components in the sinter are aluminosilicate components of a wide range of composition, calcium silicate and calcium aluminate. These components are presented both in the form of free particles and in association with each other and the other components. The main structural components of the sludge produced at 1360°C are illustrated in Figure 7b. It is clear that the most common components in the sludge are aluminosilicate components of a wide range of composition. It was also noted that the main structural components of the sludge is nearly the same for the sinter in addition to the presence of $CaCO_3$ as a result of the leaching process. Also in the structural components of the sinter and sludge it was noted that, in addition to aluminosilicates, calcium silicates and calcium aluminates of variable composition with noticeable admixtures of other elements are subordinate to the samples. It was noted that the content of aluminates in the sample of sludge is significantly lower than its content in the sinter sample that explains the higher recovery of alumina at this sintering temperature (ElDeeb et al., 2019).

3.4 *The effect of sintering temperature on the efficiency of the self-disintegration process*

The sintering temperature has also a significant effect on the efficiency of the self-disintegration process and the completeness of the phase transformations, hence the

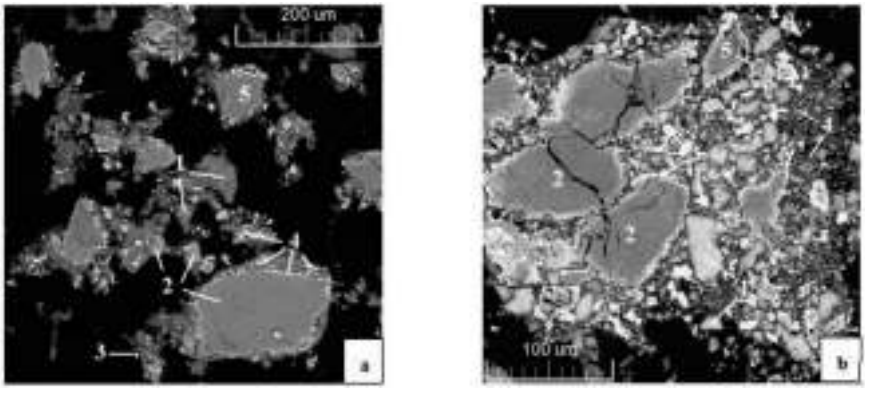

Figure 6. The main structural components of the (a) sinter produced at 1000°C where, 1- relics of calcium carbonate, 2- relics of kaolin, 3- particles of magnetite/rutile/other heavy impurities of the charge, 4- secondary aluminosilicate rims and 5- silicon dioxide. (b) the sludge sample where, 1- relics of carbonates, 2- relics of kaolin, 3- secondary aluminosilicate rims, 4- fine carbonate mass and 5- silicon dioxide.

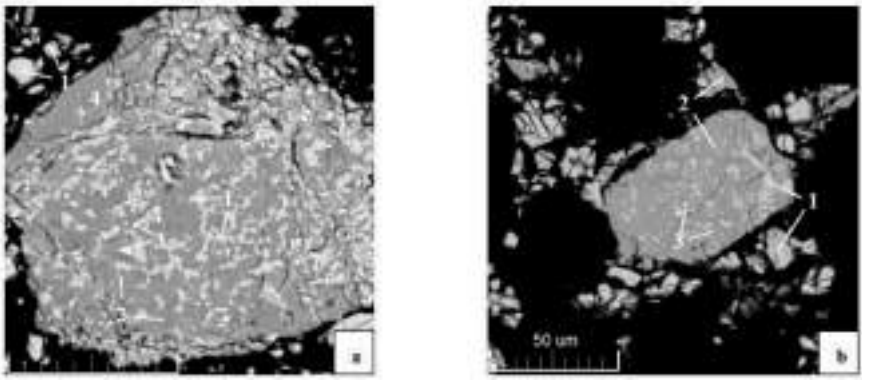

Figure 7. The main structural components of the sinter sample produced at 1360°C where, 1- calcium silicates, 2- aluminosilicates, 3- particles of magnetite/rutile/other heavy impurity components of the charge, 4- calcium aluminates and 5- carbonate components. (b) the sludge sample where, 1- calcium silicates, 2- aluminosilicates of a wide range of composition, 3- particles of magnetite/rutile/other heavy impurity components of the charge, 4- carbonate components and 5- calcium aluminates.

extraction of alumina. The lower sintering temperatures (800-1200°C) are not sufficient for the formation of calcium silicates (C_2S). C_2S undergoes a crystallographic transformation on cooling with an increase in the molar volume due to the transformation of $2CaO{\cdot}SiO_2$ from β to γ form as shown in following equation. In contrast, high sintering temperatures (1300-1400°C) are sufficient for the formation of C_2S in sufficient amounts that leads to the transformation of the sintered briquettes into fine powder, which increases the solubility of the alumina containg compounds without any need for further grinding (Stange et al., 2017).

$$\beta - Ca_2SiO_4 \xrightarrow{675^{\circ}C} \gamma - Ca_2SiO_4$$

The results of the particle size analysis of the produced sinter and sludge using the domestic microsizer 201C analyzer is shown in Figure 8. It is clear that there is an enlargement in the particle size of the sludge obtained after the leaching process compared to the size of the sinter. The agglomeration and the increase in particle size of the produced sludge can be attributed to the formation of $CaCO_3$ at the surface of the produced sludge (Zhang, et al., 2015).

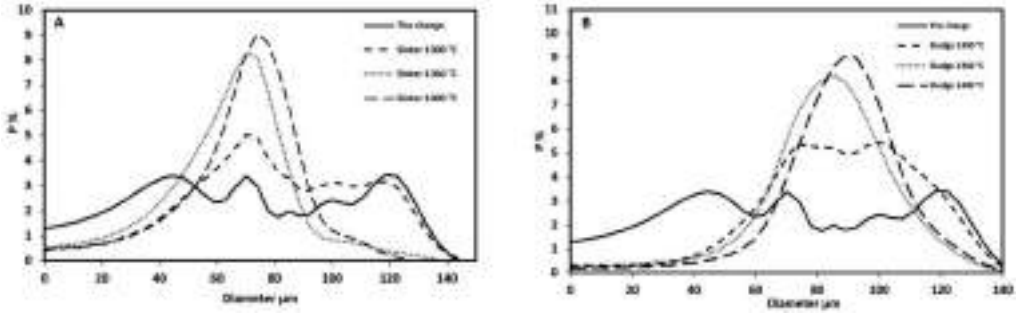

Figure 8. The effect of the sintering temperature on the particle size of the (A) sinter and (B) sludge obtained at different sintering temperature.

4 CONCLUSION

The obtained results indicate that is the sintering temperature has a significant effect on the solid state, phase transformation mechanism and hence the efficiency of alumina extraction from kaolin ore processed using lime-sinter process. The lower sintering temperatures are not enough for the melting of the original compounds of the charge and the solid state reaction between the metakaolinite and calcium carbonate doesn't occur. The extraction of alumina is carried out only from metakaolinite that explains the lower recovery of alumina at this temperature of about 10.51% at 800°C. The higher sintering temperatures are enough for the complete dehydroxylation of kaolinite and decomposition of calcium carbonate and at the same time the melting of the original constituents with the formation of calcium aluminates and calcium silicates in different forms. These temperatures enhancing the extraction of alumina to be 60.74% at 1000°C and 80.49% % at 1360°C. The more increase in the sintering temperature more than 1360°C leads to the formation of mullite phase ($3Al_2O_3.2SiO_2$) with higher percentage from which it is difficult to extract alumina which explains the decreasing of alumina extraction at1400°C to about 59.70%. Thus, it is obvious that is the sintering temperature of 1360°C is the most suitable temperature for the higher extraction of alumina from kaolin. The agglomeration of secondary $CaCO_3$ particles on the surface of the insoluble particles is the dominant mechanism of increasing the particle size of the produced sludge compared to the original particle size of the obtained sinter.

ACKNOWLEDGMENT

The work was carried out with the financial support of the Russian Science Foundation under the agreement No. 18-19-00577 of April 26 2018 of grant for fundamental scientific research and exploratory scientific research.

REFERENCES

Al-Ajeel, A.A. & Abdullah, S.Z. & Muslim, W.A. & Abdulkhader, M.Q. & Al-Halbosy, M.K. & Al-Jumely, F.A. 2014. Extraction of Alumina from Iraqi colored kaolin by lime-sinter process. Iraqi Bull. Geol. Min. 10 (3): 109–117.

Andrews, A. & Nsiah-Baafi, E. & Gawu, S.K.Y. & Olubambi, P.A. 2014. Synthesis of high alumina refractories from lithomargic clay. Ceramics International 40 (4): 6071–6075.

Brichkin, V.N. & Kurtenkov, R.V. & ElDeeb, A.B. & Bormotov, I.S. 2019. State and development options for the raw material base of aluminum in non-bauxite regions. Obogashchenie Rud 4: 31–37.

Cohen, J. & Mercier, H. 2016. Recovery of alumina from Non-Bauxite aluminum-bearing raw materials. In: Donaldson D., Raahauge B.E. (eds.) Essential Readings in Light Metals. Springer, Cham. 1057–1064.

Dubovikov, O.A. & Brichkin, V.N. 2016. Directions and prospects of using low grade process fuel to produce alumina. Journal of Mining Institute 220: 587–594.

ElDeeb, A.B.S. & Brichkin, V.N. 2018. Egyptian aluminum containing ores and prospects for their use in the production of Aluminum. Int. J. Sci. Eng. Res. 9 (5): 721–731.

ElDeeb, A.B. & Brichkin, V.N. & Kurtenkov, R.V. & Bormotov, I.S. 2019. Extraction of alumina from kaolin by a combination of Pyro- and hydrometallurgical Processes. Applied Clay Science 172: 146–154.

Imanaka Y., 2015. Materials and processes of microelectronic packing including low temperature cofired ceramics technology (past, present and future). J. Ceram. Sci. Tech. 6 (4): 291–300.

Garg, P. & Jamwal, A. & Kumar, D. & Sadasivuni, K.K. & Hussain, C.M. & Gupta, P. 2019. Advance research progresses in aluminium matrix composites: manufacturing & applications. Journal of Materials Research and Technology 8 (5): 4924–4939.

Kvande, H. 2014. The Aluminum Smelting Process. Journal of Occupational and Environmental Medicine 56: S2–S4.

Lee, J.S. & Kim, H.S. & Park, N.-K. & Lee, T.J. & Kang, M. 2013. Low temperature synthesis of α-alumina from aluminum hydroxide hydrothermally synthesized using [Al(C_2O_4)x(OH)y] complexes. Chemical Engineering Journal 230: 351–360.

Lee, S.O. & Jung, K.H. & Oh, C.J. & Lee, Y.H. & Tran, T. & Kim, M.J. 2009. Precipitation of fine aluminum hydroxide from Bayer liquors. Hydrometallurgy 98 (1-2): 156–161.

Lei, H. & Wu, X. & Chen, R. 2012. Preparation of porous alumina abrasives and their chemical mechanical polishing behavior. Thin Solid Films 520 (7): 2868–2872.
Lima, P.E.A. & Angélica, R.S. & Neves, R.F. 2014. Dissolution kinetics of metakaolin in sulfuric acid: comparison between heterogeneous and homogeneous reaction methods. Applied Clay Science 88-89 (3): 159–162.
Olaremu, A.G. 2015. Sequential leaching for the production of alumina from a Nigerian clay. Int. J. Eng. Technol. Manag. Appl. Sci. 3 (7): 103–109.
Osman, A.I. & Abu-Dahrieh, J.K. & Rooney, D.W. & Thompson, J. & Halawy, S.A. & Mohamed, M. A. 2017. Surface hydrophobicity and acidity effect on alumina catalyst in catalytic methanol dehydration reaction. Journal of Chemical Technology & Biotechnology 92 (12): 2952–2962.
Phung, T.K. & Lagazzo, A. & Rivero Crespo, M.Á. & Sánchez Escribano, V. & Busca, G. 2014. A study of commercial transition aluminas and of their catalytic activity in the dehydration of ethanol. Journal of Catalysis 311: 102–113.
Protosenya A.G. & Trushko O.V., 2007. Problems of the development of the raw material base of the aluminum industry in Russia and the organization of production in a market economy. Journal of Mining Institute 172: 132–137.
Qiao, X.C. & Si, P. & Yu, J.G. 2008. A Systematic Investigation into the Extraction of Aluminum from Coal Spoil through Kaolinite. Environ. Sci. Technol., 42 (22): 8541–8546.
Salahudeen, N. & Ahmed, A.S. & Al-Muhtaseb, A.H. & Dauda, M. & Waziri, S. M. & Jibril, B. Y. 2015. Synthesis of gamma alumina from Kankara kaolin using a novel technique. Applied Clay Science 105-106: 170–177.
Seyed, A.H. & Aligholi N. & Dariush S. 2011. Production of γ-Al_2O_3 from Kaolin. Open Journal of Physical Chemistry 1: 23–27.
Sizyakov, V.M. & Brichkin, V.N. & ElDeeb, A. B. & Kurtenkov, R.V. 2019. Egyptian aluminum-containing raw materials and the prospects for its integrated processing to produce alumina and by-products. XI International Congress & Exhibition Non-Ferrous Metals & Minerals, Proceedings of 37th International ICSOBA Conference, Krasnoyarsk, Russia, 16-20 September, 2019, http://nfmsib.ru/wp-content/uploads/2019/08/spisok-dokladov-Alyuminij-Sibiri_6.08.pdf.
Sizyakov, V.M. & Brichkin, V.N. 2018. About the role of Hydrafed calcium carboaluminates in improving the technology of complex processing of nephelines. Journal of Mining Institute 231: 292–298.
Sizyakov, V.M. 2016. Chemical and technological mechanisms of a alkaline aluminum silicates sintering and a hydrochemical sinter processing. Journal of Mining Institute 217: 102–112.
Sizyiakov, V.M. & Dubovikov, O.A. & Nikolaeva, N.V. & Kalashnikova, M.I. 2013. The role of mineralized additivies in the alumina phase transformation process. Journal of Mining Institute 202: 48–55.
Sizyiakov V.M. 2006. Influence of nepheline and limestone dispersion on the quality of aluminate sinter. Journal of Mining Institute 169: 35–40.
Sizyakov, V.M. 2005. Current status and problems of the Russian aluminum industry. Journal of Mining Institute 165: 163–169.
Stange, K. & Lenting, C. & Geisler, T. 2017. Insights into the evolution of carbonate-bearing kaolin during sintering revealed by in situ hyperspectral Raman imaging. Journal of the American Ceramic Society:1–14.
Suss, A.G. & Damaskin, A.A. & Senyuta, A.S. & Panov, A.V. & Smirnov, A.A. 2014. The influence of the mineral composition of low-grade aluminum ores on aluminium extraction by acid leaching. In: Grandfield J. (eds) Light Metals 2014, Springer, Cham,:105–109.
Tian, Y. & Pan, X. & Yu, H. & Han, Y. & Tu, G. & Bi, S. 2016. An improved lime sinter process to produce Al_2O_3 from low-grade Al-containing resources. In: Williams E. (eds) Light Metals. Springer, Cham: 5–9.
Ueki, Y. & Kunugi, T. & Morley, N.B. & Abdou, M.A. 2010. Electrical insulation test of alumina coating fabricated by sol–gel method in molten PbLi pool. Fusion Engineering and Design 85 (10-12): 1824–1828.
Wan, Ye & Wang, Huan & Zhang, Yundian & Wang, Xiumei & Li, Yanbo. 2018. Study on Anodic Oxidation and Sealing of Aluminum Alloy. Int. J. Electrochem. Sci. 13: 2175–2185.
Xiao, J. & Li, F. &, Zhong, Q. & SS Bao, H. & Wang, B. & Huang, J. & Zhang, Y. 2015. Separation of aluminum and silica from coal gangue by elevated temperature acid leaching for the preparation of alumina and SiC. Hydrometallurgy 155: 118–124.
Yan, K. & Guo, Y. &, Fang, Li & Cui, Li & Cheng, F. & Li, T. 2017. Decomposition and phase transformation mechanism of kaolinite calcined with sodium carbonate. Applied Clay Science 147: 90–96.
Zhang, S. & Ou, X. & Qiang, Y. & Niu, J. & Komarneni, S. 2015. Thermal decomposition behavior and de-intercalation mechanism of acetamide intercalated into kaolinite by thermoanalytical techniques. Applied Clay Science 114 (10): 309–314.

Advances in Raw Material Industries for Sustainable Development Goals – Litvinenko (Ed)
© 2021 Taylor & Francis Group, London, ISBN 978-0-367-75881-3

New approaches in mineral raw materials comminution tests modelling

L.S. Chitalov
Postgraduate student, St. Petersburg mining University, St. Petersburg, Russia

V.V. Lvov
PhD, Associate professor, St. Petersburg mining University, St. Petersburg, Russia

ABSTRACT: The paper discusses a model of ore particles crushing with a JK Drop Weight Tester, created using the method of discrete elements in the Rocky DEM software. The mathematical relationship between output parameters of the JK Drop Weight Test (JK DWT) and parameters of the breakage model in Rocky DEM is shown. A JK DWT was performed on a technological sample of copper-nickel ore. The JK DWT results were used in Rocky DEM to calibrate its breakage model by factorial experiment using two parameters that are not related to the results of the JK DWT. The achieved accuracy of the resulting model is ± 3.1% of the t_{10} value. The resulting model can be used to obtain the particle size distribution of crushing products for various comminution machines, as well as for determination the parameters for calibrating mathematical models of crushers, autogenous and semi-autogenous mills in the JKSimMet.

1 INTRODUCTION

In the practice of mineral processing, comminution processes are the most expensive due to their high energy consumption. Today, the main way of reducing energy costs for crushing and grinding is optimizing these processes through mathematical modeling. At the same time, no modeling can be carried out without the strength characteristics of mineral raw materials (Gospodarikov & Zatsepin, 2019, Zuev et al., 2019). Obtaining such characteristics is closely related to laboratory tests, which describe the relationship between the change in the size of the material and the energy expended on this change. The JK Drop Weight Test is one of the most used worldwide comminution test. Its results may be used as inputs parameters for calibration different kind of breakage models. One of them, constructed with the discrete element method, was calibrated in this study (Taranov et al., 2013).

1.1 *JK drop weight test*

JK Drop Weight Test (JK DWT) (Nikolaeva et al., 2017, Andreev et al., 2012) of JKTech (Australia) is developed by the Julius Kruttschnitt Mineral Research Centre. Power measurements in the range of size (from 13 to 63 mm) at different energy levels (from 0.1 to 2.5 kWh/t) were obtained in the test for copper-nickel ore. The equipment for determining the breakage function is called the JK Drop Weight Tester (JK DW). Test results were reduced to three parameters - A, b and t_a for subsequent use in the JKSimMet software.

1.2 *JKSimMet*

When modeling in JKSimMet, the ore parameters are combined with the comminution equipment details and operating conditions, which allow to predict the performance of autogenous

grinding and semi-autogenous grinding mills (AG/SAG), crushers and other comminution equipment, as well as to obtain information on the particle size distribution. Using JKSimMet in conjunctions with the JKSimFloat software it is possible to optimize existing or design new flowsheets for comminution circuits and flowsheets that include flotation operations (Alexandrova et al., 2019).

Despite the fact that JKSimMet is a leader in its field, its computational system is fixed; the simulation itself is static and does not take into account all the factors that affect the process. So, as the parts of the ore dressing machine wear out, there are modifications in the technological processes occurring. Such changes are not taken into account when modeling in JKSimMet.

1.3 *Discrete Element Method (DEM)*

The discrete element method as applied in mining is a method of modeling physical processes in which step-by-step calculation of particles kinetics of their motions and collisions with other particles and machine construction is carried out for individual particles. DEM simulations are widely used for AG/SAG processes, but as a rule only with a qualitative assessment of the dynamics of mill load (Cleary et al., 2003, Weerasrkara et al., 2013). Recently, the Rocky DEM software (Rocky) has the ability to model particle breakage processes (Beloglazov, 2018), in which the parameters obtained by JK DWT are basic. However, due to a number of limitations of DEM modeling, direct input of JK DWT results into the Rocky interface is not possible. At the same time, Rocky's mathematical model is easy to control, and the modeling process is dynamic.

2 MATERIALS AND METHODS

2.1 *The subject, tasks and the aim of the study*

The aim of this work is to combine the mathematical aspects of the breakage model of mineral raw materials in Rocky DEM software in line with the results of the drop weight test for the material (model verification). The object of the study was a copper-nickel ore sample.

The tasks include carrying out laboratory tests according to the JK DWT method on a technological sample of copper-nickel ore; comparing the theoretical foundations of JK DWT and the mathematical apparatus of breakage model in Rocky; verification of mineral breakage modeling by the JK DWT using the discrete element method in Rocky DEM software by means of a complete model factor experiment.

Subsequently, a calibrated fracture model in Rocky can be used to obtain data that allows the calibration of mathematical models of hand-held apparatuses in JKSimMet, as well as to clarify the effect of abrasive wear of the apparatuses construction on the course of the technological process.

2.2 *Methods*

The output parameters of the JK DWT are A and b characterizing the strength properties of the tested ore. These constants are found after obtaining all the results of sieve analyses of the fracture products and bringing them to the exponential dependence of the following form (see Figure 1):

$$t_{10} = A \cdot (1 - \exp^{-b \cdot E_{cs}}) \tag{1}$$

where t_{10} is the percentage finer than 1/10th of the original particle size %; A - constant (asymptotic, Figure 1); b - constant (controls the shape of the curve); E_{cs} - specific energy, kWh/t, in JK DWT E_{cs} is regulated by the mass of the drop weight and the drop height (equation 2).

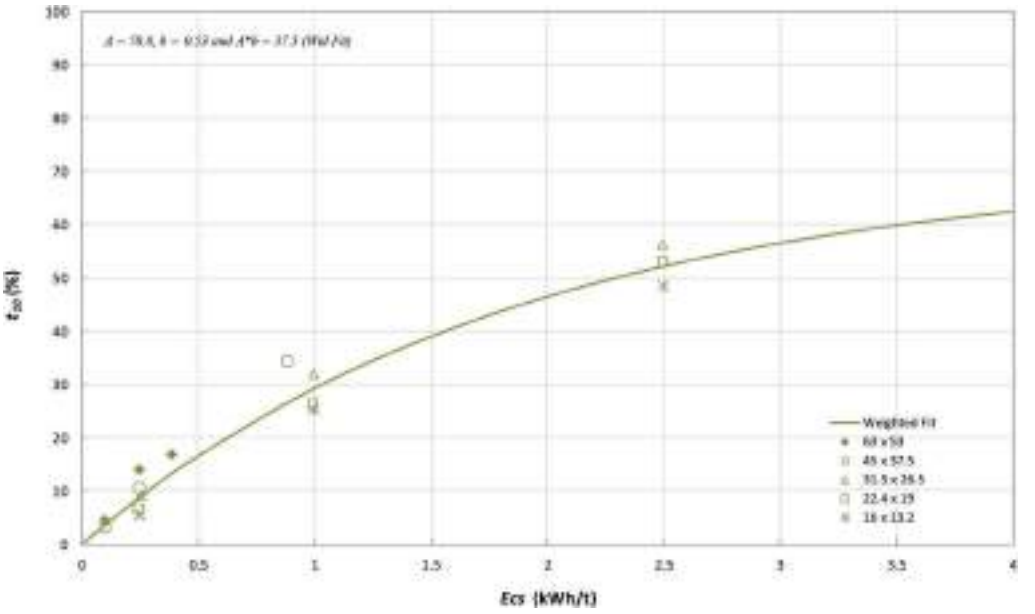

Figure 1. The dependence of the parameter t_{10} on the specific energy Ecs obtained from the JK DWT results for the sample of copper-nickel ore.

$$E_{cs} = \frac{mgh}{3,6m_y} \tag{2}$$

where m is the mass of the weight, kg; m_u - particle mass, g; g is the force due to gravity, m/s^2; h - "clean" drop height (difference between final h_2 and initial h_1 position of the steel weight, h_2 varies as it depends on the residue after breakage.), m.

In Rocky, the model multi-step events of destruction is transformed considering the probability of an act of particle breaking:

$$P(e_{cum}) = 1 - \exp^{-SecumL/Lref}, \tag{3}$$

where $P(e_{cum})$ – probability of breakage at the current value of the total specific energy applied to the particle (e_{cum}), S – constant for the material, called the coefficient of the selection function or the selective coefficient, kg/J; L – particle size, m; L_{ref}–reference particle size, m.

In this case, e_{cum} is the sum of the energies applied to the particle in the current and previous calculation steps t:

$$e^t_{cum} = e^{t-\Delta t}_{cum} + (e^t_c - e^{t-\Delta t}_c) \tag{4}$$

where $e^{t-\Delta t}_{cum}$ and $e^{t-\Delta t}_c$ – total specific contact energy and instantaneous specific contact energy at the previous time step t, respectively.

In addition, in Rocky, for the act of breakage to occur, the specific energy applied to the particle must be greater than the minimum specific energy of destruction, e_{min}, which is determined by the expression:

$$e_{\min} = e_{\min \cdot ref} \frac{L_{ref}}{L} \tag{5}$$

where $e_{min.ref}$ – reference minimum specific energy for the reference particle size of this material. This parameter, among others, is introduced into the fracture model when it is configured in the Rocky interface.

When a particle breaks, fragments are generated in accordance with the Voronoi breakage algorithm (Aurenhammer & Klein, 2000) in accordance with the minimum size of the generated particles, which is set by the user. The value of the parameter t_{10}, which will eventually be generated by the model, is calculated by the expression:

$$t_{10} = A[1 - exp(-Se_{cum}L/L_{ref})] \tag{6}$$

The expression ($e_{cum}L/L_{ref}$) in equation 5 corresponds to the E_{cs} from equation 1 taking into account the size of a particular destructible particle. Thus, to obtain a similar final fracture result in the Rocky JK DW model (see Figure 2, a), the parameters of the minimum specific energy e_{min} from equation 4 and the selective fracture function S from equations 2 and 5 were calibrated.

$$b = \frac{SLe_{cum}}{L_{ref}E_{cs}} = \frac{Se_{cum}e_{\min .ref}}{E_{cs}e_{\min}} \tag{7}$$

To solve this problem, a complete factorial model experiment was conducted on the values of the coefficients S and e_{min} comparing the parameter t_{10} obtained on their basis with the results of JK DWT carried out on a sample of the studied copper-nickel ore. To carry out a factor experiment, ANSYS Workbench software was performed, which partially automates the input parameters to the Rocky JK DW model, among which were:

- The mass of the drop weight (8 values for 15 experiments),
- Drop height (15 values for 15 experiments),
- The particle size (5 values for 15 experiments), it was also used as L_{ref},
- Particle mass (15 values for 15 experiments),

Among the varied parameters of the fracture model for each of the 15 experiments were:

- The reference minimum value of specific energy e_{min} from equation 4 (7 values),
- Selective coefficient S from equations 2 and 5 (7 values).

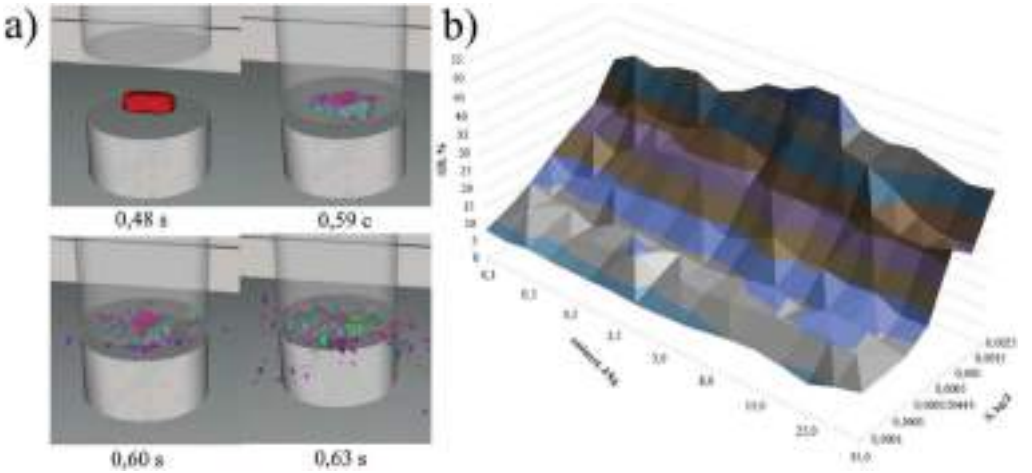

Figure 2. JK DWT modeling: a) a tester in the form of a 3D model; b) a surface diagram for the values of the obtained parameter t_{10} when varying the studied factors.

The constant A form equation 5 was introduced directly into the Rocky model from the results of a JK DWT. The size of the smallest generated particles in each experiment was introduced as 1/50 of the arithmetic mean particle size of the destructible particle size class.

3 RESULTS AND DISCUSSION

A series of experiments was simulated with 49 models for each of 15 sets of JK DWT (735 models in total). The output was reduced to surface diagrams of parameter t_{10} for each of the 15 sets (one of such diagrams is shown in Figure 2, b).

It was established that the influence of the input reference minimum specific energy emin. ref on the value of the output parameter t_{10} is insignificant in comparison with the influence of the selective coefficient S (see Figure 2, b). This is explained by the specificity of the destruction of the material using the JK DW installation, aimed at creating a single act of destruction by each of the particles included in the set.

The results obtained for equation 7 are presented in Table 1.

Figure 3 shows the initial dependence $t_{10}= f(A, b)$ and the same dependence obtained from the DEM simulation of the JK DW installation in Rocky.

Table 2 presents the initial strength parameters A and b obtained from Rocky models.

Table 1. The absolute error in determining the value t_{10}, %.

	Sizes, mm				
Specific energy, kWh/t	-63 +53	-45 +37,5	-31,5 +26,5	-22,4 +19	-16 +13,2
0,10	-0,31	0,13	-	-	-
0,25	1,17	1,01	-1,20	0,01	0,15
0,40	0,13	-	-	-	-
1,00	-	-2,70	2,12	-0,90	-1,43
2,50	-	-	3,07	-3,06	1,81

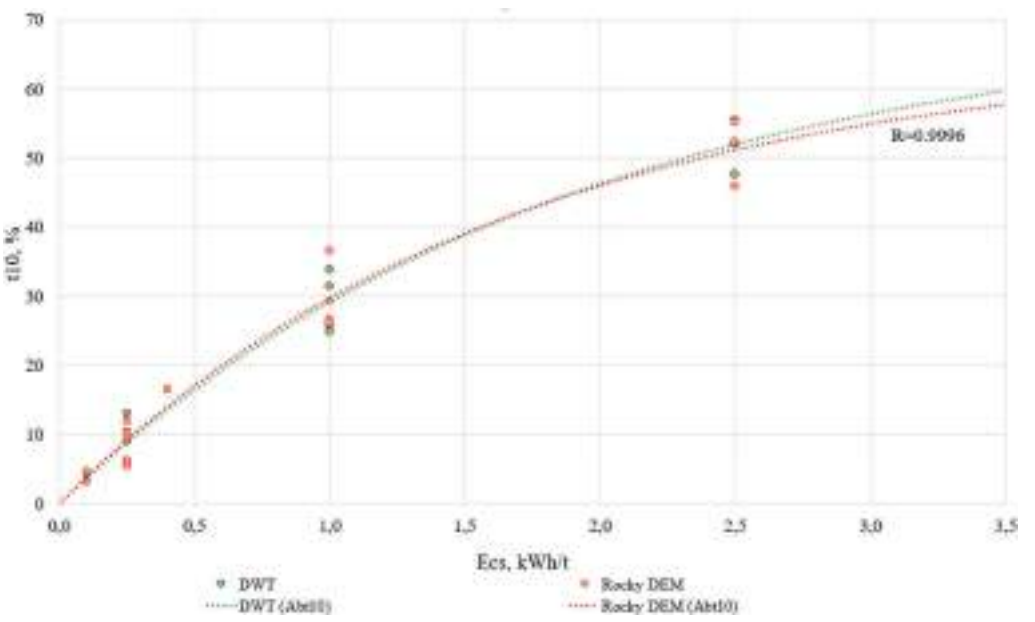

Figure 3. The dependence obtained from the results of DEM modelling.

Table 2. Strength parameters obtained by the DEM model.

Parameter	JK DWT	Rocky DEM
A	70,8	65,7
b	0,53	0,60
Ab	37,5	39,6

4 CONCLUSIONS

According to the results of the work, the coefficients of the mathematical model in Rocky, making it possible to predict the parameter t10 obtained in the JK DWT experiments for various values of the specific breakage energy for all studied particle size fractions with an accuracy of ± 3.1% at a confidence interval of 95%. The repeatability of the model has not been estimated with many tests. Despite this, the resulting model allows to calibrate mathematical models in JKSimMet software for such ore dressing equipment as crushers and AG/SAG mills according to the power parameters developed under load and particle size distribution of the feed and crushing product taking into account the lining wear rate.

The calibrated breakage Rocky DEM model may be used for analysis of particle size distribution changes during dry crushing and grinding processes of the studied nick-el-copper ore sample and during JKSimMet equipment settings:

- When making structural changes to ore preparation machines (using non-standard discharge gratings in AG mills, using non-standard lining in crushers, etc.);
- With the abrasive wear of the constructions of comminution equipment;
- To analyze the equipment which is not included in the list of supported in JKSimMet software.
- The research was carried out under the grant received from Russian Foundation of Fundamental Research № 20-55-12002

REFERENCES

Aleksandrova T. N., Nikolaeva N.V., Lvov V.V., Romashev A.O. 2019. Ore processing efficiency improvements for precious metals based on process simulations. Obogashchenie rud, No. 2: 8–13. DOI: 10.17580/or.2019.02.02.

Andreev Ye.Ye., Zakhvatkin V.V., Lvov V.V., Nikolaeva N.V. 2019. Application of falling weight test for estimation of ore strength properties. Obogashchenie rud, No. 3: 19–22.

Aurenhammer F., Klein R. 2000. Voronoi Diagrams. Handbook of Computational Geometryю In J. R. Sack and J. Urrutia (ed.) Amsterdam, Holland: North-Holland: 201–290.

Beloglazov I.I., Stepanyan A.S., Feoktistov A.Yu., Yusupov G.A. 2018. Disintegration process modeling for a jaw crusher with complex jaws swing. Obogashchenie rud, No. 2: 3–8. DOI: 10.17580/or.2018.02.01.

Cleary P.W., Morrisson R., Morrell S. 2003. Comparison of DEM and experiment for a scale model SAG mill. Mineral Processing, No. 68: 129–165.

Gospodarikov A.P. & Zatsepin, M.A. 2019. Mathematical modeling of boundary problems in geomechanics. Gornyi Zhurnal, Issue 12: 16–20.

Nikolaeva N.V., Aleksandrova, T.N., Taranov, V.A. 2017. Determination of the degree of impact destruction of gold-bearing ore particles in the layer. Information (Japan), 20(9): 6605–6613.

Taranov, V.A., Baranov V.F., Aleksandrova T.N. 2013. Review of software for modeling and calculation of ore preparation flowsheets. Obogashchenie rud, No. 5: 3–7.

Weerasekara N.S., Powell M.S., Cleary P.W., Tavares L.M., Evertsson M., Morrison R.D., Quist J., Carvalho R.M. 2013. The contribution of DEM to the science of comminution. Powder Technology no. 248: 3–24.

Zuev B.Y., Zubov V.P., Smychnik A.D. 2019. Determination of static and dynamic stresses in physical models of layered and block rock masses. Gornyi Zhurnal, Issue 7: 61–66.

Advances in Raw Material Industries for Sustainable Development Goals – Litvinenko (Ed)
© 2021 Taylor & Francis Group, London, ISBN 978-0-367-75881-3

Research on the patterns of structure formation processes of a clinker-free alkaline stone

S-A.Yu. Murtazaev, M.Sh. Salamanova & M.Sh. Mintsaev
FSFEI HE "Millionschikov Grozny State Oil Technical University", Kh. Ibragimov Complex Institute of the Russian Academy of Sciences, Grozny, Russia

D.K-S. Bataev
Kh. Ibragimov Complex Institute of the Russian Academy of Sciences, Grozny, Russia

ABSTRACT: Resource- and energy-consuming Portland cement is currently considered the most popular material in construction, but its production is classified as harmful due to the large amount of emissions into the environment. Therefore, the development of a clinker-free technology for the production of binders based on mineral fine-dispersed powders of aluminosilicate nature, activated by an alkaline grouting fluid, is an urgent and promising direction.

The research presents the results of a study on the laws of processes occurring during the structure formation of clinker-free binder systems of alkaline activation on alkaline cements using blast furnace granulated slags in a finely dispersed state. Formulations are given and the properties of clinker-free binders of alkaline activation based on mineral finely dispersed powders from rocks of sedimentary and magmatic origin are investigated. Electron probe analysis and X-ray phase analysis revealed the presence of hydrated amorphous compounds close in composition to zeolites in cement stone. An analysis of the results allowed us to determine the optimal composition of clinker-free binder of alkaline activation "silicified marl + volcanic tuff (70: 30%) + Na_2SiO_3 + NaOH" with activity ranging from 42.0 - 54.5 MPa, depending on the conditions under which the hardening of the samples was implemented.

This work was carried out as part of research on the implementation of scientific project No. 05.607.21.0320. "Development of technology for new building composites on clinkerless alkaline binders using substandard natural and secondary raw materials" that received support from the federal target program "Research and Development in Priority Directions for the Development of the Russian Science and Technology Complex for 2014-2020". Unique Agreement Identifier RFMTFI60719X0320.

Keywords: High-strength concrete, super concrete, local raw materials, products of buildings and constructions demolition and dismantling, concrete scrap, brick rubble, recycling, secondary or recycled filler (sand), filled binder, concrete

1 INTRODUCTION

The fundamental factor in the formation of structure-forming elements, both of various dense rocks, and for all traditional mineral binders is the presence of an alkaline environment created by alkaline and alkaline earth metals. Minerals such as zeolites and feldspars in the Na_2O - Al_2O_3 - SiO_2 - H_2O system were formed as a result of metamorphic processes in the earth's crust, under conditions of high temperatures, humidity, pressures, weathering and cementation with alkaline compounds of aluminosilicate rocks. But it must be taken into account that in alkaline cements, the main astringent function is performed by com-pounds of alkali metals with silicates, aluminates, and water, which are much more active than alkaline

earth oxides and create a stronger alkaline environment (Glukhovsky et al., 1981, Glukhovsky et al., 1980).

The mechanism for creating durable compositions from traditional cements is based on the synthesis of calcium salts, which, when hydrated, give an alkaline environment saturated with calcium hydroxide, which will subsequently become a component of crystallization formations. Having located the elements of alkali-containing compounds in basicity: Cs, Kb, K, Na, Li, Ba, Sr, Ca, Mg, we observe a decrease in activity and pH of the medium from left to right, therefore, caustic alkalis of sodium and potassium are strong bases, and will allow to obtain multicomponent cement systems with hydraulic properties (Glukhovsky et al., 1981, Krivenko et al., 1993, Salamanova & Murtazaev et al., 2017, Murtazaev & Salamanova et al., 2018).

2 LITERATURE REVIEW

A study of the issues related to the reactivity of the studied compounds showed that the minerals of alkaline-earth aluminosilicates, silicates, aluminates do not react with water, and for the hydration interaction to occur, it is necessary to increase the basicity of the dispersion phase, which is possible by introducing an alkaline component into the hardener, which will lead to the formation of a system with a clear increase in strength indicators.

In the works of Glukhovsky (Glukhovsky et al., 1981, Glukhovsky et al., 1980) it is proposed to classify the hydration characteristics of alkaline compounds depending on the chemical and mineralogical compositions:

– caustic alkali solutions of ROH type;
– soft acids salts of non-siliceous nature, such as R_2CO_3, R_2SO_3, R_2S, RF, etc.;
– siliceous salt of the R_2O – (0,5 – 4,0) – $Si0_2$ composition;
– aluminate salts of the R_2O – $A1_2O_3$ composition;
– aluminosilicate salts of the R_2O – $A1_2O_3$ – (2 – 6) SiO_2 type;
– salts of strong acids of non-siliceous nature such as RCl, R_2SO_4.

The hydration ability was studied (Davidovitz et al., 2008, Duxson et al., 2007, Nikiforov et al., 2011, Krivenko et al., 2006) on samples of normal consistency, from blast furnace granulated slag of aluminosilicate nature, mixed with the corresponding alkaline solutions, with Na_2O content in a binder (up to 3%). Table 1 shows a comparative analysis of slag-alkali compositions.

The dependence of the strength index of the studied alkaline compositions on the type of alkaline solution showed that the activity of binders is determined by the nature of the grouting fluid, and reaches its highest index in compounds with alkali metals + silicates of high basicity (Rakhimova et al., 2009). Therefore, the strength indicators of alkaline systems depend on the degree of their solubility and dissociation in water.

Aluminosilicate alkaline groutings, as we know, do not dissolve in water, but as a result of interaction with it, they break off a weak concentration of caustic soda. Aluminates and sodium silicates are readily soluble in water and the results of studies (Murtazaev & Salamanova et al., 2019) confirm their hydration hardening inherent in alkaline earth compounds. Consequently, the dispersed alkaline phase, necessary for hydration processes to form cement

Table 1. The results of determining the activity of blast surface slag compositions (slag compositions in short) (Glukhovsky et al., 1980).

Compressive strength, MPa										
Water	NaOH	Na_2CO_3	$NaNO_3$	NaF	Na_2S	Na_2SiO_3	Na_2O $2SiO_2$	Na_2O $4SiO_2$	Na_2O Al_2O_3 $2SiO_2$	Na_2O Al_2O_3
7,5	80	63	55	85	60	130	160	23	10	67

stone, will be an indispensable condition, and the previously known (Glukhovsky et al., 1980, Duxson et al., 2007, Nikiforov et al., 2011, Krivenko et al., 2006, Bataev & Salamanova et al., 2019) scientific, theoretical and experimental approaches to creating hydraulic binders based on calcium oxide will help to model the algorithm obtaining clinker-free bindings with mineral powders of alkaline mixing.

3 RESEARCH METHODS AND MATERIALS

The regularities and laws of the processes occurring during the formation of the structure of clinker-free binder systems of alkaline activation were studied on slag-alkali cements using blast furnace granulated slags in a finely dispersed state (Rakhimova et al., 2009, Davidovitz et al., 2008, Krivenko et al., 2006, Murtazayev & Alaskhanov et al., 2019). It has been established that compounds of the Si-O-Si and Al-O-Si type in a solution of alkali metals of high concentration are first destroyed, but after a certain time they become denser, trans-forming into a colloidal state.

The mechanism of the structure formation process is quite long and complex. At the first stage of hardening, the dispersed slag particles spontaneously dissolve in the alkali metal solution with the formation of dispersion-coagulative solutions necessary for the formation of the initial structure. Primary neoplasms formed as a result of cationic ex-change of $2Na^{+} \leftrightarrow Ca^{2+}$ are variable in nature.

At the next stage, the formed condensation structure transforms due to mass transfer processes in the colloidal dispersed system, and the transition of hydrosols to the solid phase, which intensifies the crystallization of the structure. A particular alkaline system was studied in a few research papers and it was represented by the following system "$Ca(OH)_2 – SiO_2 – H_2O – NaOH$", and so with the molar ratio $Ca(OH)_2/SiO_2 = 1$, the development of phase formation can be traced:

at $NaOH/SiO_2 < l$, the tobermorite phase is 11.3 Å with silicon-oxygen anions;

at $NaOH/SiO_2 = 1 – 5$, the tobermorite phase is 11.3 Å with the chain structure of silicon-oxygen anions;

at $NaOH/SiO_2 > 5$, sodium cation in the tobermorite phase is $NaCaHSiO_4$ with SiO_4 being isolated.

And at the last stage of structure formation, the primary solid phases of an unstable composition develop, leading to the formation of a strong crystalline intergrowth. The crystallization phases are unstable, and depend on many factors, chemical and mineralogical compositions that make up the system, the nature of the alkaline solution, the dispersion of the components, hardening conditions, etc. Alkaline medium of high basicity promotes the formation of compounds such as tobermorite like low basic calcium hydrosilicates CSH (B), variable hydrogranates, silicic acid gel, alkaline hydroaluminosilicates such as natural zeolites and hydromica, and other alkaline-alkaline earth compounds of variable composition (Rakhimova et al., 2009).

The process of forming the structure of multicomponent systems "mineral powder - alkaline activator" requires a careful analysis, since the characteristics of the binder, its nature, degree of dispersion, alkaline curing agent (alkaline grouting fluid), their dissolution rate, crystallization conditions, interfacial contact zone, and other factors as a whole affect hardening and a cement stone's strength gain. Undoubtedly, the material and quantitative compositions of the components of this complex system will have a direct impact on the process at all stages of structure formation (Rakhimova et al., 2009, Krivenko et al., 2006, Murtazayev & Alaskhanov et al., 2019).

This paper presents its view on the development of clinker-free technology for producing building composites. Considering the fact that in many regions of our vast country there are no reserves of ferrous metallurgy wastes, and transportation of this valuable raw material over long distances is economically disadvantageous, our efforts were aimed at finding materials that mutually substitute (or fill place of) blast furnace granulated slags. And this is no coincidence, the slag of ferrous metallurgy in their chemical composition is identical to the composition of clinker minerals, therefore, the processes of structure formation of cement

stone will be similar for both types of binder. Due to the lack of slag, we made attempts to obtain alkaline mixing binders using finely dispersed mineral powders of various origins.

It becomes possible since the North Caucasus has huge natural potential for the development of the cement industry. In mountainous regions, stocks of cement marls, lime-stones, gaize (silica clay), dolomites, large deposits of mortar and glass sands, coquinoid limestone, sandstone (malmrock), natural sand dunes of the Terskaya lowland are concentrated (Salamanova & Murtazaev et al., 2017).

To develop clinker-free cements of alkaline activation, mineral finely dispersed powders were prepared from rocks of sedimentary and magmatic origin: silicified marl and volcanic tuff from the Kabardino-Balkarian Republic.

4 RESULTS

The energy-dispersive microanalysis of the powders studied using a Quanta 3D 200 i scanning electron microscope showed a significant difference in the chemical composition of the mineral additives:

□ Volcanic tuff, %: MgO = 0,20; Al_2O_3 = 13,57; SiO_2 = 73,67; K_2O = 6,00; CaO = 1,79; Fe_2O_3 = 1,52; TiO_2 = 2,85; other = 0,40.

□ Silicified marl, %: MgO = 1,64; Al_2O_3 = 6,42; SiO_2 = 28,6; K_2O = 1,33; CaO = 16,90; Fe_2O_3 = 1,08; TiO_2 = 0,47; SO_3 = 0,29; other = 43,2.

To study the structure formation processes of cement stone made with clinker-free binders of alkaline activation (CFBAA), electron-probe studies were carried out using a VEGA II LMU scanning electron microscope of the INCA ENERGY 450/XT energy dispersive microanalysis system while X-ray phase analysis was performed on an ARLX'TRA diffractometer. For research, samples were obtained from finely dispersed silicified marl, thermally activated at a temperature of 700 °C, with a specific surface area of 1150 m^2/kg and a finely ground volcanic tuff with a specific surface area of 905 m^2/kg, which were mixed in a predetermined ratio and subsequently tempered with an alkaline solution of salable liquid sodium glass with a silicate module of 2,8 and a density of 1,42 g/cm^3. The prepared samples solidified on the first day under normal conditions at a temperature of 20 ± 2 °C, but after 2 days the samples were being placed into a chamber drier for 2 hours at a temperature of 50 °C every day for the next 28 days.

The studied sample of cement stone is characterized by a thin-crystalline non-uniformly crystalline structure (Figure 1 c) with rounded closed pores with a diameter of up to 0,5 mm (Figure 1 a, b). A commonly dense aggregation of cement mass with particles of sand aggregate is presented.

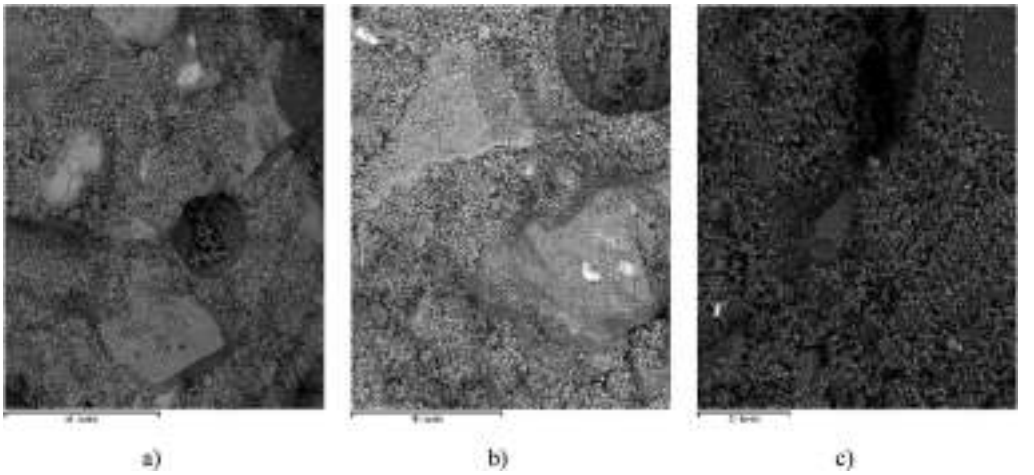

Figure 1. The microstructure of CFBAA cement stone based on volcanic tuff and thermally activated marl.

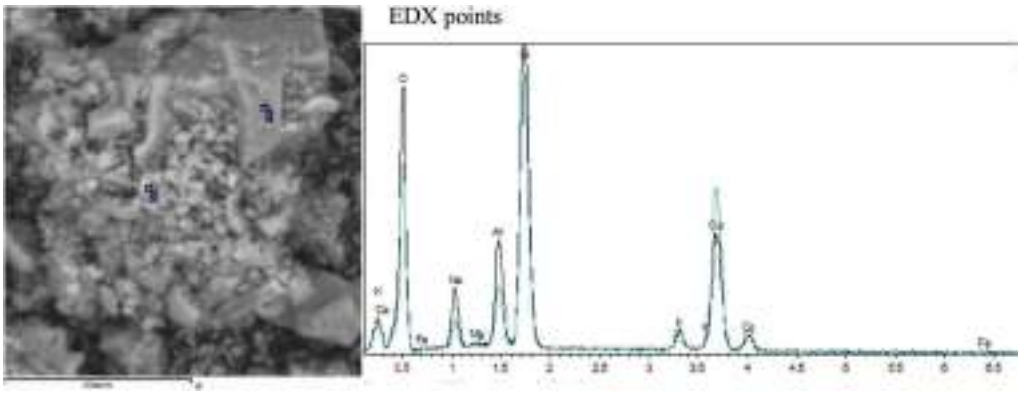

Figure 2. Hydrates of the fragments' mass (1,2).

Table 2. The composition of the hydrates of the presented fragments' mass, in weight. % (points [phases] of analysis are indicated in Figure 2).

Point	Na_2O	MgO	Al_2O_3	SiO_2	K_2O	CaO	FeO	Total
1	8,19	0,22	12,51	46,98	2,05	17,71	0,43	88,09
2	4,13	0,21	6,72	35,82	2,58	24,42	0,52	74,41

Table 3. The composition of the crystals of the presented fractions' mass, in weight. % (points [or phases] of analysis are indicated in Figure 3).

Point	Na_2O	MgO	Al_2O_3	SiO_2	K_2O	CaO	FeO	Total
1	8,66	0,00	18,76	61,65	1,66	7,61	0,40	98,74
2	4,24	0,23	12,12	71,43	5,03	5,57	0,28	98,91
3	0,92	0,21	1,14	5,98	0,23	44,52	0,00	53,00
4	2,36	0,54	1,25	4,35	0,27	43,17	0,00	57,44
5	0,74	0,00	1,03	4,06	0,33	42,55	0,00	48,70

The main structure-forming layers are hydrates of sodium calcium aluminum silicates, often forming dense intergrowths of crystals up to 10-20 μm in size (Figure 2), the composition of which according to the results of a semi-quantitative analysis is shown in Tables 2, 3 (analyzes 1, 2), which are associated with calcite and, apparently, thin layers of $Ca(OH)_2$ (Table 3, analyzes 3-5), as well as thin mica flakes.

Minerals of mica according to x-ray phase and electron probe analyzes correspond to muscovite; the measured flake composition (~ 20 μm in size) is on average close to the formula $(Na_{0.14}K_{0.63})_{0.8}(Fe^{2+}{}_{0.05}Mg_{0.02}Al^{VI}{}_{2.01}Ti_{0.01})_{2.1}(Si_{3.01}Al^{IV}{}_{0.99})_{4.0}O_{10}(OH_{2.00})_{2.0}$ reflecting the enrichment of sodium and aluminum.

According to the results of X-ray phase analysis, the presence of quartz, feldspars close to albite and orthoclase, mica, calcite, zeolites (Figure 4) was established.

5 DISCUSSION

According to X-ray diffraction data, zeolite is identified as close to garronite. $Na_2Ca_5Al_{12}Si_{20}O_{64}•27(H_2O)$ distinctly expressed main reflex at this point (phase) (2Θ - 12,4 (7,10Å)). Electron probe studies reveal the presence of Na-Ca-Si hydrated amorphous compounds with a high

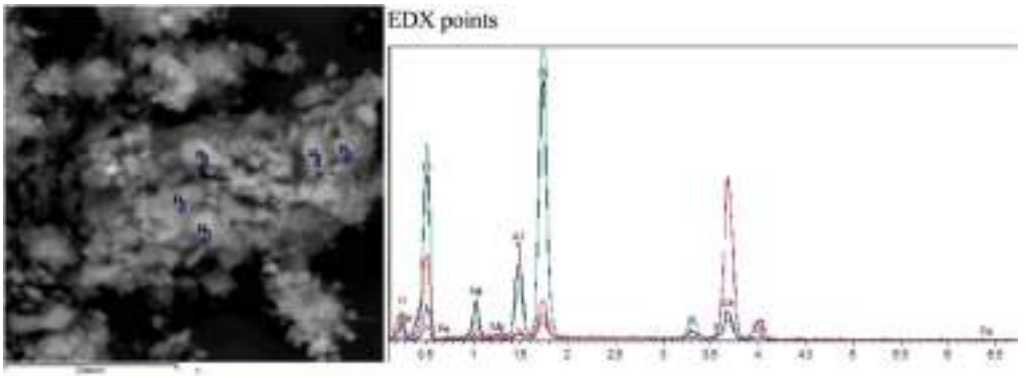

Figure 3. Points of the fragments' mass.

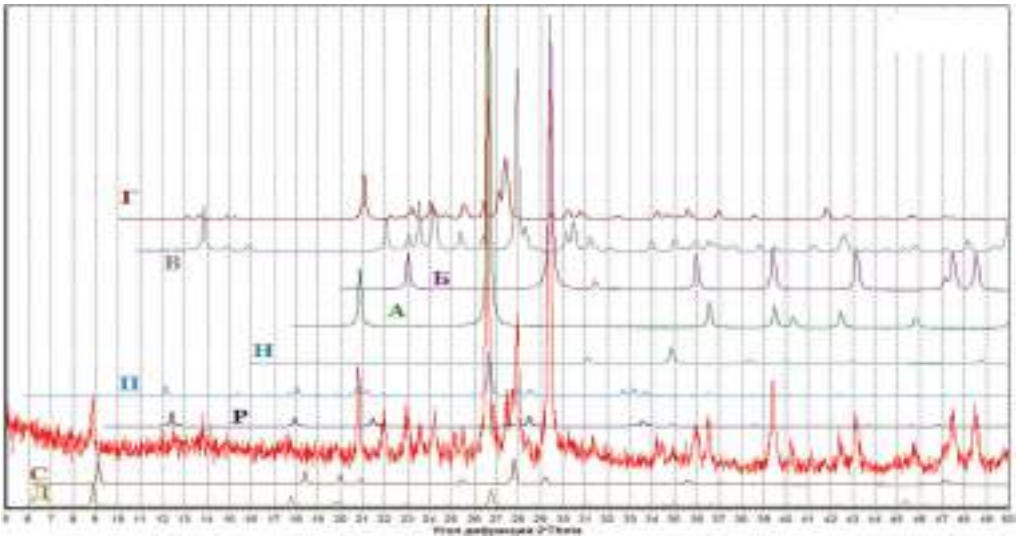

Figure 4. X-ray diffraction pattern of sample 1 in comparison with the data base PDF-2. The comparison points (phases) are as follows (the bracketed letters are Cyrillic Alphabet letters from Figure 4): A (А) — quartz, B (Б) — calcite, C (В) — albite, G (Г) — potassium feldspar, D (Д) — muscovite, N (Н) — analcime, P (П) — jismondite, R (Р) — garronite, S (С) — paragonite.

water content (Figure 5, Table 4) and points (phases) similar to them in composition and also containing aluminum. Additionally, these points (phases) are similar to zeolites in elemental composition (Figure 6; 7, Tables 6 and 7).

The size and surface roughness of the preparations do not allow measurements by quantitative methods, but it can be stated that the composition is close to Ca-phillipsite or garronite (which are characterized by the ratio - SiO_2/Al_2O_3 ~2).

According to the results of X-ray phase analysis in a cement stone of the multicomponent system "mineral powder - alkaline activator" using finely dispersed volcanic tuff powders and thermally activated marl at 700 °C, the presence of quartz, feldspars close to albite and orthoclase, mica, calcite, zeolites has been established. Electron probe studies also reveal the presence of hydrated amorphous Na-Ca-Si compounds of similar compositional phases containing aluminum and close in elemental composition to zeolites.

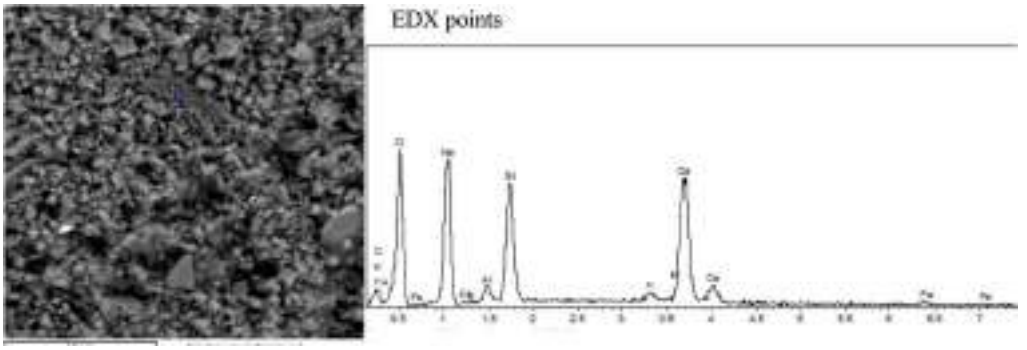

Figure 5. Hydrated Na-Ca-Si compounds in the structure of the material.

Table 4. The composition of the mica crystals, in weight. %.

Point	Na_2O	MgO	Al_2O_3	SiO_2	K_2O	CaO	TiO_2	FeO	Total
1	1,08	0,53	37,45	44,22	8,19	1,00	0,21	1,13	77,58

Table 5. Composition of hydrated Na-Ca-Si compounds (points [or phases] of analysis are indicated in Figure 6), in weight. %.

Point	Na_2O	MgO	Al_2O_3	SiO_2	K_2O	CaO	FeO	Total
1	13,52	0,04	1,43	11,80	0,55	12,31	0,72	40,36

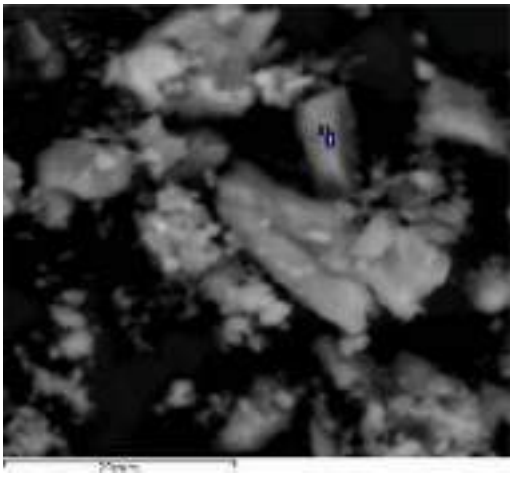

Figure 6. Hydrated Na-Ca-Si compounds in the structure of the material.

To study the kinetics of strength development of the clinker-free binder of alkaline activation, various compositions were prepared from finely dispersed silica marl thermally activated at a temperature of 700 °C with a specific surface of 1150 m^2/kg and finely ground volcanic tuff with a specific surface of 905 m^2/kg, activated with an alkaline solution; the test results are given in Table 7.

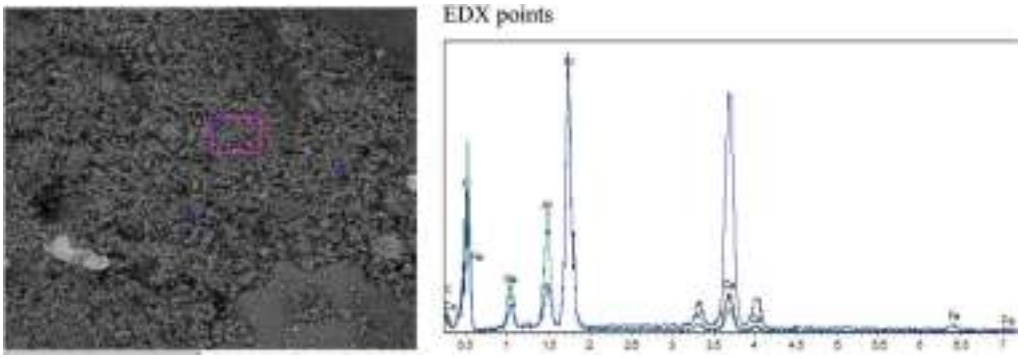

Figure 7. Points of EDX crystals close to zeolites (1, 2) и fragments' main mass (3).

Table 6. The composition of the zeolite point (phase) (points [or phases] of analysis are indicated in Figure 7), in weight. %.

Point	Na_2O	Al_2O_3	SiO_2	K_2O	CaO	FeO	Total
1	5,12	17,07	40,91	0,39	6,47	0,13	71,09

Table 7. Kinetics of strength development of the alkaline activation binder.

	The compressive strength, MPa per day								
	after thermal treatment			in water			normal conditions		
Alkaline activator	28	90	180	28	90	180	28	90	180
silicified marl + volcanic tuff (30:70%)									
Na_2SiO_3 + NaOH	24,5	25,1	26,0	18,3	23,4	24,5	18,3	18,4	19,5
Na_2SiO_3	20,1	20,5	22,3	16,5	17,3	18,5	16,6	17,2	17,6
NaOH	15,0	15,1	15,3	12,4	13,3	13,4	12,2	13,0	13,3
silicified marl + volcanic tuff (50:50%)									
Na_2SiO_3 + NaOH	43,0	47,5	49,7	41,8	43,8	44,7	38,0	41,8	42,7
Na_2SiO_3	34,3	35,8	36,9	30,2	31,4	32,7	31,5	32,3	33,6
NaOH	25,2	27,8	28,6	24,8	26,1	27,6	27,5	27,4	27,9
silicified marl + volcanic tuff (70:30%)									
Na_2SiO_3 + NaOH	46,5	52,4	54,5	45,6	47,6	49,6	42,0	43,7	44,3
Na_2SiO_3	37,2	38,6	40,8	35,4	38,4	39,9	34,1	36,3	37,5
NaOH	30,0	31,6	32,7	30,4	31,2	33,1	28,7	28,8	30,9

6 CONCLUSIONS

The results showed that clinker-free binder of alkaline activation of the "silicified marl + volcanic tuff (70:30%) – Na_2SiO_3 + NaOH" composition can be considered as an optimal one. The activity of cement stone varies from 42.0 to 54.5 MPa depending on hardening conditions affecting the samples. It can be noted that heat treatment favorably affects the kinetics of the strength development of cement stone. Activation of the investigated multi-component systems with sodium hydroxide solution is inferior to sodium metasilicate.

Thus, the obtained research results will significantly expand the scope of application of clinker-free cements of alkaline activation in regions experiencing a shortage of ferrous metallurgy waste, and become an alternative to energy and resource-consuming Portland cement, and, of course, it will be possible, if necessary, to replace it in the construction industry as the studies have confirmed the presence of hydrated amorphous Na-Ca-Si compounds, similar in composition of studied fragments' masses to zeolites, capable of facilitating the production of effective modern concrete composites.

REFERENCES

Bataev D.K-S., Murtazayev S- A. Yu., Salamanova M.Sh., Viskhanov S.S. 2019. Utilization of Cement Kiln Dust in Production of Alkali-Activated Clinker-Free Binders/Proceedings of the International Symposium "Engineering and Earth Sciences: Applied and Fundamental Research" dedicated to the 85th anniversary of H.I. Ibragimov (ISEES 2019). Atlantis Highlights in Material Sciences and Technology (AHMST). April 2019. Vol.1.

Davidovitz, J. 2008. Geopolymer. Chemistry and applications. Saint-Quentin: Institute Geopolymer.

Duxson, P. 2007. Geopolymer technology: The current state of the art//P. Duxson, A. Fernandez, J. Provis/J. Mater. Sci. –V. 42.

Glukhovsky, V.D. Slag-alkali concrete on fine-grained aggregates [Text]/V.D. Glukhovsky//Kiev: Vishcha school. Head Publishing House, 1981.- 224 p.

Glukhovsky, V.D. 1980. Complex use of blast furnace and electrothermophosphoric slag in the production of high-strength cements and concrete/ V.D. Glukhovsky, I.A. Pashkov, B.C. Grigoryev / University News: Construction and Architecture, - No. 5.

Krivenko, P.V. 1993. The durability of slag-alkali concrete/P.V. Krivenko, K.K. Pushkareva//- Kiev: Budivelnik.

Krivenko, P.V. 2006. Physicochemical fundamentals of the durability of slag stone/P.V. Krivenko// Cement. - 1990. - No. 11. - S. 2–4.10. Lecomte, I. Microstructural comparison between geopolymers, alkali-activated slag cement and Portland cement/I. Lecomte, C. Henrist, M. Liegeois//J. Eur. Cer. Soc. – 2006. – Vol. 26.

Murtazaev, S-A.Yu. 2017. The effect of surface active sites on the reactivity of mineral additives/S-A.Yu. Murtazaev, M.Sh. Salamanova, M.S. Saidumov, Z.Kh. Ismailova//Scientific journal "Modern Science and Innovation" (Stavropol - Pyatigorsk). - 2017. - No. 2 (18).

Murtazaev, S-A.Yu. 2018. Prospects for the use of thermally activated raw materials of aluminosilicate nature/C-A.Ю. Murtazaev, M.Sh. Salamanova//Volga Scientific Journal. - 2018. - No. 2 (T.46).

Murtazayev S- A. Yu., Salamanova M.Sh., Alaskhanov A.Kh, Ismailova Z.Kh 2019. Development of Multicomponent Binders Using Fine Powders/Proceedings of the International Symposium "Engineering and Earth Sciences: Applied and Fundamental Research" dedicated to the 85th anniversary of H.I. Ibragimov (ISEES 2019). Atlantis Highlights in Material Sciences and Technology (AHMST). April 2019. Vol.1.

Nikiforov, E.A. 2011. The effect of alkaline activation on the structure and properties of diatomite/E.A. Nikiforov, V.I. Loganina, E.E. Simonov//Bulletin of BSTU named after V.G. Shukhov. 2011. - No. 2.

Rakhimova, N.R. 2009. Properties of the slag-alkaline bindings - specific surface and granulometric of ground blast furnace slags relation/N.R. Rakhimova, R.Z. Rakhimov//17. Internationale Baustofftagung, Tagungsbericht. Band 1.Weimar.

Salamanova, M.Sh. 2019. Obtaining liquid glass silicate-sodium alkaline solutions from silica-containing additives/M.Sh. Salamanova, St. A.Yu. Murtazaev//Scientific and technical journal Vestnik GGNTU. Technical science. - 2019 .– No. 1(15).

Advances in Raw Material Industries for Sustainable Development Goals – Litvinenko (Ed)

Energy estimates of relaxation and creep deformation processes of polymeric materials

A. Makarov
Vice-Rector of Science, Saint Petersburg State University of Industrial Technologies and Design, Saint Petersburg, Russia

A. Demidov
Rector, Saint Petersburg State University of Industrial Technologies and Design, Saint Petersburg, Russia

N. Pereborova
PhD, Associate Professor, Associate Professor of the Department of Intelligent Systems and Information Security Saint Petersburg State University of Industrial Technologies and Design, Saint Petersburg, Russia

M. Egorova
PhD, Associate Professor, Associate Professor of the Department of Intelligent Systems and Information Security Saint Petersburg State University of Industrial Technologies and Design, Saint Petersburg, Russia

ABSTRACT: The article considers energy estimates of nonlinear hereditary relaxation and creep processes. Polymeric materials have pronounced rheological properties including the flexible-chain structure of macromolecules that are in an oriented state and have an amorphous-crystalline structure at the supramolecular level (Pereborova et al., 2020a). According to the current views of structural physicists, at this level, the rheological properties of polymers, as a combination of elasticity, viscoelasticity and plasticity, are formed (Pereborova et al., 2020b). The decomposition of the total deformation value into the corresponding three parts is considered to be a difficult task due to their simultaneous occurrence and further development. Information about the complex pattern of distribution of material particles over relaxation and delay times can be obtained only through a physically-based analytical description of polymeric materials rheology in combination with the measurement of various deformation processes (Pereborova et al., 2020c). The accumulated experience of working with polymeric materials shows that the viscoelastic and plastic components of their deformation depend in a certain way on the level of applied mechanical action (Pereborova et al., 2020d). Hence, it follows that one creep or relaxation curve cannot be used to get any information on the delay or relaxation times (Pereborova et al., 2018a).

1 THE METHODS FOR DETERMINING THE ACTIVATION ENERGY OF RELAXATION AND CREEP DEFORMATION PROCESSES OF POLYMERIC MATERIALS

The main deformation processes of polymeric materials are relaxation and creep. To determine the activation energy of deformation processes, it is necessary to develop their mathematical models. The parameters of these processes, the relaxation and delay (creep) times, implicitly contain information about energy (Makarov et al., 2018a).

The physical meaning of the relaxation and delay time is the minimum time of conformational transition during which the assumed 'relaxing' or 'delaying' particle passes from one energy state to another overcoming some potential energy barrier (Pereborova et al., 2019a).

The authors proposed mathematical models of relaxation and creep processes based on the Cauchy probability distribution of the relaxation and delay times. It is physically feasible as this distribution has an additivity property, i.e. the sum of random variables distributed according to the Cauchy law, is also distributed according to this law (Pereborova et al., 2018b).

To illustrate the above-noted statement, it is proposed to consider a woven polymer fabric which consists of threads made up of fibres. Experimental studies confirm that complex (composite) polymeric materials behave in a similar way in the relaxation and creep processes and these processes can be described by the same mathematical models (Makarov et al., 2016).

The second convenience of the Cauchy probability distribution is in its close similarity to the normal distribution on the basis of which many physical principles can be described.

And finally, the third advantage of the Cauchy distribution is that its cumulative distribution function is an elementary function normalized arctangent (Makarov et al., 2015).

$$\varphi_t = \frac{1}{2} + \frac{1}{\pi} arctg\left(\frac{1}{b}\ln\frac{t}{t_1}\right) \tag{1}$$

in contrast to the probability integral for the normal distribution.

Here, the dimensionless logarithmic time is taken as an argument $\frac{t}{t_1}$ (t_1 - some value of base time), b - the coefficient of the intensity of relaxation or creep processes.

The elementary character of this function considerably simplifies the rearrangement in mathematical modelling of relaxation and creep.

The simplest model of the relaxation process for the case of constant deformation $\varepsilon = \text{const}$ is given by (Pereborova et al., 2018c)

$$E_{\varepsilon t} = E_0 - (E_0 - E_\infty)\varphi_{\varepsilon t} \tag{2}$$

where E_0 and E_∞- asymptotic values of the relaxation modulus

$E_{\varepsilon t} = \frac{\sigma_t}{\varepsilon}$, σ_t - time varying t stress.

Similarly, the simplest model of the creep process for the case of constant stress $\sigma = const$ is given by (Makarov et al., 2018b).

$$D_{\sigma t} = D_0 + (D_\infty - D_0)\varphi_{\sigma t} \tag{3}$$

where D_0 and D_∞ - aasymptotic compliance values $D_{\sigma t} = \frac{\varepsilon_t}{\sigma}$.

The simplest mathematical model of relaxation (1), (2) has an important advantage over other similar models as it has the smallest possible number of physically based parameters: three constants (E_0, E_∞, b_ε) and deformation-time function

$$f_{\tau_\varepsilon} = \ln\frac{t_1}{\tau_\varepsilon} \tag{4}$$

characterising the relaxation times τ_ε (Pereborova et al., 2019d).

The same can be said about the mathematical model of creep (1), (3). It also contains three physically based constants (D_0, D_∞, b_σ) and force-time function

$$f_{\tau_\sigma} = \ln\frac{t_1}{\tau_\sigma} \tag{5}$$

characterising the delay times τ_σ (Rymkevich et al., 2013)

Sufficient reliability and technical convenience follows from the analysis of the applicability of the considered simplest mathematical models of relaxation and creep used for the analytical description of the rheological properties of polymeric materials and the subsequently calculated prediction of loaded or deformable states of these materials. Due to the smallest number of

parameters-characteristics, the simplicity of their determination from short-term experiments, and clarity of their physical interpretation, the developed methods seem to be promising not only for polymers but also for a number of other solid materials (Pereborova et al., 2019c).

The simplest mathematical models of relaxation (1), (2) and creep (1), (3) can be easily generalised for the case of complex relaxation ($\varepsilon \neq const$) and complex deformation ($\sigma \neq const$) processes by using the Boltzmann-Volterra integral constitutive relations whose integral kernels are derivatives of the relaxation function or the delay function, respectively (Pereborova et al., 2018d). The mathematical model of a complex relaxation process is given by (Pereborova et al., 2018e),

$$\sigma_t = E_0 \varepsilon_t - (E_0 - E_\infty) \cdot \int_0^t \varepsilon_\theta \cdot \varphi'_{\varepsilon;t-\theta} d\theta \tag{6}$$

where $\varphi'^{\leftarrow}_{\varepsilon t}$ - relaxation kernel:

$$\varphi'_{\varepsilon t} = \frac{\partial \varphi_{\varepsilon t}}{\partial t} = \frac{1}{\pi} \cdot \frac{1}{b_\varepsilon} \cdot \frac{1}{1 + W^2_{\varepsilon t}} \cdot \frac{1}{t}, \tag{7}$$

$$\varphi_{\varepsilon t} = \frac{1}{2} + \frac{1}{\pi} \cdot arctg(W_{\varepsilon t}) \tag{8}$$

$$W_{\varepsilon t} = \frac{1}{b_\varepsilon} \cdot \ln \frac{t}{\tau_\varepsilon} = \frac{1}{b_\varepsilon} \cdot \left(\ln \frac{t}{t_1} + \ln \frac{t_1}{\tau_\varepsilon} \right) \tag{9}$$

Similarly, the mathematical model of a complex deformation process is given by (Gorshkov et al., 2013)

$$\varepsilon_t = D_0 \sigma_t - (D_\infty - D_0) \cdot \int_0^t \sigma_\theta \cdot \varphi'_{\sigma;t-\theta} d\theta \tag{10}$$

where $\varphi'^{\leftarrow}_{\sigma t}$ - delay kernel:

$$\varphi'_{\sigma t} = \frac{\partial \varphi_{\sigma t}}{\partial t} = \frac{1}{\pi} \cdot \frac{1}{b_\sigma} \cdot \frac{1}{1 + W^2_{\sigma t}} \cdot \frac{1}{t} \tag{11}$$

$$\varphi_{\sigma t} = \frac{1}{2} + \frac{1}{\pi} \cdot arctg(W_{\sigma t}), \tag{12}$$

$$W_{\sigma t} = \frac{1}{b_\sigma} \cdot \ln \frac{t}{\tau_\sigma} = \frac{1}{b_\sigma} \cdot \left(\ln \frac{t}{t_1} + \ln \frac{t_1}{\tau_\sigma} \right) \tag{13}$$

At the same time, the set of assumptions on which these mathematical models are built should be considered. First of all, the governing equations (6) and (10) of the elastic-hereditary type have a phenomenological origin (Makarov et al., 2017a). Despite the achieved success in the modelling of elastic-hereditary and more general rheological media with a stable structure, it seems to be obvious that almost any mathematical model greatly simplifies the properties of a polymer material (Demidov et al., 2017). The essence of the alternativeness of two consistent equations of nonlinear hereditary viscoelasticity (6) and (10) is in the simultaneous use of two analogies, which are deformation-time (in the case of relaxation) and force-time (in the case of creep) (Makarov et al., 2017b). There are no direct contradictions to modern kinetic views in this approach. Although, it is unusual to simultaneously use two contradicting analogies at once. The approximate nature of both analogies can be the only physical justification of this approach (Makarov et al., 2015a).

The accepted hypothesis about the feasibility of simultaneous consistent use of two logarithmically symmetric delay and relaxation kernels has an approximate nature and makes all sorts of calculation procedures easier because of a noticeable reduction in the number of parameters-characteristics. The question of preference of one kernel over another remains unclear and is subject to further research. The possibility of considering at least one of these kernels logarithmically symmetric is also not obvious (Makarov et al., 2015b).

In addition to the reduction of the number of parameters-characteristics, the simplest version of generalisation by introducing force-time and deformation-time analogies into the hereditary kernels in the normalized version plays a pivotal role.

The obtained force function of the delay times (5) and the deformation function of the relaxation times (4) in general qualitatively correspond to the modern approaches to kinetic thermofluctuation nature of 'behaviour' of the oriented amorphous-crystalline polymers (Makarov et al., 2014a).

2 CALCULATION OF THE ACTIVATION ENERGY OF RELAXATION AND CREEP DEFORMATION PROCESSES OF POLYMERIC MATERIALS

In order to verify the quantitative correspondence to these views on the curves obtained from a set of creep and relaxation of a polyester thread 83 tex., the activation energies were calculated using the well-known Arrhenius-Boltzmann formula which is given by (Demidov et al., 2006a).

$$U_\sigma = RT \cdot \left(\ln \frac{t_1}{\tau_0} - \ln \frac{t_1}{\tau_\sigma} \right), \tag{14}$$

$$U_\varepsilon = RT \cdot \left(\ln \frac{t_1}{\tau_0} - \ln \frac{t_1}{\tau_\varepsilon} \right), \tag{15}$$

where τ_0 - the parameter that has the meaning of the duration of the elementary rearrangement of 'relaxing' particles of the material $t_1 = 1$ minutes; $f_{\tau_\sigma} = \ln \frac{t_1}{\tau_\sigma}$ - force-time function, τ_σ - delay time; $f_{\tau_\varepsilon} = \ln \frac{t_1}{\tau_\varepsilon}$ - deformation-time function, τ_ε relaxation time; T - temperature ^oK; $R = kA$, k - the Boltzmann constant, A - the Avogadro number; U_σ - activation energy as a function of stress; U_ε - activation energy as a function of deformation.

In the calculation of the relaxation and creep activation energy of a polyester thread 83 tex., the following values were used: $R = 8,31$ kJ/mol*grad and $\tau_0 \cong 5 \cdot 10^{-12}$c, whence it follows that $ln \frac{t_1}{\tau_0} \cong 30$.

The calculation results are shown in Figure 1 and Figure 2. It is evident that the calculated dependencies are linear. In equations (Demidov et al., 2009)

$$U_\sigma = U_0 - \gamma \tag{16}$$

$$U_\varepsilon = U_0 - \gamma \cdot E_\tau \varepsilon \tag{17}$$

according to Figure 1 and Figure 2, it is obtained that $U_0 = 100$ kJ/mol and $\gamma \cong 4 \cdot 10^{-22}$ cm^3.

In the calculation of γ according to Figure 2, the mean value of the viscoelastic modulus was used $E_\tau = 8,5$ GPa. These values correspond to the molecular mobility of the segments or the destruction of van der Waals cross-links between the side groups.

The proximity and stability of the lines obtained in Figure 1 and Figure 2 with reference to temperature changes confirms the concept validity of the micromechanism of delay or relaxation unity in the considered temperature range, as well as, the physical validity of the analogies used. In this case, it is assumed that with a change in temperature, the physical meaning of the used parameters-characteristics is preserved but their numerical values may change.

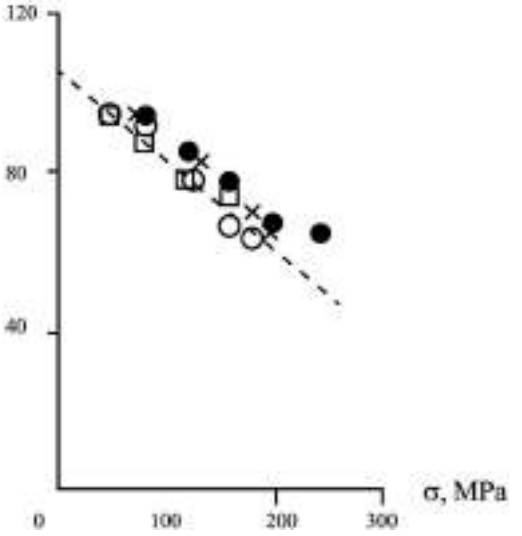

Figure 1. The dependence of activation energy on stress at temperatures 20°C (•); 40°C (x); 60°C (o); 80°C (□) of a polyester thread 83 tex.

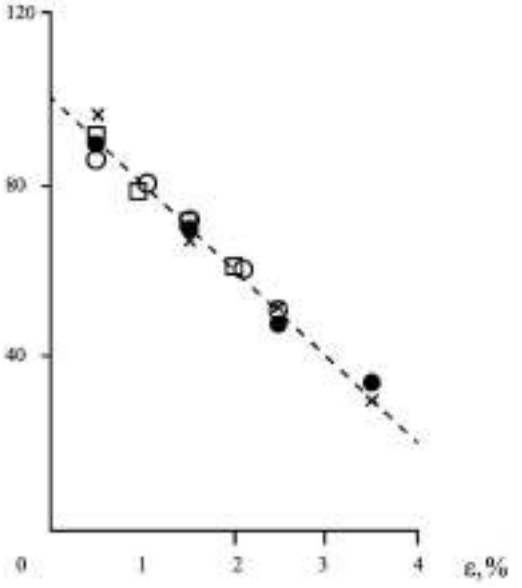

Figure 2. The dependence of the activation energy on deformation at temperatures 20°C (•); 40°C (x); 60°C (o); 80°C (□) of a polyester thread 83 tex.

Consequently, in the investigated temperature range the isothermal force-time and deformation-time analogies are generalised into the temperature-force-time and temperature-deformation-time analogies, respectively (Makarov et al., 2014b). It should be emphasised that the assumptions made in the mathematical description of the hereditary-rheological properties of polymeric materials did not affect the calculation of the activation energies of the delay times (14) and the relaxation times (15). The obtained decreasing character of the

activation energy (16), (17) corresponds to the modern approaches to the activating character of mechanical action and the leading role of thermal fluctuations at the molecular level.

3 CALCULATION OF THE COMPONENTS OF DEFORMATION OF POLYMERIC MATERIALS

The process of deformation of polymeric materials at a constant speed $\dot{\varepsilon}$ at the initial stage of the stress-strain diagram (Figure 3) is analytically described by a phenomenological integral equation of the nonlinear-hereditary type (6) which by changing the variable $s = t - \theta$ is reduced to the form

$$\sigma_t = E_o \varepsilon_t - (E_o - E_\infty) \cdot \int_0^t \varepsilon_{t-s} \cdot \varphi'_{\varepsilon s} ds \tag{18}$$

Let's take a closer look at the stress-strain diagram (Figure 3). Where $\varepsilon_t = \dot{\varepsilon} \cdot t$ and σ_t are the coordinates of a point; $\varepsilon_{t-s} = \dot{\varepsilon} \cdot (t - s)$ is the deformation under the integral sign in the formula (18).

Due to the fact that all parameters and functions included in (18) have a well-defined physical meaning, equation (18) can be considered as the mathematical model of the mechanical properties of a polymeric material with a specific spectral interpretation (Demidov et al., 2007a).

Both in the general case when $\dot{\varepsilon} \neq$const and in the special case when $\dot{\varepsilon} =$ const, elastic (ε_{to}) and absorbed (ε_{tt}) deformation components can be obtained using the formulas (Demidov et al., 2007b).

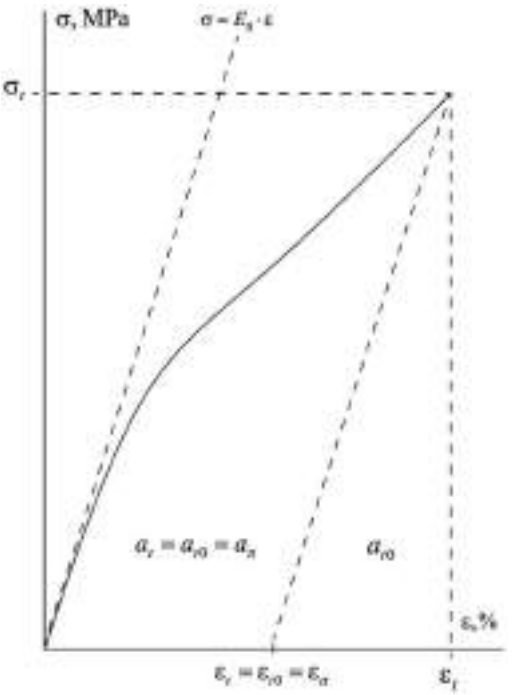

Figure 3. The decomposition scheme of the total deformation ε_t and mechanical work a_t of a polymer material into elastic $(\varepsilon_{to}, a_{to})$ and absorbed $(\varepsilon_{tt}, a_{tt})$ components.

$$\varepsilon_{to} = E_o^{-1}\sigma_t \tag{19}$$

$$\varepsilon_{tt} = \varepsilon_t - \varepsilon_{to} \tag{20}$$

or a calculated prediction based on (18) taking into account (19) and (20) (Demidov et al., 2006b).

$$\varepsilon_{tt} = \left(1 - E_\infty E_o^{-1}\right) \int_o^t \varepsilon_{t-s}\varphi'_{\varepsilon s} ds \tag{21}$$

$$\varepsilon_{to} = \varepsilon_t - \varepsilon_{tt} \tag{22}$$

Obtaining of elastic and absorbed deformation components for a polyester thread 83 tex. T=40° C, $\dot{\varepsilon} = 0,083\ c^{-1}$ is shown in Figure 4.

The calculated values of the deformation components of a polyester thread 83 tex. T=40° C, $\dot{\varepsilon} = 0,083\ c^{-1}$are given in Table 1.

The relative fractions of elastic and absorbed deformation components are equal (Demidov et al., 2006c)

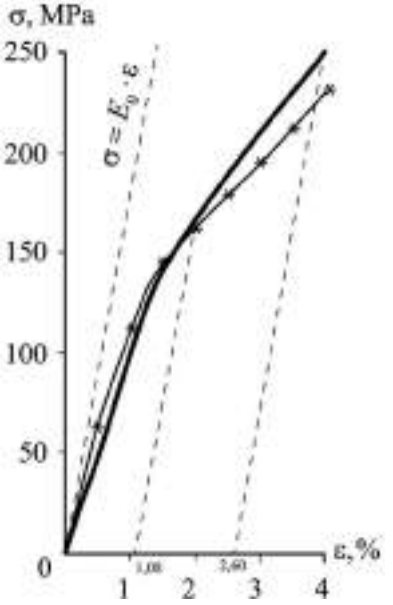

Figure 4. The stress-strain diagram of a polyester tread 83 tex., T=40° C, $\dot{\varepsilon} = 0,083\ c^{-1}$ (solid line - experiment, —*— - calculation).

Table 1. The values of the deformation components of a polyester thread 83 tex., T=40° C.

ε_t	ε_{to}	$\varepsilon_{tt} = \varepsilon_t - \varepsilon_{to}$
2,00	0,92	1,08
4,00	1,40	2,60

$$\varepsilon_{to}\varepsilon_t^{-1} = E_o^{-1}\sigma_t\varepsilon_t^{-1} \tag{23}$$

$$\varepsilon_{to}\varepsilon_t^{-1} = 1 - \left(1 - E_\infty E_o^{-1}\right)\varepsilon_t^{-1}\int_o^t \varepsilon_{t-s}\varphi'_{\varepsilon s}ds \tag{24}$$

In the calculations using (19) - (24) the corresponding viscoelastic parameters-characteristics are used $E_o,\ E_\infty, f_{\tau_\varepsilon\varepsilon},\ A_\varepsilon$.

Thus, the decomposition of the total deformation into elastic and absorbed components can be carried out either using the experimental stress-strain diagram (19), (20) or by the calculated prediction (21), (22).

5 CALCULATION OF THE ENERGY COMPONENTS OF THE DEFORMATION MECHANICAL WORK OF POLYMERIC MATERIALS

By analogy with the method of the total deformation of polymeric materials decomposition ε_t into elastic ε_{to} and absorbed ε_{tt} components, the decomposition of the specific (per unit volume) mechanical deformation work a_t into elastic a_{to} and absorbed a_{tt} components can be considered (Demidov et al., 2006d).

For a given point of the stress-strain diagram (Figure 3) with coordinates ε_t and σ_t the specific mechanical work is calculated by the formula

$$a_t = \int_o^{\varepsilon_t} \sigma_t d\varepsilon \tag{25}$$

Taking into account (18), from (25) the prediction formula is developed (Demidov et al., 2007c).

$$a_t = 0,5E_o\varepsilon_t^2 - \dot{\varepsilon}(E_o - E_\infty)\int_o^t\int_o^t \varepsilon_{t-s}\varphi'_{\varepsilon s}dsdt \tag{26}$$

The elastic component of specific mechanical work (Stalevich et al., 2003).

$$a_{to} = 0,5E_o^{-1}\sigma_t^2 \tag{27}$$

and, accordingly, the elastic fraction of mechanical work (a_{to}/a_t) is obtained for a given point of the diagram with coordinates ε_t and σ_t or directly using the formula (25) (Makarov, 2002)

$$\frac{a_{to}}{a_t} = \frac{\sigma_t^2}{2E_o\int_o^{\varepsilon_t}\sigma_\mathrm{t}d\varepsilon} \tag{28}$$

or by the prediction using the formula (28) with the help of (18) (Stalevich et al., 2002a)

$$\frac{a_{to}}{a_t} = \frac{E_o^2\varepsilon_t^2 + \left(\int_o^t \varepsilon_{t-s}E'_{\varepsilon s}ds\right)^2 + 2\varepsilon_t E_o \int_o^t \varepsilon_{t-s}E'_{\varepsilon s}ds}{E_o^2\varepsilon_t^2 + 2\dot{\varepsilon}E_o \int_o^t\int_o^t \varepsilon_{t-s}E'_{\varepsilon s}dsdt} =$$
$$= \frac{\varepsilon_t^2 + (1-c)^2\left(\int_o^t \varepsilon_{t-s}\phi'_{\varepsilon s}ds\right)^2 + 2\varepsilon_t(1-c)\int_o^t \varepsilon_{t-s}\phi'_{\varepsilon s}ds}{\varepsilon_t^2 + 2\dot{\varepsilon}(1-c)\int_o^t\int_o^t \varepsilon_{t-s}\phi'_{\varepsilon s}dsdt} \quad (29)$$

where $c = \frac{E_\infty}{E_o}$.

The absorbed part of the specific mechanical work (Stalevich et al., 2002b)

$$a_{tt} = a_t - a_{to} \quad (30)$$

or its relative part

$$\frac{a_{tt}}{a_t} = 1 - \frac{a_{to}}{a_t} \quad (31)$$

are also obtained in any of the two mentioned ways (Stalevich et al., 2000).

For example, the values of the specific work and its elastic and absorbed components for a polyester thread 83 tex., t=40° C, at a deformation speed $\dot{\varepsilon} = 0,083\ c^{-1}$ are given in Table 2.

The calculation results of the fraction of elastic component of mechanical work $\frac{a_{to}}{a_t}$ depending on the deformation ε according to (28) - (31) are shown in Figure 5.

As it is evident from the graph (Figure 5), the fraction of the component a_{tt} in mechanical work increases, the fraction of the component a_{to} decreases with increasing deformation ε (Makarov et al., 2014c). This means that in order to return to its original state, according to the law of conservation of energy, the material needs to transfer from the external environment the more (in percentage) energy, the more it is deformed. On the other hand, this fact indicates the emerging role of the viscoelastic factor with the increase of deformation (Potapov et al., 2018).

As the result, the methods for obtaining the elastic component of mechanical work from the stress-strain diagrams or using the calculated prediction at the stage of non-destructive mechanical action are proposed (Blinov te al., 2018). The proximity of elastic components values obtained from the measured or predicted stress-strain diagram confirms the quite satisfactory reliability of physical and mechanical properties modelling of a thread in the form of a nonlinear hereditary equation (18) (Vasil'eva et al., 2016).

Table 2. The values of the specific deformation work (a_t), its elastic (a_{to}) and absorbed (a_{tt}) components for the deformation values ε_t of a polyester thread 83 tex., t=40° C at a deformation speed $\underline{\varepsilon} = 0,083c^{-1}$.

ε_t, %	a_t, MPa	a_{to}, MPa	a_{tt}, MPa
2,00	1,86	0,76	1,10
4,00	5,42	1,75	3,67

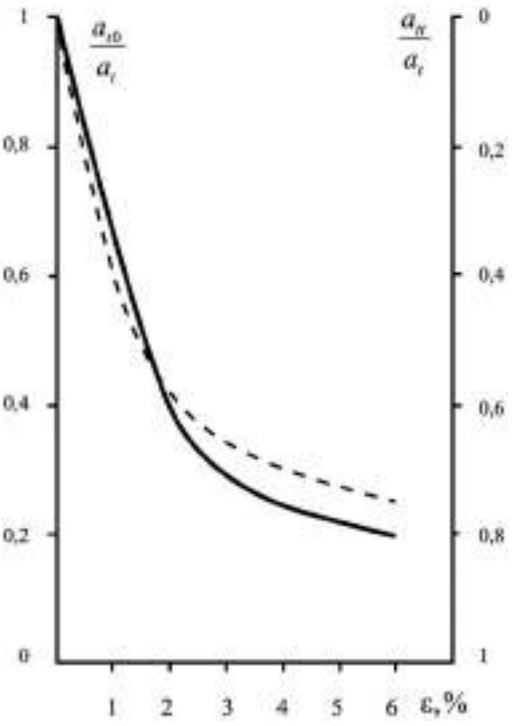

Figure 5. The fraction of elastic component $\frac{a_{1D}}{a_t}$ and absorbed component $\frac{a_{II}}{a_t}$ of mechanical work during deformation of a polyester thread 83 tex., T=40° C depending on the deformation ε,% (solid line - experiment, - - - - calculation).

6 CONCLUSION

In sum, the energy characteristics of relaxation and creep processes were considered. Specifically, the methods for decomposition of the deformation mechanical work into two elastic-reversible and viscoelastic-plastic components are developed. The proximity of the values of elastic components obtained from the measured and predicted stress-strain diagram confirms the reliability of the mechanical properties modelling of a polymeric material in the form of a nonlinear hereditary governing equation.

The methods for decomposition of deformation of polymeric materials into their components: elastic deformation, highly elastic deformation and plastic deformation allows to better understand the nature of deformation processes. Taking into account the plastic component of deformation helps to improve the accuracy and, consequently, the reliability of predicting both simple and complex nonlinear hereditary viscoelastic processes.

The proximity of the energy parameters calculated from the delay times and from the relaxation times, their invariability in the temperature range, and the decreasing nature of the activation energy confirm the thermofluctuation interpretation of the viscoelastic nonlinearity of the delay and relaxation kernels at the level of intermolecular interaction and internal rotation in chemical bonds.

The analysis of the activation parameters calculated from the obtained delay times and relaxation times confirms the consistency of the hypothesis about the activating nature of mechanical action at the level of intermolecular interactions and internal rotation. It also confirms the consistency of the thermofluctuation interpretation of viscoelastic nonlinearity of the used delay and relaxation kernels. This substantiates the proposed methods for the analytical description of the hereditary rheological properties of polymeric materials.

FUTURE RESEARCH AND ACKNOWLEDGEMENTS

The study was funded within the framework of the state assignment of the Ministry of Science and Higher Education of the Russian Federation, Project No. FSEZ-2020-0005.

REFERENCES

Blinov, P.A., Dvoynikov, M.V. (2018) Rheological and Filtration Parameters of the Polymer Salt Drilling Fluids Based on Xanthan Gum. *Journal of Engineering and Applied Sciences*, 13: 5661–5664. DOI: 10.36478/2018.5661.5664

Demidov, A.V., Makarov, A.G., Stalevich, A.M. (2006a) The criteria of optimal selection of mathematical model of textile materials viscoelasticity. *Izvestiya Vysshikh Uchebnykh Zavedenii, Seriya Teknologiya Tekstil'noi Promyshlennosti*, Vol. 293, No 5, pp. 21–25. eid=2-s2.0-34247548784

Demidov, A.V., Makarov, A.G., Stalevich, A.M., Petrova, L.N., Chelishev, A.M. (2006b) Research of changes of deformation properties of polyester threads depending on twist amount. *Izvestiya Vysshikh Uchebnykh Zavedenii, Seriya Teknologiya Tekstil'noi Promyshlennosti*, Vol. 292, No 4, pp. 9–13. eid=2-s2.0-33845499474

Demidov, A.V., Makarov, A.G., Stalevich, A.M. (2006c) Methods of computer analysis of viscoelasticity of technical materials. *Izvestiya Vysshikh Uchebnykh Zavedenii, Seriya Teknologiya Tekstil'noi Promyshlennosti*, Vol. 291, No 3, pp. 13–17. eid=2-s2.0-37849188658

Demidov, A.V., Makarov, A.G., Stalevich, A.M. (2006d) Definition of the mechanical characteristics of textile stuffs at variable temperature. *Izvestiya Vysshikh Uchebnykh Zavedenii, Seriya Teknologiya Tekstil'noi Promyshlennosti*, Vol. 294, No 6, pp. 15–18. eid=2-s2.0-34250009041

Demidov, A.V., Makarov, A.G., Stalevich, A.M. (2007a) Definition of the computer forecasting trends of deformation properties of textile stuffs. *Izvestiya Vysshikh Uchebnykh Zavedenii, Seriya Teknologiya Tekstil'noi Promyshlennosti*, Vol. 297, No 2, pp. 14–17. eid=2-s2.0-38849203122

Demidov, A.V., Makarov, A.G., Stalevich, A.M. (2007b) System analysis of viscoelasticity of textile stuffs. *Izvestiya Vysshikh Uchebnykh Zavedenii, Seriya Teknologiya Tekstil'noi Promyshlennosti*, Vol. 298, No 3, pp. 11–14. eid=2-s2.0-34648822922

Demidov, A.V., Makarov, A.G., Stalevich, A.M. (2007c) Predicting the nonlinear hereditary viscoelasticity of polymers. *Journal of Applied Mechanics and Technical Physics*, Vol. 48, No 6, pp. 897–904. DOI: 10.1007/s10808-007-0114-8

Demidov, A.V., Makarov, A.G., Stalevich, A.M. (2009) A version of modeling of nonlinear-hereditary viscoelasticity of polymer materials. *Mechanics of Solids*, Vol. 44, No 1, pp. 122–130. DOI: 10.3103/S0025654409010130

Demidov, A.V., Makarov, A.G., Pereborova, N.V., Egorova, M.A. (2017) Forecasting of deformation-relaxation properties of poly amide fabric used to make the canopy. *Izvestiya Vysshikh Uchebnykh Zavedenii, Seriya Teknologiya Tekstil'noi Promyshlennosti*, Vol. 367, No 1, pp. 250–258. eid=2-s2.0-85033239149

Gorshkov, A.S., Makarov, A.G., Romanova, A.A., Rymkevich, P.P. (2013) Modelling of directed polymers deformation processes based on the description of the kinetics of supramolecular structures separated by energy barriers. *Magazine of Civil Engineering*, Vol. 44, No 9, pp. 76-83+103-104. DOI: 10.5862/MCE.44.10

Makarov, A.G. (2002) Determining the analytical correlation between the standardized nuclei of relaxation and creep in textile materials. *Izvestiya Vysshikh Uchebnykh Zavedenii, Seriya Teknologiya Tekstil'noi Promyshlennosti*, Vol. 266, No 2, pp. 13–17. eid=2-s2.0-0036931214

Makarov, A.G., Pereborova, N.V., Egorova, M.A., Wagner, V.I. (2014a) Modeling and forecasting viscoelastic properties of textile materials with a complex structure. *Izvestiya Vysshikh Uchebnykh Zavedenii, Seriya Teknologiya Tekstil'noi Promyshlennosti*, Vol. 354, No 6, pp. 120–124. eid=2-s2.0-84937439497

Makarov, A.G., Pereborova, N.V., Egorova, M.A., Wagner, M.A. (2014b) Ways of modeling deformation and relaxation properties of textile materials with a complex structure. *Izvestiya Vysshikh Uchebnykh Zavedenii, Seriya Teknologiya Tekstil'noi Promyshlennosti*, Vol. 351, No 3, pp. 110–115. eid=2-s2.0-84937410003

Makarov, A.G., Pereborova, N.V., Wagner, V.I., Rymkevich, P.P., Gorshkov, A.S. (2014c) The Basis of Spectral-Temporal Analysis of Relaxation and Deformation Properties of Polymeric Materials in Textile and Ligt Industry. *Izvestiya Vysshikh Uchebnykh Zavedenii, Seriya Teknologiya Legkoi Promyshlennosti*. Vol. 23, No 1. pp. 24–29.

Makarov, A.G., Slutsker, G.Y., Drobotun, N.V. (2015) Creep and fracture kinetics of polymers. *Technical Physics*, Vol. 60, No 2, pp. 240–245. DOI: 10.1134/S1063784215020152

Makarov, A.G., Demidov, A.V., Pereborova, N.V., Egorova, M.A. (2015a) Modeling and prediction of estimated relaxation and deformation properties of the polymer parachute line. *Izvestiya Vysshikh Uchebnykh Zavedenii, Seriya Teknologiya Tekstil'noi Promyshlennosti*, Vol. 360, No 6, pp. 194–205. eid=2-s2.0-84976560627

Makarov, A.G., Pereborova, N.V., Wagner, V.I., Vasileva, E.K. (2015b) Development of methodology for the comparative analysis of deformation and relaxation properties of aramid yarns and textile materials based on them. *Izvestiya Vysshikh Uchebnykh Zavedenii, Seriya Teknologiya Tekstil'noi Promyshlennosti*, Vol. 359, No 5, pp. 48–58. eid=2-s2.0-84971636036

Makarov, A.G., Slutsker, G.Y., Gofman, I.V., Vasil'eva, V.V. (2016) Initial stage of stress relaxation in oriented polymers. *Physics of the Solid State*, Vol. 58, No 4, pp. 840–846. DOI: 10.1134/S1063783416040132

Makarov, A.G., Pereborova, N.V., Egorova, M.A., Egorov, I.M. (2017a) Quality analysis of deformation-relaxation properties of aramid cords mountain rescue appointments. *Izvestiya Vysshikh Uchebnykh Zavedenii, Seriya Teknologiya Tekstil'noi Promyshlennosti*, Vol. 368, No 2, pp. 309–313. eid=2-s2.0-85035207042

Makarov, A.G., Pereborova, N.V., Egorova, M.A., Egorov, I.M. (2017b) Mathematical modeling of deformation-relaxation processes polymeric materials in conditions of variable temperatures. Izvestiya Vysshikh Uchebnykh Zavedenii, Seriya Teknologiya Tekstil'noi Promyshlennosti, Vol. 370, No 4, pp. 287–292. eid=2-s2.0-85057142312

Makarov, A.G., Pereborova, N.V., Kozlov, A.A., Shvankin, A.M. (2018a) Computer-Assisted Prediction and Qualitative Analysis for Polymer Parachute Cords *Fibre Chemistry*, Vol. 50, No. 3, pp. 239–242. DOI 10.1007/s10692-018-9968-1

Makarov, A.G., Pereborova, N.V., Vagner, V.I., Egorova, M.A., Klimova, N.S. (2018b) Spectral Analysis of Viscoelastic Creep of Geotextiles. *Fibrie Chemistry*, Vol. 50, No 4, pp. 378–382. DOI 10.1007/s10692-019-09993-4

Pereborova, N.V., Demidov, A.V., Makarov, A.G., Klimova, N.S. (2018a) Modeling of Deformation-Relaxation Processes of Aramid Textile Materials – the Foundation for Analyzing Their Operational Properties. *Fibre Chemistry*, Vol. 50, No. 2, pp. 104–107. DOI 10.1007/s10692-018-9941-z

Pereborova, N.V., Makarov, A.G., Egorova, M.A., Kozlov, A.A., Konovalov, A.S. (2018b) Methods of simulation and comparative analysis of shadow and deformation-reducing properties of aramide textile materials. *Izvestiya Vysshikh Uchebnykh Zavedenii, Seriya Teknologiya Tekstil'noi Promyshlennosti*, Vol. 375, No 3, pp. 253–257. eid=2-s2.0-85059766891

Pereborova N.V., Makarov A.G., Kozlov A.A., Vasil'eva E.K. (2018c) Development of Integral Optimality Criteria for Mathematical Modeling of Relaxation/Recovery Processes in Polymer Textile Materials. *Fibrie Chemistry*, Vol. 50, No 4, pp. 306–309. DOI 10.1007/s10692-019-09981-8

Pereborova, N.V., Makarov, A.G., Egorova, M.A., Klimova, N.S. (2018d) Methods of increasing the competitiveness of domestic aramid textile materials based on complex analysis of their functional properties. *Izvestiya Vysshikh Uchebnykh Zavedenii, Seriya Teknologiya Tekstil'noi Promyshlennosti*, Vol. 378, No 6, pp. 267–272. eid=2-s2.0-85072335464

Pereborova, N.V., Demidov, A.V., Makarov, A.G., Klimova, N.S., Vasileva, E.K. (2018e) Methods of mathematical modeling and qualitative analysis of relaxation-deformation processes of aramide textile materials. *Izvestiya Vysshikh Uchebnykh Zavedenii, Seriya Teknologiya Tekstil'noi Promyshlennosti*, Vol. 374, No 2, pp. 251–255. eid=2-s2.0-85056451197

Pereborova, N.V., Makarov, A.G., Vasil'eva, E.K., Shvankin, A.M., Egorov, I.M. (2019a) Mathematical Modeling and Computed Prediction of Viscoelastic Creep in Geotextile Nonwoven Fabrics. *Fibre Chemistry*, Vol. 50, No 6, pp. 487–490. DOI 10.1007/s10692-019-10015-6

Pereborova, N.V., Makarov, A.G., Egorova, M.A., Kozlov, A.A. (2019b) Mathematical Modeling and Comparative Analysis of Deformation/Recovery Properties and Shrinkage of Aramid Textile Materials. *Fibre Chemistry*, Vol. 50, No 5, pp. 468–472. DOI 10.1007/s10692-019-10010-x

Pereborova, N.V., Makarov, A.G., Egorova, M.A., Klimova, N.S. (2019c) Improving the Competitiveness of Aramid Textile Materials Based on Mathematical Modeling and Analysis of Their Performance Properties. *Fibre Chemistry*, Vol. 50, No 6, pp. 569–572. DOI 10.1007/s10692-019-10030-7

Pereborova, N.V., Makarov, A.G., Shvankin, A.M., Egorova, M.A., Abramova, I.V. (2020a) Modeling and Qualitative Analysis of Creep Processes of Geotextile Nonwovens -A Foundation for Enhancing their Competitiveness. *Fibre Chemistry*, Vol. 51, No. 5, pp. 397–400. DOI 10.1007/s10692-020-10119-4

Pereborova, N.V., Makarov, A.G., Shvankin, A.M., Egorova, M.A., Korobovtseva, A.A. (2020b) Predicting Creep and Deformation and Recovery Processes of Geotextile Nonwovens. *Fibre Chemistry*, Vol. 51, No. 5, pp. 401–403. DOI 10.1007/s10692-020-10120-x

Pereborova, N.V., Makarov, A.G.,Egorova, M.A., Egorov, I.M. (2020c) Methods of Modeling and Computer-Aided Prediction of Relaxation of Medical-Purpose Textile Elastomers. *Fibre Chemistry*, Vol. 51, No. 6, pp. 467–470. DOI 10.1007/s10692-020-10136-3

Pereborova, N.V., Makarov, A.G.,Egorova, M.A., Egorov, I.M. (2020d) Methods modeling and Computer-Aided Prediction of Strain and Relaxation Processes of Medical-Purpose Textile Elastomers. *Fibre Chemistry*, Vol. 51, No. 6, pp. 471–474. DOI 10.1007/s10692-020-10137-2

Potapov, A., Makhov, V. (2018) Methods for Nondestructive Testing and Diagnostics of Durability of Articles Made of Polymer Composite Materials. *Russian Journal of Nondestructive Testing*. 54. 151–163. 10.1134/S1061830918030087.

Rymkevich, P.P., Romanova, A.A., Golovina, V.V., Makarov, A.G. (2013) The energy barriers model for the physical description of the viscoelasticity of synthetic polymers: Application to the uniaxial orientational drawing of polyamide films. *Journal of Macromolecular Science, Part B: Physics*, Vol. 52, No 12, pp. 1829–1847. DOI: 10.1080/00222348.2013.808906

Stalevich, A.M., Makarov, A.G. (2000) Determining the inherent viscoelastic relaxation spectrum for synthetic filaments. *Izvestiya Vysshikh Uchebnykh Zavedenii, Seriya Teknologiya Tekstil'noi Promyshlennosti*, Vol. 255, No 3, pp. 8–12. eid=2-s2.0-0034436083

Stalevich, A.M., Makarov, A.G. (2002a) Forecasting the deformation recovery process and the reverse relaxation in polymer materials. *Izvestiya Vysshikh Uchebnykh Zavedenii, Seriya Teknologiya Tekstil'noi Promyshlennosti*, Vol. 267, No 3, pp. 10–13. eid=2-s2.0-0038128574

Stalevich, A.M., Makarov, A.G., Saidov, E.D. (2002b) Elastic components in the stress/strain curve for a synthetic fibre yarn. *Izvestiya Vysshikh Uchebnykh Zavedenii, Seriya Teknologiya Tekstil'noi Promyshlennosti*, Vol. 268, No 4-5, pp. 15–18. eid=2-s2.0-0037742684

Stalevich, A.M., Makarov, A.G., Saidov, E.D. (2003) Relaxation spectrometry of synthetic yarns. *Izvestiya Vysshikh Uchebnykh Zavedenii, Seriya Teknologiya Tekstil'noi Promyshlennosti*, Vol. 270, No 1, pp. 16–22. eid=2-s2.0-2642532049

Vasil'eva, M.A., Feit, S. (2016) Investigation of polymer material of the working camera-channel of the magnetic pumps for heavy oil. *Journal of Mining Institute*, 221, p. 651. DOI: 10.18454/pmi.2016.5.651

Advances in Raw Material Industries for Sustainable Development Goals – Litvinenko (Ed)

Increasing the corrosion resistance of tubular furnace elements at temperature range 400-700°C in accelerated testing for real operational conditions

Bashar Issa
PhD student, Faculty of Mineral Raw Materials Processing, Saint-Petersburg Mining University, Saint-Petersburg, Russia

Vladimir Yu. Bazhin
Doctor of Engineering, Professor, Saint-Petersburg Mining University, Saint-Petersburg, Russia

Tatiana A. Aleksandrova
Candidate of Engineering Sciences, Saint-Petersburg Mining University, Saint-Petersburg, Russia

ABSTRACT: The presence of impurities in the crude oil especially trace metals and chlorides are the primary responsible for the deterioration of the coiled-pipes of the tubular furnaces, and therefore for their premature failure. Mainly as a result of the acceleration of different types of corrosion processes in addition to the catalyst poisoning reaction. The small quantities of such these impurities which are existed in the heavy crude oils are large enough to cause significant industrial problems annually, environmental hazards and economic losses. Coiled-pipes of tubular furnaces are subject to extreme operating conditions from the prolonged exposure to the high temperatures and the aggressive environments on their alloys, because of these types of furnaces are constantly working (24 hours a day — 7 days a week). The inevitable consequences for the coiled-pipes utilization (or other elements) of the tubular furnaces can be summarized as; the reducing of the corrosion resistance of the coiled-pipes alloys, the increasing of the tendency to unexpected coiled-pipes ruptures, releasing flammable materials, fires, explosions, injuries and unfortunately deaths. As long as corrosion is the most dangerous process, which can negatively affect the elements of the tubular furnaces and especially on the coiled-pipes, this research is devoted to find a solution for very important industrial problem of the premature failure of the coiled-pipes of the tubular furnaces of the dewatering and desalting installation at oil refinery «ELOY» which is located in Syria by using two furnaces to make a closed small-scale heating cycle with temperature range 400 - 700°C. Role of different kinds of chlorides which are existed in the Syrian heavy crude oil is carefully studied due to their high concentrations; accordingly, a whole mechanism for chloride corrosion cycle inside the coiled-pipes of tubular furnaces is suggested. Roles of trace metals which are existed in the Syrian heavy crude oil are also studied in deep in addition to their possible roles in the resulting corrosion types. The responsible mechanisms for each type of corrosion are proposed too.

1 GENERAL INSTRUCTIONS

1.1 *Introduction*

After an accident occurred at the studied oil refinery in Syria because of the corrosion of the coiled-pipes of the tubular furnace, this led to cease the production for few months, which led to import of oil-products from abroad, which in turn exacerbated the economic burden. Scientific research about corrosion and corrosion resistance at temperature range 400 - 700°C and

about the role of trace metals which are existed in both phases of crude oil on scales and deposits forming (corrosion products) in the inner surface of the coiled-pipes of the tubular furnace are almost rare in the literatures, which reflects the importance of this research.

Spontaneous physicochemical destruction and premature failure of the coiled-pipes of the tubular furnaces at oil refineries, leading to irretrievable loss of their alloys, due to their chemical or electrochemical interaction with the flowing crude oil can be defined as corrosion. As a result of the corrosion processes, the inner surface of the coiled-pipes is visibly destroyed (Saakyan et al. 1982, Isaev1997 & Goldobina et al. 2019, Ivanik et al. 2017). A large amount of crude oil as well as natural gas is lost annually from through defects and the premature failures in oil- and/or gas-pipelines and coiled-pipes of tubular furnaces, which leads to environmental pollution, emergency situations, oil and/or gas shortages to consumers, and penalties (Bakesheva et al. 2019). For the purpose of coiled-pipes, trunks and oil and/or gas pipelines safe operation, two types of wall metal anticorrosion protection can be generally used - the passive (insulation coating) protection and the active (electrochemical) protection (Tsenev et al. 2017). Corrosion processes require annually huge repair and maintenance expenses to the oil, gas and petrochemical industry (Bobritsky & Yufin 1988, Kondrasheva et al. 2014 & Volovikov 2010), which can cause serious injuries and unfortunately deaths, explosions, fires, catastrophic disasters, environmental pollution and economical losses every year; due to the mutual effect of both crude oil impurities and the temperature on the coiled-pipes of the tubular furnaces (Alekseev & Smirnov 1955, Alekseev 1972 & Baratov et al. 1990).

Syria is a relatively small oil producer, according to global or even regional standards, that accounted for just 0.5% of the global production in 2010, falling to less than 0.05% by 2016 according to the International Monetary Fund, i.e. the Syrian oil production has fallen by ten times in six years due to the consequences of the devastating war, the accompanying international sanctions and the deterioration of installations and equipments.

1.2 *Aims of study*

The aims of this research are: to determine the possible roles of metals and/or metallic components in the crude oil on the severe corrosion at the studied temperature range; to determine the most possible corrosion types; and to determine the effectiveness of a specific inhibitor in reducing the corrosion rate of the coiled-pipe of tubular furnaces.

1.3 *Used methods*

Chemical analysis for determination the metals content in Syrian heavy crude oils is done by burning the Syrian heavy crude oil sample and then by analyzing the obtained carbon residual by using sequential X-ray fluorescence spectrometer XRF-1800; Chemical and microstructural analysis for determination the metals content in coiled-pipes is done by using an analytical scanning electron microscope — VEGA3 TESCAN; X-ray microanalysis for the determination of phase's composition in coiled-pipe is done by using oxford INCA energy EDS; Determination of corrosion ability of the coiled-pipe and the effectiveness of studied inhibitor in reducing the corrosion rate of the coiled-pipes at the studied temperature range is done by using weight loss method.

2 RESULTS

2.1 *Closed small-scale heating cycle*

The closed small-scale heating cycle consists of four basic elements, as shown in Figure 1: horizontal tube furnace, pump (air-cooled thermic fluid pump - AT. DIN24256), silit (silicon carbide) furnace and system filling valve (VF06 Sealed System Filling Valve). Inside the horizontal (ceramic) tube furnace (with the dimensions 30cm (length)* 3.3cm (diameter)), we put

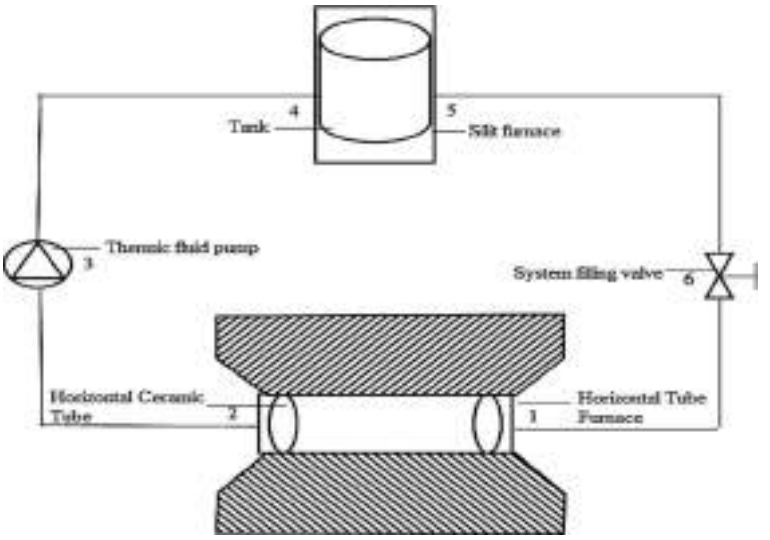

Figure 1. Closed small-scale heating cycle.

a stainless steel tube (AISI 321 grade) (with the dimensions 30cm length * 2.8cm diameter * 0.5cm thickness) and inside this stainless tube we fixed a coupon (with the dimensions 3cm length * 1cm width * 0.5cm thickness) from the same alloy of the coiled-pipe of the tubular furnace between two obstacles (barriers/pieces) of the same alloy of the stainless steel alloy in order to stay in the horizontal (ceramic) tube and not to move with circulating (flowing) emulsion. Inside the silit furnace (heating camera with the dimensions 250mm height * 160mm length * 160mm width), we put tank (with the dimensions 23cm height * 14cm length * 14cm width) and we put inside the tank 4L of the flowing emulsion. The flowing emulsion consists of a mixture of laboratory prepared salt electrolyte (90% = 3.6L) (with the composition shown in the Table 5) and Syrian heavy crude oil (10% = 400mL)) (with metal composition shown in the Table 4). The two furnaces were set at the same studied temperature. Tests were performed with and without the studied inhibitor by applying weight loss method.

The surface of each coupon was abraded mechanically with (320, 400 and 600) grades of SiC (silicon carbide) abrasive paper, washed with distilled water, dried with clean tissue paper, immersed in ethanol, dried with clean tissues paper and weighted before and after the experiment, then the weight loss was determined. The corrosion rate and the effectiveness of the inhibitor in reducing the corrosion rate were calculated by using the following equation:

$$CR_i, mdd = \frac{\Delta m, g}{A, Cm^2.t, sec}(10^5)(86400)$$

$$\%_i = \frac{CR_0 - CR_i}{CR_0}(100)$$

Where: CR_i — Corrosion rate with the studied inhibitor; CR_0 — Corrosion rate without inhibitor; mdd = $mg/dm^2/day$; Δm — Weight loss of the coupon of the coiled-pipe; A — Surface area of the coupon; $\%_i$ — Inhibitor effectiveness in reducing the corrosion rate.

The studied emulsion enters the stainless-steel tube at point 1, which is placed inside the horizontal tube furnace, where the coupon of the coiled-pipe is fixed between two obstacles of the same alloy of the stainless steel. The emulsion exits from the stainless-steel tube at point 2 to enter the thermic fluid pump at point 3 in order to continue to reach the silit furnace to enter the tank at point 4 and to exit at point 5 to continue to enter the filling valve at point 6. All the connecting lines were made of thick wall copper tubing.

The two furnaces ensure that the temperature of the flowing emulsion will be constant inside the stainless-steel tube, where the coupon is placed in. The filling valve (VF06 Sealed System Filling Valve) and the thermic fluid pump (AT. DIN24256) control the flow through the stainless-steel tube (flow rate 1L/min) and to assure proper performance of the closed small-scale heating cycle. The filling valve for closed heating systems (VF06) is a combination-filling valve for sealed heating systems, incorporating a pressure-reducing valve, stop valve, a non-return valve and hose connections. The thermic fluid pump –(AT. DIN 24256) with no additional cooling required (air-cooled).

It should be noted that the composition of the flowing emulsion under the experimental condition is 90% laboratory prepared salt electrolyte: 10% heavy Syrian crude oil, while the percentage of the formation water (salt electrolyte) of the flowing emulsion under the real operative condition inside the coiled-pipes of the tubular furnace is only 0.5% formation water according to the Syrian standards (and according to the Russian requirements 0.2% formation water), because of that; the real corrosion rates can be calculated by multiplying the accelerated corrosion rates by 0.5/90 for the Syrian requirements (and by 0.2/90 for the Russian requirements).

The cause of use laboratory prepared salt electrolyte instead of the formation water and the cause of use the ratio (90% laboratory prepared salt electrolyte: 10% heavy Syrian crude oil) instead of the ratio (99.5% heavy Syrian crude oil: 0.5% formation water (salt electrolyte)) are due to two reasons: Firstly, to accelerate the process of corrosion, since the effectiveness of the studied inhibitor in reducing the corrosion rate will not change. Secondly, to follow the safety procedures because the crude oil is a flammable liquid and the experiments required high temperatures.

2.2 *Microstructure and elemental composition of coiled-pipe*

The alloy grade of coiled-pipes of tubular furnaces which is used in the studied oil refinery is «10X17H13M2T» — austenitic steel, its chemical composition is shown in Table 1.

The structure of the coiled-pipe is shown under the scanning electron microscope in spectra, as shown in figures (2 - For non-affected (clean) areas (sites), without any signs of corrosion and 3 - For affected (corroded) (transitional) areas (sites)) and their composition are shown in tables (2 and 3).

Table 1. Chemical composition of steel «10X17H13M2T».

C, %	Si, %	Mn, %	Ni, %	S, %	P, %	Cr, %	Mo, %	Cu, %	Fe, %
≤0.1	≤0.8	≤2	12-14	≤0.02	≤0.035	16-18	2-3	≤0.3	Balance

Table 2. Analytical composition of eight spectra of coiled-pipe in non-affected (clean) areas (sites).

№ Spectrum	O, %	Si, %	Ni, %	Mn, %	Mo, %	Cr, %	Fe, %	Total
Spectrum 1	1.01	0.2	9.18	0.1	0.61	8.54	80.36	100
Spectrum 2	0.25	0.44	6.41	0.54	1.25	11.39	79.72	100
Spectrum 3	0.36	0.59	10.25	1.05	0.96	14.11	72.68	100
Spectrum 4	1.95	0.32	12.15	0.35	2.01	13.56	69.66	100
Spectrum 5	—	0.41	9.73	0.12	1.85	11.03	76.86	100
Spectrum 6	2.47	0.26	4.26	1.36	1.31	14.73	75.61	100
Spectrum 7	—	0.11	7.12	0.34	0.31	12.67	79.45	100
Spectrum 8	1.65	0.61	11.54	0.21	0.97	11.93	73.09	100
Min.	—	0.11	4.26	0.1	0.31	8.54	69.66	
Max.	2.47	0.61	12.15	0.54	2.01	14.73	80.36	

Table 3. Analytical composition of three spectra of coiled-pipe in affected (corroded) (transitional) areas.

№ Spec.	Fe %	V %	Cl %	O %	Mn %	Cr %	Co %	Ni %	Cu %	Zn %	Sn %	Si %	S %
Spec.11	7.85	11.24	4.13	4.58	—	0.73	—	22.96	41.37	2.14	4.39	0.61	—
Spec.12	3.98	—	—	—	—	—	0.82	37.64	50.21	5.5	1.86	—	—
Spec.15	7.84	13.43	9.71	5.01	1.36	2.61	17.03	20.05	21.76	1.25	11.39	0.57	0.63
Min.	3.98	—	—	—	—	—	—	20.05	21.76	1.25	1.86	—	—
Max.	7.85	13.43	9.71	5.01	1.36	2.61	17.03	37.64	50.21	5.5	11.39	0.61	0.63

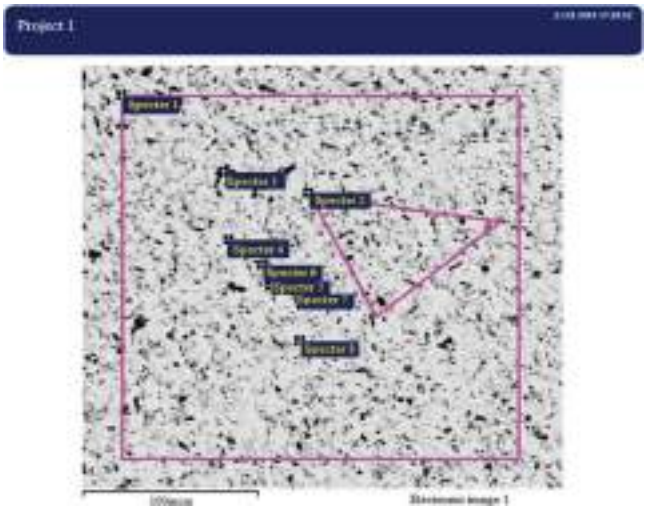

Figure 2. Electronic image-position of eight spectra of coiled-pipe in non-affected area — scale 1: 100.

In Figure 3 the left side is the material of the coiled-pipe, and the right side is the scale, formed as a result of the long stay of the coiled-pipes under the influence of the burners of the tubular furnace in addition to the effects of different types of corrosion processes. Between the material of the coiled-pipe and the resulting scale there is the transitional zone of corrosion.

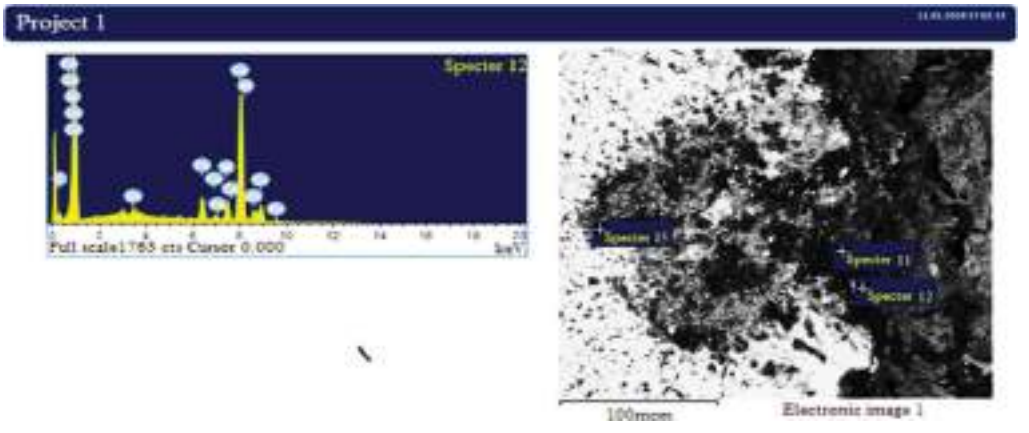

Figure 3. Electronic image-position of three spectra of coiled-pipe in affected (transitional) zone — scale 1: 100.

2.3 *Trace metals in Syrian heavy crude oil*

6.0259g of Syrian heavy crude oil was placed in a crucible, the crucible was placed inside the heating chamber of the silit furnace, where the Syrian heavy crude oil was burned at 350°C and the furnace was turned-off immediately after the self-ignition is stopped, the crucible was kept inside the turned-off furnace to cool down to room temperature, after that it weighted again and the weight of the carbon residual was 1.1451g, the weight percentages of the elements inside the carbon residual was analyzed by XRF as shown in Table 4.

Where: $\%M_C$ — Weight percentage of element in the carbon residual; $\%M_0$ —Weight percentage of element in crude oil.

2.4 *Corrosion experiments*

Inorganic salt precipitation is one of the main problems in oilfield operations and many factors can affect scale and fouling formation and their inhibition (Khormali et al. 2018). The availability of abrasive sand particles in the flowing crude oil inside the coiled pipes of the tubular furnaces is considered to be a factor that contribute to the emergence of grooving corrosion (Popov et al. 2019). To prevent the destruction processes and premature failures for reliable operation of oil and coiled-pipes, tanks and oil and/gas pipelines caused by metal corrosion some solutions are needed (Sultanbekov et al. 2019). Using of coiled-pipes made of high-strength composite corrosion resistant materials it must be an intuitive solution (Nikolaev et al. 2017). For an example, using of Ni-resist cast-iron alloys for critical elements of tubular furnaces operating in oil refineries (Bevza et al. 2018) should be a wise decision. Despite the development of corrosion-resistant alloys over the past few decades, cheap and non-resistant alloys are still used in oil, gas and petrochemical industries (Alec 2010 & Nesic 2005) especially in Syria - taking into account the bad economic circumstances as a result of the war consequences – then the only possible way to protect the coiled-pipes of tubular furnace is by adding a corrosion inhibitor, (Achour et al. 2010 & Jevremović et al. 2013).

Corrosion experiments on coiled-pipes coupons were made by using an emulsion (90% laboratory prepared salt electrolyte: 10% Syrian heavy crude oil). The laboratory prepared salt electrolyte (pH = 5.5) having the composition which is shown in Table 5 is used; firstly, without inhibitor, and secondly, with the studied inhibitor (SNPCH-6030 «b») in three

Table 4. Metal content in Syrian heavy crude oil.

Element	$\%M_C*10^4$	$\%M_0*10^4$
S	5.42	1.03
V	94.19	17.90
Ni	41.99	7.98
Fe	30.89	5.87
Zn	19.84	3.77
Mn	14.05	2.67
Cu	4.79	0.91
Pb	3.68	0.70
Co	3.31	0.63
Cr	2.74	0.52
C	balance	balance

Table 5. The composition of the laboratory prepared salt electrolyte.

Chem. compounds	NaCl	$MgCO_3$	$CaCl_2$	$MgSO_4$	HCl
C, M	$8.5(10^{-3})$	$1.6(10^{-6})$	$5.5(10^{-4})$	$5.7(10^{-4})$	$3.2(10^{-6})$

different concentrations 100ppm, 150ppm and 200ppm. The main characteristics of this inhibitor are shown in Table 6.

- Influence of the temperatures on the accelerated corrosion rates (table 7):

From Figure 4, we can notice that at the lowest studied temperature 400°C, the curves are so close to each other because of the relatively close accelerated corrosion rates. By increasing the temperature, the curves move away from each other because of the diverging accelerated corrosion rates. The highest differential corrosion rates are recorded at the highest temperature 700°C.

- Influence of the inhibitor concentrations on the accelerated corrosion rates (Table 8):

Table 6. The main characteristics of the used inhibitor (SNPCH-6030 «b»).

Parameter	Parameter value
Mass fraction of active substance, %	33-37
Mass fraction of phosphorus, %	0.15-0.32
Mass fraction of nitrogen, % not less than	0.13
Pour point, ℃ not higher than	-50

Table 7. The relationship between the temperatures and the accelerated corrosion rates.

T,°C	CR_i,mdd(10^5)-100ppm	CR_i,mdd (10^5)-150ppm	CR_i,mdd (10^5)-200ppm
400	43128.75	32053.02	12985,3
500	89582,74	43073,15	18884,4
600	115533,14	59817,07	16176,03
700	151752,20	103168,4	19373,14

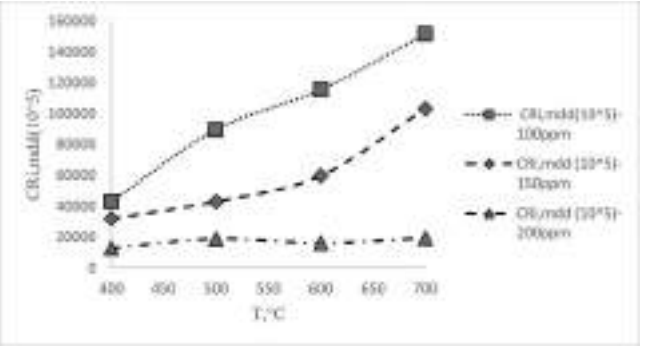

Figure 4. The relationship between the temperatures and the accelerated corrosion rates.

Table 8. The relationship between the inhibitor concentrations and the accelerated corrosion rates.

(i),ppm	CR,mdd (10^5)-400°C	CR,mdd (10^5)-500°C	CR,mdd (10^5)-600°C	CR,mdd (10^5)-700°C
0	71623,31	153158,02	207651,24	301293,01
100	43128,75	89582,74	115533,14	151752,20
150	32053,02	43073,15	59817,07	103168,4
200	12985,3	18884,4	16176,03	19373,14

From the Figure 5, it can be seen that the accelerated corrosion rate decreases with the increasing of the inhibitor concentration. In general, as the temperature increases, the corrosion rate (with/without inhibitor) increases; these increases of the corrosion rates are increased by decreasing inhibitor concentration to reach the maximum corrosion rates without the inhibitor at all studied temperatures, comparing with the accelerated corrosion rates with inhibitor, which indicates that the studied inhibitor (SNPCH-6030 «b») has an effective role in slowing down the corrosion of the coiled-pipes.

In the range of inhibitor concentration (0 - 100ppm), the accelerated corrosion rate is reduced linearly for the four studied temperatures (400°C, 500°C, 600°C and 700°C) with their slopes (-28494.56 (10^{-5}), -63575.28 (10^{-5}), -92118.1 (10^{-5}) and -149540.81 (10^{-5})) respectively. The 700°C-line inside the linear range (0 - 100ppm inhibitor concentration) decreases more rapidly by [-149540.81 (10^{-5})/-28494.56 (10^{-5}) =] 5.2 times, and 600°C-line by [-92118.1 (10^{-5})/-28494.56 (10^{-5}) =] 3.2 times, and 500°C-line by [-63575.28 (10^{-5})/- 28494.56 (10^{-5}) =] 2.2 times by comparison with 400°C-line.

- Influences of inhibitor concentrations on the inhibitor effectiveness in reducing the accelerated corrosion rates (Table 9):

As shown from Table 9, the highest inhibitor effectiveness in reducing the accelerated corrosion rate was recorded for 200ppm inhibitor concentration, at 400°C was 81.87%, while was 87.67% at 500°C, and was 92.21% at 600°C, and was 93.57% at 700°C (which is the highest inhibitor effectiveness ever recorded while the lowest inhibitor effectiveness ever recorded is 39.8% for 100ppm inhibitor at 400°C).

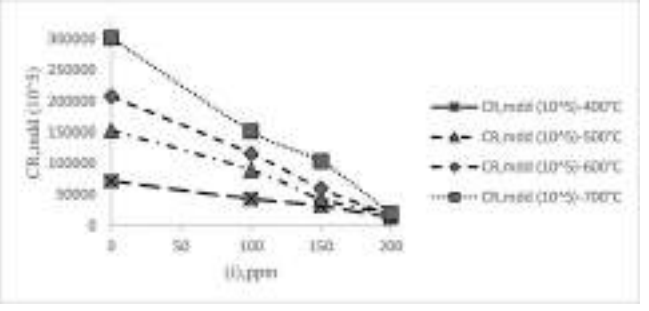

Figure 5. The relationship between the inhibitor concentrations and the accelerated corrosion rates.

Table 9. Impact of temperature on the relationship between inhibitor concentrations and inhibitor effectiveness.

T,°C	$\%_{100ppm}$	$\%_{150ppm}$	$\%_{200ppm}$
400	39.8	55.2	81.87
500	41.5	71.9	87.67
600	44.4	71.2	92.21
700	49.6	65.7	**93.57**

3 RESULTS INTERPRETATION

Taking into consideration that «ELOU» installation — electrical desalting and dewatering installation, NaOH and NH_3 are added in «ELOU» installation before heat exchangers by (2 - 4%) of the amount of crude oil to be refined individually and separately. $NaOH_{(l)}$ is added to the «ELOU» installation (as anti-hydrolysis agent) to control $HCl_{(l)}$ (hydrochloric acid) by converting acidic metal chlorides salts (especially $CaCl_2$ and $MgCl_2$) to NaCl and by converting $HCl_{(l)}$ (hydrochloric acid) - which is generated from the hydrolysis process of the acidic chlorides salts - to NaCl. $NH_{3(g)}$ is added to the «ELOU» installation (as a neutralizer) to control $HCl_{(g)}$ (hydrogen chloride) by converting $HCl_{(g)}$ into $NH_4Cl_{(s)}$. It should be noted that the amount of ammonia should be controlled carefully because: the under-dosing of $NH_{3(g)}$ amount can lead to acid corrosion, while over-dosing of $NH_{3(g)}$ can cause localized underdeposit corrosion, because the excessive formation of $NH_4Cl_{(s)}$ salt, which can cause fouling and later sublimation, and the cycle goes on.

3.1 *Role of chlorides*

The chlorides are always existed in the crude oil (water-in-oil type emulsion), which are considered one of the most dangerous and aggressive components at the studied temperature range, because of the high conductivity of chlorides and therefore of their high tendency to form more stable emulsion, which can lead to presence higher concentrations of chlorides in the dewatered and desalted crude oil after the «ELOU» installation, this possible functional failure or at least low efficiency of the «ELOU» installation definitely can accelerate the corrosion rate of the coiled-pipe leading to the premature failure. Because of that, the corrosion control in the tubular furnaces of «ELOU» installation is very difficult to achieve. The following points can explain the possible roles of chlorides:

- *Role of inverse solubility salts*

It is a well-known fact that by increasing the temperature, the dissolution of all salts, which are existed in the flowing emulsion inside the coiled-pipes, can be increased but their solubility at the studied temperature range is determined only by Le Chatelier's principle. Calcium and magnesium salts can play a role in the deterioration of the coiled-pipe because of their inverse solubility, which can lead to their sedimentation, which in turn can lead to form hard impermeable scale that eventually can lead to overheating and burning-out (thermal failure) of the coiled-pipes of the tubular furnace.

- *Role of acidic salts*

Acidic salts like chlorides (in the first place) and sulfates (in the second place) are harmful due to their hydrolysis processes at the studied temperature range to their derivatives acids, which can lead to increase the local acidity of the medium, which in turn can lead to severe local corrosion in the forms of deep pits, crevices and cracks (Rogachèv & Mukhametshin 2018).

- *Role of volatile metallic chlorides*

The $HCl_{(g)}$ (hydrogen chloride) in the coiled-pipes at the studied temperature range can cause localized corrosion as a result of the formation and sublimation of volatile metallic chlorides, especially iron chloride and copper chloride $FeCl_3$ = 318.4°C, $CuCl_2$= 523.6°C (Maier 1925).

- *Role of molten metallic chlorides*

In spite of molten metallic chlorides are corroding salts and strong ionic electrolytes, which can play an effective role in the electrochemical corrosion but this role is secondary at the studied temperature range (400 - 700°C) due to their higher melting temperatures (melting point of metallic chlorides $MgCl_2$ = 714°C, KCl = 772°C = $CaCl_2$, NaCl = 808°C) (Maier1925).

- *Possible mechanism of the chloride corrosion cycle*

The most common source of $HCl_{(g)}$ vapor/condensate inside the coiled-pipes of tubular furnace comes from hydrolysis process of acidic chloride salts. Eventually all chloride salts in

crude oil will be converted to hydrogen chloride $HCl_{(g)}$ as a result of the high temperature and hydrolysis processes inside the coiled-pipes of the tubular furnace. NaCl is more common in desalted crude oil feeds than $MgCl_2$ and $CaCl_2$ but it is more resistant to hydrolysis. $MgCl_2$ and $CaCl_2$ start to hydrolyze above (121°C) and (204°C) respectively while NaCl is more stable and will not hydrolyze under (232°C) (Bagdasarian et al. 1996, Valenzuela & Dewan 1999 & Kapusta et al. 2001).

Hydrogen chloride $HCl_{(g)}$ can move quickly inside the coiled-pipes, and one part of hydrogen chloride can easily dissolve in water vapor (water condensate), resulting in local mediums with very low pH values it can reach to 1 - 1.5pH (Rogachèv & Mukhametshin 2018), which can lead to dissolve the protecting films/scales or corrosion products to reach the bare metal surface and make deep pits, crevices and even cracks. The second part of hydrogen chloride can react with ammonia vapor $NH_{3(g)}$ to form $NH_4Cl_{(s)}$ ammonium hydrochloride salt (exothermic reaction). If $NH_4Cl_{(s)}$ salt deposits become wet, they can be very corrosive to the alloy of the coiled-pipe and cause localized under-deposit corrosion because of the hydrolysis of NH_4Cl. If NH_4Cl salt deposits do not become wet, under the influence of the high temperatures they can be sublimated to form $NH_{3(g)}$ and $HCl_{(g)}$, which lead to under-deposit corrosion (endothermic reaction). The third part of hydrogen chloride can react easily with active metals and their oxides, hydroxides, and carbonates to produce chlorides with the presence of moisture in the transitional zones or in the scales or corrosion products.

Thus, as a result, the cycle of chloride corrosion will continue endlessly and will lead eventually to total premature failure of the coiled-pipes. Since the concentrations of chlorides in the emulsion will considerably affect the corrosion rate, thus developing the suitable technology to reduce the concentration of chlorides in pre-treatment of the oil before entering the furnace will have great effect on reducing the corrosion rate.

3.2 *Role of metals*

Metals can accelerate corrosion and can also cause catalyst poisoning, fouling and catalyzing undesired side reactions. Impurities like nickel, copper and cobalt in the transitional zones are nobler metals than iron. They can play a negative role through electrochemical corrosion, especially according to their relatively high concentrations in the transitional zones (which needs further research). Vanadium compounds can form vanadium pentoxide V_2O_5, which is conditioned by oxygen availability (most of the spectra of the affected zones proved the oxygen availability of about 5%). Vanadium pentoxide V_2O_5 has relatively low melting point 690°C; this liquid (melted) vanadium pentoxide is strongly corrosive for the coiled-pipes alloy (Bakirova et al. 1984 & Qasim 2017). As shown in the following reaction, where hydrochloric acid $HCl_{(l)}$ is oxidized to the corresponding halogen by V_2O_5, which in turn, is reduced to ionic form of vanadium compound, thus vanadium is also responsible for the deterioration of the coiled-pipe alloy as a result of V_2O_5 forming.

$$V_2O_5 + 6HCl + 7H_2O \rightarrow 2\left[VO(H_2O)_5\right]^{2+} + 4Cl^- + Cl_2$$

Since manganese is existed in the Syrian heavy crude oil up to more than 2.5g/t and in the coiled-pipe alloy up to 2%, maybe it has a possible role in promoting the formation of Cr_2O_3 scale (Sudhangshu 2018) (which needs a further research). Cr_2O_3 scale which has good resistant to hot, acidic and electrochemical corrosion, but its low amount makes its role in corrosion resistance limited. Chrome (which is a corrosive-resistant metal) has high resistant for hot, acidic and electrochemical corrosion. Since coiled-pipe alloy of grade «10X17H13M2T» contains 16 – 18 %Cr and 2 – 3 %Mo as corrosion-resistant alloying elements, this alloy shows better corrosion resistance comparing with other alloys containing low content of chrome, because of the formation and accumulation of thin, chemical stable and passive oxide film of Cr_2O_3. Without chrome as an alloying element, the corrosion rates of the coiled-pipes alloy it would be much worse. However, further corrosion protection is needed for coiled-pipe alloy in the «ELOY» installation against hot, acidic and electrochemical corrosion, due to the high

temperatures and the aggressive medium by applying inhibitor as was suggested in our research (SNPCH-6030 «b») for its considered role in slowing the corrosion rate of the coiled-pipes.

4 CONCLUSIONS

The highest inhibitor effectiveness (SNPCH-6030 «b») in reducing the accelerated corrosion rate was recorded for 200ppm inhibitor concentration, at 400°C was 81.87%, while was 87.67% at 500°C, and was 92.21% at 600°C, and was 93.57% at 700°C (which is the highest inhibitor effectiveness ever recorded while the lowest inhibitor effectiveness ever recorded is 39.8% for 100ppm inhibitor at 400°C). Despite the positive role of chrome as an alloying element in coiled-pipe alloy to protect from corrosion but it is still not enough according to the high temperatures and the aggressiveness of the medium, because of that further corrosion protection (additional protection) is needed for coiled-pipe alloy in the «ELOY» installation against hot, acidic and electrochemical corrosion by applying the studied inhibitor (SNPCH-6030 «b») as we suggested in our research for its significant role in slowing the corrosion rate of the coiled-pipes. The high contents of vanadium and chloride in Syrian heavy crude oil, in addition to the high content of nickel, copper and cobalt in the transitional zones and of course the high temperature inside the coiled-pipe of the tubular furnaces are the main reasons for the severe corrosion of the coiled-pipe which led to the premature failure. Mixed mechanism between sedimentation — sublimation and redox reactions was proposed to interpret the hot corrosion of the coiled-pipe. Mixed mechanism between dissolution — sedimentation reactions and hydrolysis reactions was proposed to interpret the acid corrosion of the coiled-pipe. Mechanism of electrochemical reactions (galvanic effect) was proposed to interpret the electrochemical corrosion of the coiled-pipe in the transitional zone with the presence of nobler metals than iron, mainly in the water vapor/condensate inside the coiled-pipe and less possibly in molten salts (due to their higher melting points than the studied temperature range).

REFERENCES

Achour, M., Blumer, D., Baugh, T., Lane, C., Humble, Ph., Waters, J.,Wilcher, J.& Hudgins, R. 2010. A novel method to mitigate top of the line corrosion in wet gas pipelines: part I – proof of concept, CORROSION, paper no. 11332.

Alec, Groysman. 2010. Corrosion for Everybody. Springer-Verlag, Dordrecht. p 346–159.

Alekseev, M.V. 1972. Basics of fire prevention in technological processes of production. M., Higher School of the Ministry of Internal Affairs of the USSR, NIIRIO. p 89–132, 143-159.

Alekseev, M.V.& Smirnov, V.M. 1955. Fire prevention in the technological processes connected with the circulation of flammable and flammable liquids. M.: Ministry of Communal Services of the RSFSR. p 17–49.

Bagdasarian, A., Feather, J., Hull B., Stephenson R. & Strong, R. 1996. Crude Unit Corrosion and Corrosion Control. Corrosion/96, Paper No. 96615, NACE International, Houston, TX.

Bakesheva, A.T., Fetisov, V.G. & Pshenin, V.V. 2019. A refined algorithm for leak location in gas pipelines with determination of quantitative parameters. International Journal of Engineering Research and Technology. Volume 12, Issue 12, Pages 2867–2869.

Bakirova, S.F.,Kotova, A.V.,Yagyayeva, S.,Fedorova, N. & Nadirov, N.K.1984. Structural Features of Vanadyl Porphyrins of Petroleum of West Kazakhstan, Petroleum Chemistry U.S.S.R., 24, 196–202.

Baratov, A.N., Korolchenko, A.Ya. & Kravchuk, G.N. 1990. Fire and explosion hazard of substances and materials and means of extinguishing them; M., Chemistry. p 25–39.

Bevza, V.F., Grusha, V.P. & Krasnyy, V.A. 2018. Improvement of structure and properties of ni-resist cast-iron part blanks for mining and petroleum refining machine industry. Mining Informational and Analytical Bulletin. Vol. 2018, Issue 2, Pages156–167.

Bobritsky, N.V. & Yufin, V.A. 1988. Basics of the oil and gas industry. M.: Nedra. p 174–189.

Goldobina, L. A. & Orlov, P. S. 2019. Analysis of the corrosion destruction causes in underground pipelines and new solutions for increasing corrosion steel's resistance. ZapiskiGornogoinstituta. Volume 219.
Isaev, N.I. 1997. Theory of corrosion processes. M.: Metallurgy. p 289–321.
Ivanik, S.A. & Lyubin V, E.A. 2017. Chemical and electrochemical methods of protection from corrosion of gas and oil pipelines pipelinesand storage tanks. International Multidisciplinary Scientific GeoConference Surveying Geology and Mining Ecology Management, SGEM. Vol. 17, Issue 14, Pages579–584.
Jevremović I., Singer M., Achour M., Blumer D., Baugh T., Misković-Stanković V. & Nešić S. 2013. A Novel Method to Mitigate the Top-of-the-Line Corrosion in Wet Gas Pipelines by Corrosion Inhibitor within a Foam Matrix. Corrosion. p 144–167.
Kapusta, S., Ooms, A., Buijis, J.W., Fan, D. & Fort, W. 2001. Systematic Approach to Controlling Fouling and Corrosion in Crude Unit Overheads and Hydrotreater Reactor Effluents. Corrosion/01, Paper No. 01535, NACE International, Houston, TX,
Khormali, A., Sharifov, A.R. & Torba, D.I. 2018. Increasing efficiency of calcium sulfate scale prevention using a new mixture of phosphonate scale inhibitors during waterflooding. Journal of Petroleum Science and Engineering. Vol. 164, Pages 245–258.
Kondrasheva, N. K., Dubovikov, O. A., Ivanov, I. I. & Zyr'yanova, O. V. 2014. Preliminary preparation of oil for primary processing. ZapiskiGornogoinstituta. Volume 210.
Maier, C. G. 1925. Vapor pressures of the common metallic chlorides and a static method for high temperatures. University of Utah. Department of Metallurgical Research, Washington, D.C.: U.S. Dept. of the Interior, Bureau of Mines: U.S. Govt. Print. Off. P.53
Nesic, S. 2005. Key Issues related to modeling of internal corrosion of oil and gas pipelines – A review, 16th International corrosion congress.
Nikolaev, A.K. & Velazquez, A.L.C. 2017. Modelling of fiberglass pipe destruction process. Journal of Mining Institute. Vol. 223, Pages 93–98.
Popov, G., Kasyanov, A., Bolobov, V. & Krivokrysenko, E. 2019. Study of factors enabling initiation and behavior of grooving corrosion. E3S Web of Conferences. Vol. 121.
Qasim, Y Mohammed. 2017. Determination of salt content in crude oil, turbine oil and some refinery products volumetrically, Journal of Chemical and Pharmaceutical Sciences, volume 10 (issue 1).
Rogachèv, M.K. & Mukhametshin, V. V. 2018. Control and regulation of the process of hydrochloric acid effect on the well bottom zone according to geological field data. ZapiskiGornogoinstituta. T. 231. p.275–280.
Saakyan, L.S. & Efremov, A.P. 1982. Protection of oilfield equipment against corrosion. M.: Nedra. p 186–211.
Sudhangshu, Bose. 2018. High Temperature Coatings (second edition). Butterworth-Heinemann. P. 416
Sultanbekov, R. & Nazarova, M. 2019. The influence of total sediment of petroleum products on the corrosiveness of the metal of the tanks during storage. E3S Web of Conferences. Vol. 121.
Tsenev, A.N., Nosov, V.V.& Akimova, E.V. 2017. Fault location method for unexposed gas trunk line insulation at stray current constant effect area. IOP Conference Series: Earth and Environmental Science. Vol. 87, Issue 9.
Valenzuela, D. & Dewan A. 1999. Refinery Crude Column Overhead Corrosion Control, Amine Neutralizer Electrolyte Thermodynamics, Thermochemical Properties, and Fluid Phase Equilibria., p 829–834.
Volovikov, A. Yu. 2010. Problems and prospects of the exploration of the primary oil refining. ZapiskiGornogoinstituta. Volume 186.

Advances in Raw Material Industries for Sustainable Development Goals – Litvinenko (Ed)

Technogenic byproduct filler-based earthquake-resistant super concrete

M.S. Saidumov & A.Kh. Alashkhanov
FSFEI HE "Millionschikov Grozny State Oil Technical University", Grozny, Russia

S-A.Yu. Murtazaev
FSFEI HE "Millionschikov Grozny State Oil Technical University", Kh. Ibragimov Complex Institute of the Russian Academy of Sciences, Grozny, Russia

T.S-A. Murtazaeva
Academy of Sciences of the Chechen Republic, Grozny, Russia

ABSTRACT: The article presents an analysis of domestic and foreign experience in the production and use of high-strength concrete (HSC) and studies raw material resource base, both natural and secondary, for their production. The test results of filled binders obtained with the use of concrete scrap and brick rubble processing are given. The compositions of earthquake-resistant HSC, classified to be up to B80 in compressive strength, are obtained and the results of their tests are presented.

This work was carried out as part of research on the implementation of scientific project No. 18-48-200001 "High-quality concrete with enhanced performance properties based on local natural and secondary (processed) raw materials," which received support from the Russian Foundation for Fundamental Research (RFFR).

Keywords: High-strength concrete, super concrete, local raw materials, products of buildings and constructions demolition and dismantling, concrete scrap, brick rubble, recycling, secondary or recycled filler (sand), filled binder, concrete

1 INTRODUCTION

Currently, for the construction of cast-in-situ buildings and constructions, along with traditional concrete of grade B7.5-B30, new effective concrete composites are becoming widely used: high-strength, non-shrinking, expanding, straining and others, that are also made with the use of new composite or filled binders, which significantly expand the range and capacity of product units (Kaprielov et al., 2017, Bazhenov, 1995, Bazhenov et al., 2011). Specifically, according to the American Association of Cement Manufacturers, in 2012 alone, the world's leading industrial powers produced more than 13 billion cubic meters of concrete (Volkov, 2004).

It is a common knowledge that high-rise construction lead to increased demands placed on the quality of raw materials, the uniformity and stability of the compositions, the reliability and stability of the construction, etc. For concretes operating in seismically active regions, the issue of selecting the composition and designing the properties of the future composite requires even more attention. Such concretes must possess increased strength, ductility and enviable longevity (Bataev et al., 2017, Kuprina, 2014).

An analysis of scientific papers (Lesovik et al., 2012, Volodchenko et al., 2016) on high-strength concrete technology shows that their production is usually associated with the use of high-quality natural raw materials affecting the cost and increasing the energy and resource consumption of composites based on them.

With a rational approach of using such elements as modern chemical modifiers of the concrete structure, mineral additives of various nature, as well as effective equipment for activating raw materials and homogenizing the mixture, high-strength concrete compositions based on secondary raw materials can be recommended.

First of all, concrete and reinforced concrete scrap, as well as crushed brick (rubble), which make up more than 60% of the total waste of dismantling buildings and structures, are of great interest for concrete technology (Murtazaev et al., 2009, Salamanova & Murtazaev, 2018). According to the authors, this interest is caused by the possibility of their use as a finely ground mineral component in mixed or so-called filled binders, characterized by improved technological and physico-mechanical properties, based on which, high-strength concrete can be obtained suitable for cast-in-situ high-rise construction in seismically active regions of the country and the world.

2 LITERATURE REVIEW

In foreign practice, high-strength concrete (or considered to be high-strength at that time) began to appear at the beginning of the second half of the twentieth century, when concrete of classes B30 and higher began to be developed in the USA, Norway and some other countries. Later, in the 70s and 80s, analogues of modern high-strength concrete of B70-B80 compressive strength classes were known (Bazhenov et al., 2006).

Scientific works of Kim J.-K., Aitcin P.C., Skazlic M., Shi C., Talebinejad I., Strunge T., Wille K., Soutsos M., Ma J. are internationally recognised for their contribution to the development of HSC practice. Works of these researchers and of a number of other scientists, highlight the features of the technology for producing high-strength concrete and the role of mineral additives in the process of their structure formation.

According to Kim J.-K. (Kim & Kim, 1996) and Aitcin P.C. (Aitcin, 1998) it was proved that the presence of finely dispersed fillers and additives helps to reduce the amount of portlandite and ettringite and fill capillary pores with hydration products, as a result of which a decrease in porosity and the obtainment of high concrete strength are observed.

The raw materials requirements to obtain HSC presented in the works of Aitcin P.C. (Aitcin, 1998), Skazlic M. (Skazlic & Bjegovic, 2005) and Shi C. (Shi et al., 2015), are mainly associated with a limitation of the amount of water (W/C = 0.22-0.4), high cement content (about 450-560 kg/m3), optimization of the grain composition of aggregates (sand size modulus Mk = 2.5-3, the recommended crushed stone fraction is 10-15 mm, the absence of flaky grains, etc.), the use of mineral fillers (finely ground additives of various nature, which reduce the porosity of cement stone), etc.

The fragility and the pattern of deterioration of high-strength concrete was investigated in the works of Richard P. and Cheyrezy M. (Richard & Cheyrezy, 1995), where it is recommended to use fiber reinforcement in order to increase the fracture toughness of concrete. In addition, in order to obtain concrete with a strength of about 150 MPa, Cheyrezy M., Shi C. and other scientists outside of Russia suggest reducing the W/C ratio to 0.13 and argue that in this case the maximum density of the concrete composite can be achieved.

Yu.M. Bazhenov (Bazhenov, 1995), S.S. Kaprielov (Kaprielov et al., 2017), D.K.-S. Bataev (Bataev et al., 2017), V.S. Lesovik (Lesovik et al., 2012), B.C. Demyanova (Demyanova & Gusev, 2013), V.I. Kalashnikov (Bazhenov et al., 2006), G.V. Nesvetaev (Nesvetaev et al., 2003), O.Ya. Berg (Berg et al., 2012) and others have actively contributed to the development of Russian science in the field of obtaining HSC.

Until recent times, the low demand for high-strength concrete in Russia has led to the fact that the concrete used in Russia at the end of the twentieth century secured much lower index in strength (almost 2 times) in comparison with concrete developed in the USA and Europe. The production and development of high-strength concrete in Russia is mainly associated with the development of binders of low water demand (LWD) and their modified analogues developed by Russian scientists Yu.M. Bazhenov and his students (Bazhenov et al., 2011), due to the fact that the potential for using binding ability and properties in such binders is 1.5-2.0

times greater in comparison with traditional factory grinding cements. Currently, due to the development of a market economy and the development of domestic scientists in Russia, there is practically no gap in the physical, mechanical and other indicators of modern concrete used in Russia and abroad.

Kaprielov S.S., Sheinfeld A.V. and Dondukov V.G. (Kaprielov et al., 2017) studied binders for high-strength concrete and proposed optimal compositions of effective high-strength concrete for cast-in-situ construction based on the use of the MB series concrete modifier.

Works of Lesovik V.S. and his students (Lesovik et al., 2012, Volodchenko et al., 2016) develop methodological foundations for the use of energy-saving raw materials and effective technologies for the production of building composite materials, considering the genesis of the raw materials and the sustainability of the "man - material - environment" system. V.S. Lesovik is the author of a new transdisciplinary scientific field - geonics, and his scientific school solve engineering problems considering the knowledge gained during the study of natural processes and view rocks as natural analogues of building materials. Therefore, they obtained ultra-high-strength concrete using the theoretical principles of geonics and raw materials of the Kursk magnetic anomaly, which, according to the author, will be in demand in the development of the North and the Arctic, in the construction of fortifications and in the field of other anomalous conditions for the operation of materials."

Thus, the experience of researchers, both Russian and international, shows that HSC currently is and in the foreseeable future will be in great demand in the manufacture of a wide range of structural elements of civil buildings and special structures, both in earthquake-safe areas and in areas with sites for increased seismic activity (Kim & Kim, 1996, Aitcin, 1998).

Therefore, the development of compositions of high-strength concrete based on the integrated use of secondary raw materials for their (compositions') use in concreting structural elements of high-rise cast-in-situ earthquake-resistant buildings is an urgent problem in the field of concrete technology that needs to be addressed in order to increase the efficiency of the waste recycling process resulting from dismantling buildings and structures.

3 RESEARCH METHODS AND MATERIALS

They are constituted by mineral fillers of technogenic nature (MFTN) for producing high-quality concrete mixtures using mechanical activation and ceramic brick rubble (CBR) in a laboratory vibrating ball mill of the MV-20-EKS type to obtain a specific gravity of 450-600 m^2/kg. The average grinding time was 4-6 minutes.

The chemical composition of the feedstock, as well as the macro- and microstructure of concrete samples, were studied using a Quanta 3D 200i scanning electron microscope.

The natural sand of the Chervlenskoye deposit in the Chechen Republic with the following characteristics was used as a fine aggregate: fineness modulus Fm = 1.7-1.8; the content of flour and clay particles is 1.7-1.9%; void coefficient – 40.8 %; density $\rho_{s.}$ = 2617 kg/m^3; density $\rho_{p.}$ = 1512 kg/m^3.

Local gravel from gravel fractions of 5-20 mm fractions of the Argun and Sernovodsky deposits of the Chechen Republic was used as a coarse aggregate.

In experimental studies, a plain Portland cement of the PC 500 D0 grade produced by the State Unitary Enterprise "Chechencement" (Chechen Republic, village of Chiri-Yurt) with normal consistency (NC) = 25.5%, specific surface area of 3252 cm^2/g, water segregation (bleeding) ≤ 18% and the setting time of 2 hours and 15 minutes (start) and 3 hours 40 minutes (end) was used as a binder. The content of clinker minerals characterizing the mineralogical composition of the binder: C_3S = 59 %; C_2S = 16 %; C_3A = 8 %; C_4AF = 13 %.

Modern additives of the following manufacturers of construction chemicals were used as fluidizing agents:

1. POLYPLAST company - "Linamix PK" (liquid) superplasticizing agent (SP) and "Linamix RS" (liquid) hardening retardant based on polyoxyethylene derivatives of polymethacrylic acid;

2. TOKAR LLC (Vladikavkaz) offers a complex multifunctional additive "D-5" (in a dry powder form) that meets the requirements of State All-Union Standard (SAUS) No. 24211-2008.

The choice between the proposed additives is due to their accessibility and cheapness, although their analogues with equal effectiveness are known in the world for instance plasticizer additives from manufacturers such as "MC-Bauchemie" ("MC-PowerFlow" hyperplasticizer based on the latest polycarboxylate ester technology MS), "Sika" company ("Sika ViscoCrete 5-600 SK" superplasticizer based on polycarboxylate esters), etc.

4 RESULTS

In order to obtain optimal formulations of high-strength concrete with the integrated use of the secondary raw material, compositions of filled binders (FB) with a fine-ground mineral filler of technogenic nature (MFTN – filler made of recyclables) were developed, allowing to obtain a high-strength cement stone with significantly smaller pores and less shrinkage (Table 1).

Two brands of FB with a finely ground MFTN (developed by the authors) were studied, the formulations of which are included, % by weight:

– The brand of FB:	FB-75:25	FB-60:40
– PC M500 D0 «Chechencement»	75	60
– MFTN of concrete scrap	16	27
– Same, of CBR	7	11
– D-5 Additive	2	2

The compositions were developed in relation to the technology for constructing cast-in-situ bored piles of the 435-meter multi-functional high-rise complex "Akhmat Tower", erected in the city of Grozny on a site with a seismicity of 9-10 points.

Due to the fact that concrete of various strength grades (B40, B75-B80, etc.) were laid down for the design of the underground part the complex, the task of designing optimal formulations of high-strength concrete was indicated in this work, including medium-grade concrete of compressive strength B30-B40 and high-strength - B50-B80 all of which were produced with the integrated use of secondary raw materials. At the same time, the formulations were designed to obtain highly mobile (pumpable castables) concrete mixtures with a standard cone slump of 22 ± 2 cm, which corresponds to the P5 workability grade, which are used in modern cast-in-situ construction field, as more efficient concrete mixtures requiring less energy for pumping through a concrete pump pipeline and subsequent vibrocompaction.

The compositions and properties of high-quality concrete mixtures with increased durability and longevity are presented in Table 2.

Table 1. Properties of FB with fine-ground (floured) MFTN.

Name of a binder	Normal density ND,%	S_{ssa} of a - binder, m^2/kg	True density, kg/m^3	Water segregation (bleeding), %	Setting time, hour. - min		Activity, MPa
					Start	End	
FB-75:25	17	558	2986	15,5	3-40	5-30	71,3
FB-60:40	19	577	2905	14,7	3-55	5-35	60,7
PC M500 D0 SUE «Chechencement» *(for reference)*	26	325	3115	18,0	2-15	3-40	52,6

Table 2. Compositions and properties of concrete mixtures based on secondary raw materials.

Composition/ mix No.	Design grade of concrete	Required strength, MPa	Consumption of concrete mixture components, kg/m^3								Mixture characteristics			
			Crushed stone		Sand	Binder			Additive					
			Argun	Sernovodskoe	Chervlennoe	FB-60:40	FB-75:25	Water	Linamix PC (% of cement's mass)	Linamix RS (% of cement's mass)	Water-to-cement ratio	Density, kg/m3	CS, cm	Longevity, jour
1	B30	39,3	1000	-	855	385	-	161	1,1 (0,3)	2,5 (0,7)	0,45	2398	23	7,0
2	B40	52,4	1000	-	795	435	-	158	1,3 (0,3)	3,0 (0,7)	0,36	2407	21	7,0
3	B45	58,9	1000	-	765	470	-	162	1,4 (0,3)	3,3 (0,7)	0,34	2427	23	8,0
4	B55	72,0	-	1000*	735	-	540	161	1,6 (0,3)	3,8 (0,7)	0,31	2451	23	8,5
5	B60	78,6	-	1000*	685	-	600	165	1,8 (0,3)	4,3 (0,7)	0,30	2462	21	9,0
6	B80	104,7	-	1000*	620	-	700	170	2,1 (0,3)	4,9 (0,7)	0,32	2481	24	10,0

Note: * - enriched crushed stone from gravel of a fraction of 5-20 mm with M1200 grade for crushability

The Linamix PK superplasticizer was introduced into FB concrete mixes together with mixing water in a small amount (from 0.3 to 0.4% of the binder's weight), since the complex polyfunctional additive D-5 already has plasticizing properties in the composition of FB.

The hardening retarder "Linamix RS" was dosed in an amount of 0.7% by weight of the binder in order to ensure increased workability retaining capacity of concrete mixtures (7-8 hours or more).

The obtained experimental data on the study of the properties of HSC based on secondary raw materials of technogenic nature are presented in Table 3.

When comparing the obtained experimental results of testing concrete based on filled binders (Table 3) with known indicators of concrete strength on traditional Portland cement, you can notice the difference in the dynamics of the concrete strength gain (Figure 1).

In order to analyze the degree of homogeneity of the studied concretes based on secondary raw materials, the dependences of the prismatic strength coefficient of concretes on their compositions and on the type of binders used were studied. In addition, the proportion of the clinker part and the finely ground filler of technogenic nature in the used binders varied.

The obtained data reflecting the experimental dependencies of the prism strength R_{PR} of the developed concrete using binders of various nature on their cubic strength R, were compared with the known data of Russian scientists (Figure 2).

It was established that with an increase of the prismatic strength of concrete, its modulus of elasticity increases as well (Figure 3). Moreover, the dependence curve is slightly different from the known data obtained by prof. G.V. Nesvetaev and his students.

5 DISCUSSION

Based on the analysis of the results obtained, it can be stated that concretes containing filled binders that use finely ground fillers of technogenic nature are characterized by distinctive features of properties compared to traditional Portland cement concretes. In particular, this relates to retaining workability parameters of the concrete mixtures, the dynamics of curing during the first days of hardening, the strain (deformation) properties of concrete, etc. (Figures 1-3).

Therefore, the development process of FB concrete's strength characteristics at 1-3 days of age is accelerated by 1.5-2 times: on the first day FB concrete develops a strength about 33-36% higher compared to the design strength, and on the 3-day, the strength is 65- 75%. Moreover, at the age of 7 days, the strength of this concrete completely exceeds 85-90% of the design strength. This differs significantly from the performance of conventional formulations that use traditional Portland cement. Thereby, these characteristics when relating to the traditional concrete at the age of 1, 3 and 7 days correspond to 23-26, 34-37 and 65-70% of the design strength, respectively. Such dynamics of concrete hardening is explained by the complex effect of chemical modifiers that form the concrete as well as filled binder. Additive D-5 in concrete, which exhibits plasticizing properties during the first hours after mixing the concrete with water, begins to act as an accelerator since day one, to a certain extent. A similar effect of D-5 on the properties of concrete mix and concrete itself turn it into a multifunctional additive that positively affects both the rheological and technological characteristics of the mixture, as well as the physical-mechanical and operational characteristics of the concrete. Identically, the properties of the concrete mixes and concrete are also affected by the addition of Linamix PK, which accelerates the hardening of concrete at an early age. Such a sufficiently fast dynamics of the strength development allows you to load constructional elements at an early age (1. . .7 days after construction).

As is commonly known, among the most important indicators of the quality of concrete mix for cast-in-situ construction is the ability of the concrete to retain the parameters of its workability (mobility, composition stability, etc.) for a long time. In this regard, the rheological and technological properties of concrete mixtures were studied, in particular their mobility, durability, ability to retain workability, water segregation (bleeding), segregation of concrete, etc. As can be seen from Table 3, the compositions studied and proposed in this work (special concrete compositions) based on filled binders and special additives are characterized by increased capacity to retain

Table 3. Properties of HSC based on raw materials of various nature.

Mix No. from Table 2	Design grade of concrete	ρ_c, kg/m^3	Compression strength at the age of . . ., MPa								Strain ε, mm/m						
			R				R_{PR}										
			1 day	3 days	7 days	28 days	28 days	R_{PR}/R	R_{tb}	$E_C \cdot 10^3$, MPa	longitudinal ε_1	lateral ε_2	Poisson's ratio μ	Concrete shrinkage, mm/m	W_M, % by weight	W	F
1	B30	2336	14,3	31,7	41,1	46,7	38,3	0,82	4,8	43,5	2,08	0,49	0,237	0,62	2,7	W14	F400
2	B40	2352	17,8	38,9	51,7	58,1	47,6	0,82	5,7	44,8	1,99	0,47	0,235	0,60	2,7	W14	F400
3	B45	2358	22,3	45,5	59,9	65,8	54,6	0,83	6,4	46,2	1,96	0,46	0,234	0,55	2,5	W16	F500
4	B55	2365	26,4	54,1	69,6	77,3	65,7	0,85	8,2	47,5	1,96	0,45	0,228	0,40	2,4	W18	F500
5	B60	2383	29,5	59,8	75,3	85,4	72,6	0,85	8,6	52,4	1,95	0,43	0,222	0,36	2,4	W20	F600
6	B80	2408	40,9	81,8	106,1	115,3	99,2	0,86	9,7	54,5	1,90	0,40	0,210	0,31	2,2	W20	F600

Note: ρ_c – concrete density, kg/m^3; R – cubic compressive strength of concrete, MPa; R_{PR} – prismatic concrete compressive strength, MPa; R_{PR}/R – othe ratio of the prismatic strength of concrete to cubic, characterizing its uniformity; R_{tb} – concrete tensile strength in bending, MPa; $EC \cdot 10^3$ – concrete modulus of elasticity, MPa; ε – concrete strain, mm/m; ε_1 – longitudinal strain of concrete, mm/m; ε_2 – lateral strain of concrete, mm/m; μ – Poisson's ratio (lateral strain coefficient); W_M – concrete water absorption by weight, %; W – concrete's grade by its waterproof capacity; F – concrete's grade for frost resistance.

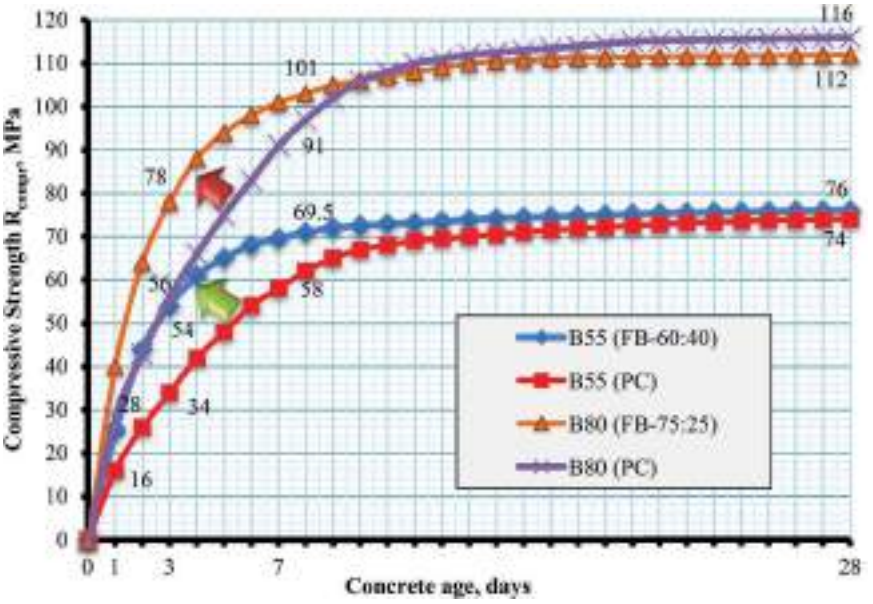

Figure 1. Assessment of the concrete strength characteristics growth (over time), depending on the type of binder.

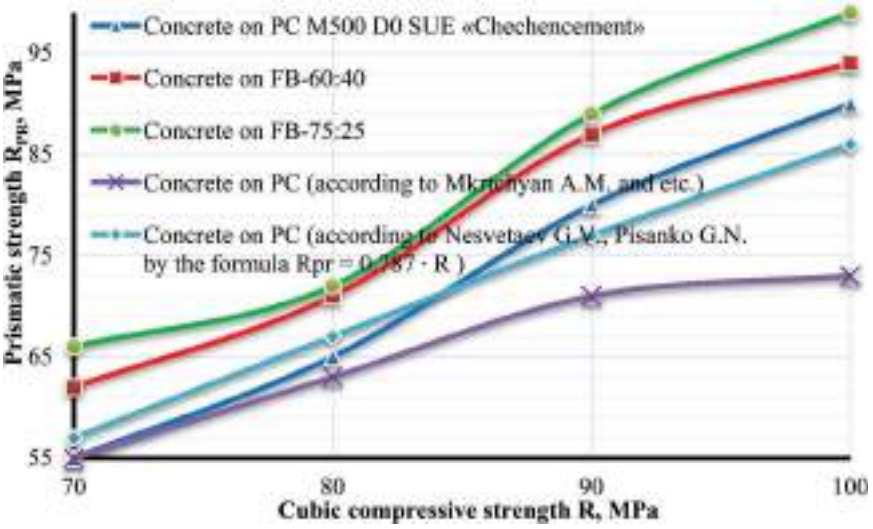

Figure 2. Dependence of the prism strength R_{PR} on cubic R when using binders of various nature.

workability (8-10 hours). High rates of workability parameters preservation of concrete mixtures contribute to the production of an integral in-situ construction without the formation of "cold joints" in case of unforeseen circumstances associated with breakdown of equipment and tools, failure to supply the mixture, etc. And after the end of the inhibitory effect of the additive, these mixtures quickly gain strength at an early age (1-3 days), which increases the efficiency of form reuses and, as a result, drastically reduces the construction time, which is very important in modern cast-in-situ construction. For elements of the precast reinforced construction industry,

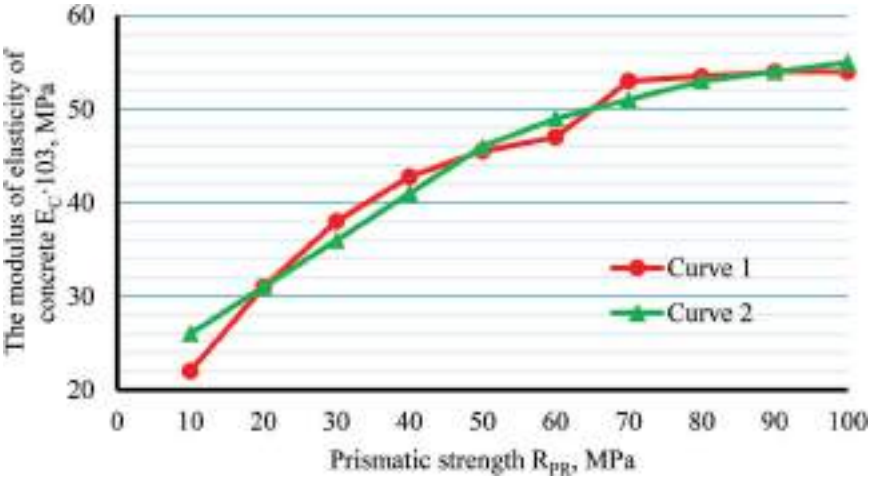

Figure 3. Dependence of the elastic modulus of HSC produced with a finely ground MFTN (curve 1) and ordinary concrete (curve 2, according to G.V. Nesvetaev) on its prism strength.

such a feature of the proposed concrete formulations (high durability, rapid strength development, etc.) will slash the manufacturing time of constructions, and in some cases, partially or completely eliminate the cost of concrete steaming.

6 CONCLUSIONS

Formulations of filled binders (FB) with an activity of 60-71 MPa with finely dispersed mineral fillers of technogenic origin (MFTO), including concrete scrap and ceramic brick (CBK) with a ratio of 70:30%, respectively, were developed and studied, with the proportion of the filler mixture in FB amounted to 25 and 40% by weight of the binder.

Using secondary raw materials, optimal formulations of concrete mixtures with a grade of P5 in cone slump along with its capacity to retain workability for more than 8 hours were designed to produce HSC.

The physical-mechanical characteristics of HSC made of secondary raw materials of B60-B80 grades were studied, and the development of their strength characteristics over a period of time depending on the type of binder was evaluated. It was found that the process of strength development of FB concrete is accelerated by 1.5-2 times at an early age (1-3 days). So, FB concrete at the age of 1 day has a strength of about 33-36% of the design, and at the age of 3 days - it reaches up to 70%. The 7-day strength of concrete obtained using FB is about 85-90% of the design, which is significantly higher than the performance of traditional "PortlandCement" (PC) compositions.

It is proved that the prismatic strength coefficient (i.e., the RPR/R ratio) for FB concrete is in the range of 0.82-0.86, whereas the traditional PC concrete shows only 0.78 or lower.

The stress-related (deformational) properties of HSC based on secondary raw materials were studied. It was found that the concrete modulus of elasticity of the proposed compositions of HSC, prepared on the basis of secondary raw materials, is in the range of $40{,}2 \times 10^3$ – $54{,}5 \times 10^3$ MPa, depending on the strength of concrete and the type of filler. Moreover, the higher the strength of concrete, the higher its modulus of elasticity.

It is experimentally proved that the ultimate longitudinal ε_1 and lateral ε_2 strains of the HSC on finely dispersed MFTN are 1.93-2.32 mm/m and 0.41-0.66 mm/m, respectively. For straight cement concrete of traditional composition, they usually reach ε_1 = 3.2-3.6 mm/m and ε_2 = 1.9-2.0 mm/m. It is discovered that with an increasing concrete strength and higher proportion of finely ground MFTN the longitudinal and lateral strains decrease.

It was found that the Poisson's ratio μ (lateral strain coefficient) for HSC with a finely ground MFTN is in the range of 0.21-0.285. It was found that with an increase in concrete strength, the Poisson's ratio of HSC decreases, which indicates a more fragile nature of the structure of such concrete with an increase in their compressive strength grade.

Thus, the given deformation characteristics of the developed HSC testify to their high resistance to dynamic influences, including seismic ones.

It has been proved that HSC based on FB with fine-ground MFTN are characterized by high grades in frost resistance (F300-F500) and waterproof (W14 and higher), demonstrating a solid evidence of high durability and longevity of such concrete.

REFERENCES

Aitcin, P.C. 1998. High-performance concrete. London: E&FN SPON.

Bazhenov, Yu.M. 2011. Fine-grained concrete from recycled materials for the repair and restoration of damaged buildings and structures: scientific publication / Yu.M. Bazhenov, D.K.-S. Bataev, St. A.Yu. Murtazaev, H.N. Mazhiev. - Grozny: IE "Sultanbegova H.S.".

Bazhenov, Yu.M. 1995. Concrete of the 21st Century/Yu.M. Bazhenov // Resource- and energy-saving technologies of building materials, products and structures: Sat. scientific tr Int. conf. -Belgorod.

Bazhenov, Yu.M. 2006. Modified high-quality concrete: scientific publication / Yu.M. Bazhenov, B.C. Demyanova, V.I. Kalashnikov. - M.: Publishing house of the Association of construction universities.

Bataev, D.K.-S. 2017. Recipes of high-strength concrete based on technogenic and natural raw materials / D.K-S. Bataev, M.S. Saydumov, T.S.-A. Murtazaeva, D.M. Dudaev, M.K. Salgiriev // Actual problems of modern building science and education: materials of the All-Russian scientific-practical conference dedicated to the 60th anniversary of the building faculty of FSBEI HE "GSTU named after Acad. M.D. Millionschikova", October 12–13, 2017 - Grozny: P. Bisultanova.

Berg, O.Ya. 2012. High-strength concrete/O.Ya. Berg, E.N. Shcherbakov, G.N. Pysanko. –M.: Stroyizdat.

Demyanova, V.S. 2013. Effective building materials using industrial waste/V.S. Demyanova, A.D. Gusev. –Penza: PGUAS.

Kaprielov, S. S., Scheinfeld, A. V., Dondukov, V. G. 2017. Cements and additives for the production of high-strength concrete // Building materials. - No. 11.

Kim, J.-K., Kim, Y.-Y. 1996. Experimental study of the fatigue behavior of high strength concrete // Cement and Concrete Research. -Vol. 26, -Issue 10.

Kuprina, A.A., Lesovik, V.S., Zagorodnyk, L.H., Elistratkin, M.Y. 2014. Anisotropy of materials properties of natural and man-triggered origin // Research Journal of Applied Sciences. –Vol. 9.- Issue 11.

Lesovik, B.C. 2012. Building composites based on screenings for crushing concrete scrap and rocks: scientific publication/B.C. Lesovik, St. A.Yu. Murtazaev, M.S. Saydumov. –Grozny: Municipal Unitary Enterprise "Printing House".

Murtazaev, S-A.Yu. 2009. Fine-grained concrete based on fillers from recycled materials [Text]: scientific publication / S-A.YU. Murtazaev, D.K.-S. Bataev, Z.K. Ismailov, Kh.N. Mazhiev, St. M.K. Khubaev. -M.: Komtekhprint.

Nesvetaev, G.V. 2003. Evaluation of the effectiveness of superplasticizers for high-strength and high-quality concrete / G.V. Nesvetaev, A.V. Nalimova, G.V. Bumblebee // Proceedings of universities. Construction, -№ 9.

Richard, P., Cheyrezy, M. 1995. Composition of reactive powder concretes // Cement and Concrete Research. -No. 25.

Salamanova, M.Sh. 2018. Clinker-free binders based on finely dispersed mineral components/Murtazaev S.A. Yu., Salamanova M.Sh. // Collected: ibausil conference proceedings. - -FROM. 707–714.

Shi, C., Wu, Z., Xiao, J., Wang, D., Huang, Z., Fang, Z. 2015. A review on ultra high performance concrete: Part 1. Raw materials and mixture design // Construction and Building Materials. -No. 101.

Skazlic, M., Bjegovic, D. 2005. Perspectives of designing with new concrete types. Zagreb: Annual 2005 of the Croatian Academy of Engineering.

Volkov, Yu. 2004. Concrete basis for modern skyscrapers / Yu. Volkov, A. Zvezdov // Construction. - -No. 5.

Volodchenko, A.A., Lesovik, V.S., Zagorodnjuk, L.H., Volodchenko, A.N., Aleksandrovna, K.A. 2016. The control of building composite structure formation through the use of multifunctional modifiers // Research Journal of Applied Sciences -№ 10 (12).

Advances in Raw Material Industries for Sustainable Development Goals – Litvinenko (Ed)

Recent technologies in selective removal of arsenic in copper ore processing

A. Kobylyanski
Postgraduate student, Saint-Petersburg Mining University, Saint-Petersburg, Russian Federation

V. Zhukova
Master student, Saint-Petersburg Mining University, Saint-Petersburg, Russian Federation

V. Grigoreva
Student, Saint-Petersburg Mining University, Saint-Petersburg, Russian Federation

A.Ya. Boduen
PhD, Associate professor, Saint-Petersburg Mining University, Saint-Petersburg, Russian Federation

ABSTRACT: The changes of raw material's characteristic and challenges of processing copper ores containing high concentration of arsenic and antimony was considered. The analysis of the main methods shows that alkaline sulphide leaching is the most effective way to process off-grade copper concentrates. Leaching of concentrates' samples containing approximately 1,36% As and 19.2% Cu was studied in alkaline sulphide solutions containing sodium hydroxide and sodium sulphide

Experiments were carried out with the assistance of the laboratory base of St. Petersburg mining university's Common Use Centre. Experimental results of concerning the selective removal of arsenic are presented here.

Keywords: copper, arsenic, tennantite, enargite, sulphides, sulfosalt, alkaline leaching, ore processing

1 INTRODUCTION

For the copper industry it is the time of chances and challenges. The industry and the market have to face these challenges now, for seizing the chances coming its way in the future. The European Copper Institute predicts (the ECI 2017 Annual Report) the growth in copper consumption in the short term, taking into account the development of industries and expansion of the number of copper products applications.

However, one of the serious challenges for mining companies is the increase of the off-grade mineral reserves in the deposits. This situation is common for many companies of the mining industry including copper sector. Statistical database of the International Copper Study Group and the recent researches indicate that producers are exploiting deposits with low valuable components concentration in the ores.

In this situation copper deposits are being developed by mining companies, and valuable component content in the ore is ranging between 0.5 and 0.8%. This problem is further complicated by the fact that the relatively low-grade mineral resources being extracted are often unconventional and contain more than one valuable component. This leads to unavoidable losses of the valuable components in ore concentration processes and conversion into mining and mineral processing waste (Nevskaya et al., 2019) Consequently, the effective processing

and the utilisation of the raw materials with various quality characteristics became much more important for industrial companies.

In details, the changes in quality characteristic of the raw materials (especially steady decrease of the content of the valuable component in the ores) lead to the drop of the processing indicators of raw materials. The chemical and mineralogical compositions of the processed concentrates get worse. All these factors have influence on the final metallurgical product's cost.

High concentration of impure elements in the ore composition is also the problem for metallurgical companies. There are many orebodies or materials, which have significant value but also contain arsenic, throughout the world. Processing of copper ores (or any other ores) that contain arsenic is challenging. Arsenic is considered to be a human carcinogen with high mobility in aqueous streams, which in time may lead to increased arsenic concentrations in rivers (Oyarzun et al., 2004, 2006) and drinking water.

The presence of arsenic minerals in copper concentrates complicates their treatment by the conventional smelting-converting process. The sulphides and oxides of arsenic are highly volatile. Thus, in the pyrometallurgical treatment of copper concentrates with high arsenic content, there is a high risk of producing arsenic emissions to the atmosphere. Therefore, the smelters impose heavy penalties on copper concentrates that contain more than 0.5% arsenic (Ruiz M.C. et al., 2015).

Hydrometallurgical methods can be involved in treatment processes of arsenic containing materials, concentrates and ores as well as complex ones containing any number of metals. Industrial experience of these methods is known worldwide, in CIS, China and the United States the methods are employed for the production of antimony.

Despite the prevalence of pyrometallurgical processes, the global copper production by implementing hydrometallurgical approach increases (Fedoseev et al., 2018; Boduen et al., 2019). Amongst current technologies, an alkaline sulphide hydrometallurgical process has been demonstrated successful results in selective dissolution of arsenic and antimony from a copper concentrate containing enargite and tennantite (Prada et al., 2014; Tongamp et al., 2009; Baláž et al., 2006). In this paper, the process undertakes an alkaline sulphide leaching with a concentrated solution for transformation the arsenic sulphides into soluble compounds. The alkaline sulphide system is essentially a mixture of sodium sulphide and sodium hydroxide. It is an exclusive hydrometallurgical system - very selective lixiviant for the alkaline leaching of tin, gold, antimony, arsenic and mercury.

2 THE ROLE OF ARSENIC IN COPPER ORE PROCESSING

Copper production from the copper ores (or any ores) that contain arsenic is challenging due to certain factors. The common copper-arsenic bearing minerals in copper ores are enargite (Cu_3AsS_4) and tennantite ($Cu_{12}As_4S_{13}$). It should be noted that enargite and tennantite contain significant amounts of copper: 48.4% and 51.6% respectively. Chalcopyrite, which is employed more for copper production, has 34.5% of copper content. Removal of enargite and tennantite minerals from the concentrate means valuable metal losses, hence production income. Moreover, according to environmental and plant ecological concerns, pyrometallurgical operations will penalise concentrates that contain arsenic over 0.5% by weight (sometimes less). The presence of arsenic can also increase concentrates' shipping costs, since concentrates are commonly imported/exported overseas (Castro, 2008; Filippou et al., 2007).

Enargite and tennantite are part of the sulfosalt minerals' class. Sulfosalt minerals differ from sulphides in that semimetal elements such as antimony, arsenic or bismuth in sulphides substitute the sulphur positions, but in sulfosalts they substitute for the metal ions and bond with the sulphur.

There is a dearth of industrial experience and literature concerning the selective removal of arsenic from the copper ores during the processing. The up-to-date methods of processing copper-sulphide ores with mixture of sulfosalt minerals encompass a number of technological problems that significantly complicate the production process. In other words, at the stage of

ore preparation sulfosalt minerals are usually over grinded due to the very thin mutual germinating of the main ore-forming minerals: pyrite, chalcopyrite, and sphalerite and sulfosalt minerals.

Besides the similarity of the flotation properties of the minerals and over crushing of sulfoarsenides, the process of selective flotation is complicated, because of the main copper sulphides combined with tennantite might be easily turned to sludge, and that leads to higher losses of copper with processing tails as well as challenges in obtaining a conditioned copper concentrate.

Methods and experiments carried out by other researches (Prada et al., 2014; Tongamp et al., 2009; Baláž et al., 2006) have shown the results of arsenic extraction up to 97%. These results can be achieved by using the alkaline sulphide process for processing ores containing enargite and tennantite. In the presence of sulphide, arsenic is believed to transform and to form sodium thioarsenate as shown in the Equation 1:

$$Cu_{12}As_4S_{13} + 6NaOH + 6NaOH \rightarrow 5Cu_2S + 2CuS + 4Na_3AsS_3 + 6H_2O \quad (1)$$

Studying these methods and achievement the same arsenic extraction results for processing copper-arsenic concentrates and middling products were one of the key of this research work.

3 MATERIALS AND METHODOLOGY

3.1 *Sample preparation*

The samples of middling product and copper concentrate were received from the Uchalinskiy mining and processing plant (JSC «Uchalinsky GOK»), which is one of the largest industrial companies of Southern Ural, (production specialisation - zinc and copper concentrates).

The ores of the region demonstrate a decrease in the average content of valuable components (on average 10.0-15.0%), as well as a constant grow in the content of related elements such as arsenic, antimony, lead, mercury, fluorine. These raw materials are characterised as difficult to process, multicomponent, with unfavourable texture and structural features. Ore-forming minerals have similar processing properties (Nikolaeva, E.S. et al., 2019).

The samples of the study were the concentrate and middling product provided by the JSC «Uchalinsky GOK». The chemical analyses results (ICP) of the samples are presented in the Table 1.

The samples of middling product and copper concentrate were prepared in laboratory conditions by coning and quartering followed by splitting through a 10-channel splitter, obtaining 50 gram of leaching samples. A sample with P_{80} of approximately 50 μm was used for kinetic experiments at different temperatures. The particle size distribution for this sample is shown in Figure 1.

3.2 *Apparatus and procedure*

Experiments were carried out batch-wise in a 300 ml glass jacket cell under atmospheric pressure. Temperature was controlled by a thermostated water bath throughout the process.

Table 1. Chemical analysis of the copper concentrate and middling product (basic elements).

Sample	Content (wt. %)										
	Cu	Pb	Zn	Fe	Co	SiO_2	Al_2O_3	Cd	As	Sb	Ag
Copper concentrate UGOK	16.0	23.8	0.8	5.3	0.1	1.94	0.82	0.03	1.36	0.21	0.009
Middling UGOK	6.22	0.74	7.3	24.4	0.1	4.02	1.32	0.03	1.36	0.19	0.009

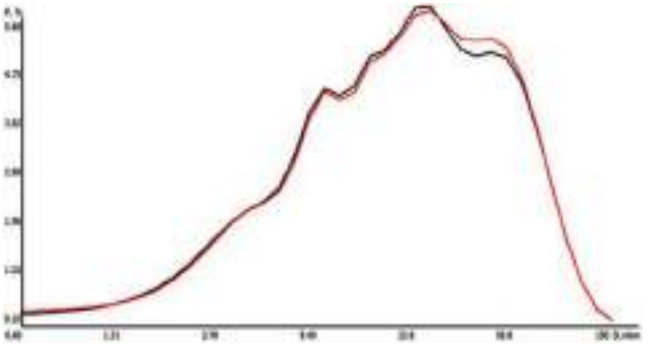

Figure 1. Particle size distribution for the enargite sample used for determination of the rate controlling process, P80 = 50 μm.

Agitation was provided by a mechanical paddle agitator during tests. All chemicals were of analytical grade and were used as received. In order to avoid evolution of hydrogen sulphide, leach solutions were prepared separately by dissolving sodium hydroxide in distilled water and dissolving sodium sulphide in distilled water in separate glass cell. Thereafter both solutions were mixed together in the glass jacket cell. It should be noted that all NaOH concentrations written below also include the NaOH produced by the hydrolysis of Na_2S according to the Equation 2.

$$Na_2S_{(aq)} + H_2O_{(l)} \leftrightarrow NaOH_{(aq)} + NaHS_{(aq)} \quad (2)$$

The samples for analysing, approximately 10 ml of pulp, were drawn from the leaching reactor periodically (in some test - only in the final stage), filtered and sent for analysis. The remaining pulp that was not used for analysis was immediately returned to the reactor. In this experimental work the studied parameters included concentration of sodium sulphide and sodium hydroxide, temperature, agitation, P_{80} and pulp density and their effect on the dissolution behaviour of arsenic, antimony, iron and copper.

4 RESULTS AND DISCUSSION

During the experimental work certain parameters were determined, studied and described. The effects of temperature and hydroxide concentration are important for the leaching kinetics. In general, Figure 2 shows that there is a clear improvement in the kinetics of arsenic removal as temperature is increased.

The best results were observed when both reagents were taken in high concentrations (4 M NaOH and 1.5 M Na_2S) - almost 100 % of arsenic extraction. This strong concentration and temperature dependence is very clear evidence that the controlling mechanism is a chemical reaction taking place on the surface of the particles (Levenspiel, 1999; Petrov, G. et al., 2018).

The decrease of the reagents' concentration declines the leaching rate significantly. Results of experiments 1 and 2 confirm that the concentration of both sodium hydroxide and sulphide has immediate impact on the leaching process (Table 2).

The temperature impact was studied in the range of 85, 90 и 95°C. In this group of experiments other parameters were kept constantly:

- process time – 4.5 hours;
- agitation rate – 600 rpm;
- reagents concentration – 3,5 M NaOH и 1,5 M Na_2S.

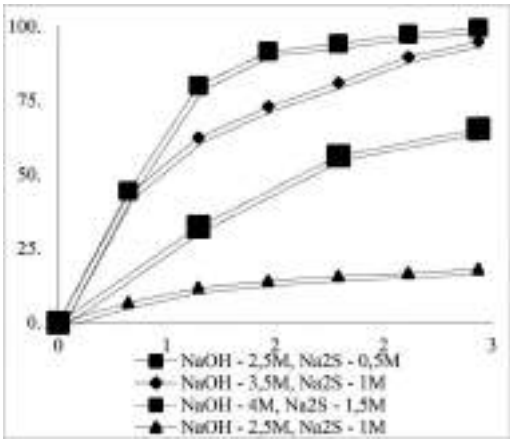

Figure 2. Effect of NaOH and Na_2S on the arsenic extraction at 95°C in 250 ml of solution.

Table 2. Parameters and results of experiments – the concentration influence.

Experiment	Temperature (°C)	Liquid/solid rate	Time (h)	Concentration		As removal (%)
				NaOH	Na_2S	
1	95	10	3	2.5	0.5	18.10
2				2.5	1.0	65.44
3				3.5	1.0	92.86
4				4.0	1.5	99.56

The results of experiments follow the same trend as previous ones. The highest temperature level provides the best arsenic removal rate (Figure 3; Table 3).

According to the results of experiments' analysis, copper and iron was found in leaching solutions in concentrations 12×10^{-4}(g/l) and 78×10^{-4}(g/l) respectively. This trend indicates high selectivity of leaching process.

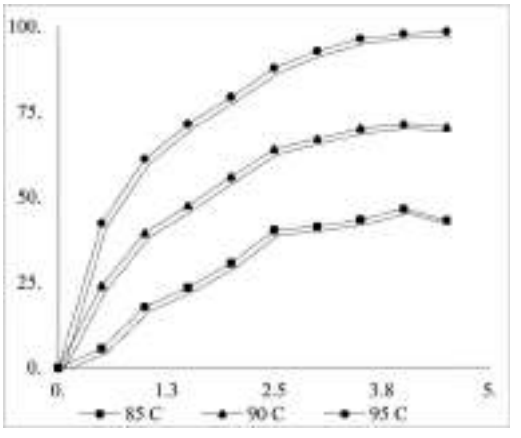

Figure 3. Effect of temperature on the arsenic extraction in 250 ml of solution with concentration 3,5 M NaOH и 1,5 M Na_2S.

Table 3. Parameters and results of experiments of the temperature impact.

Experiment	Temperature (°C)	Liquid/solid rate	Time (h)	Concentration		As removal (%)
				NaOH	Na_2S	
1	85	10	4.5	3.5	1.0	43.21
2	90					70.54
3	95					98.57

5 CONCLUSION

The existing industrial and scientific experience in technologies of arsenic extraction from copper concentrates and middling products does not provide appropriate solutions for the industry.

The existing methods of flotation cannot separate copper and zinc sulphides from sulfosalt minerals completely, that increases the concentration of arsenic in the product.

Therefore, the smelters impose heavy penalties on copper concentrates that contain more than 0.5% arsenic. All this factors makes this area of research very relevant.

The alkaline sodium sulphide leaching of copper concentrates and middling products efficiently removes arsenic, and produces a "pure" copper product. Due to this fact the selective leaching of arsenic and antimony using sodium sulphide in the alkaline solutions is a prospective way of upgrading copper-gold-silver concentrates to make them suitable for smelting. This fact creates an opportunity for the mining companies to extend the raw materials base for the production from off-grade mineral reserves.

At the moment, the main direction of modern research in this area is focused on the identification of effective reagent regime and influences of the mechanical activation on the process.

The reported study was funded by RFBR according to the research project 18-29-24103.

REFERENCES

Anderson, C.G. & Twidell, L.G. 2008. The alkaline sulphide hydrometallurgical separation, recovery and fixation of tin, arsenic, antimony, mercury and gold. *Lead and Zinc* 2008: 121–132.

Baláž, P., Achimovičová, M. 2006. Selective leaching of antimony and arsenic from mechanically activated tetrahedrite, jamesonite and enargite. *International Journal of Mineral Processing* 81: 44–50.

Boduen, A. & Fokina, S. & Petrov, G. & Andreev, Yu. (2019). Ammonia autoclave technology for the processing of low-grade concentrates generated in flotation concentration of cupriferous sandstones. Obogashchenie Rud. 33–38. 10.17580/or.2019.02.06.

Fedoseev, I. V., Barkan, M. S., Kornev, A. V., and Danilov, A. S. (2018). Theoretical Foundations and Technological Capabilities of Hydrocarbonyl Process of Recovering Copper from Technogenic Wastes. *Journal of Ecological Engineering*, 19(5), pp.33–37.

Filippou, D., St-Germain, P., Grammatikopoulos, T., 2007. Recovery of metal values from copper–arsenic minerals and other related resources. *Miner. Process. Extr. Metall. Rev*. 28 (4): 247–298.

Nadkarni, R.M & Kusik, C.L. 1988. Hydrometallurgical removal of arsenic from copper concentrates. Arsenic Metallurgy Fundam. Appl. Proc. Symp: 263–286.

Nevskaya, M.A.; Seleznev, S.G.; Masloboev, V.A.; Klyuchnikova, E.M.; Makarov, D.V. Environmental and Business Challenges Presented by Mining and Mineral Processing Waste in the Russian Federation. Minerals 2019, 9, 445.

Nikolaeva, E.S., Talovina, I.V., Nikiforova, V.S., Heide, G. 2019. Chemical composition and genesis of serpentinite group minerals in nickeliferous weathering crust of the Elov deposit (Urals). *Scientific and Practical Studies of Raw Material Issues*: 3–10.

Oyarzun, R., Guevara, S., Oyarzun, J., Lillo, J., Maturana, H., Higueras, P. 2006. The Ascontaminated Elqui river basin: a long lasting perspective (1975–1995) covering the initiation and development of Au–Cu–As mining in the high Andes of northern Chile. *Environ. Geochem. Health* 28 (5): 431–443.

Oyarzun, R., Lillo, J., Higueras, P., Oyarzun, J., Maturana, H. 2004. Strong arsenic enrichment in sediments from the Elqui watershed, northern Chile: industrial (gold mining at El Indio-Tambo district) vs. geologic processes. *J. Geochem. Explor*. 84 (2): 53–64.

Parada, F., Jeffrey, M.I., Asselin, E. 2014. Leaching kinetics of enargite in alkaline sodium sulphide solutions. *Hydrometallurgy* 146: 48–58.

Petrov, G. V. & Fokina, S. B. & Boduen, A.Y. & Zotova, I.E. & Fidarov, B.F. 2018. Arsenic behavior in the autoclave-hydrometallurgical processing of refractory sulfide gold-platinum-bearing products. *International Journal of Engineering and Technology (UAE)* 7: 35–39.

Tongamp, W., Takasaki,Y. & Shibayama, A. 2009. Arsenic removal from copper ores and concentrates through alkaline leaching in NaHS media. *Hydrometallurgy* 98: 213–218.

Advances in Raw Material Industries for Sustainable Development Goals – Litvinenko (Ed)
© 2021 Taylor & Francis Group, London, ISBN 978-0-367-75881-3

Spectral-time analysis of relaxation and creep processes of polymeric materials

N. Pereborova
PhD, Associate Professor, Associate Professor of the Department of Intelligent Systems and Information Security Saint Petersburg State University of Industrial Technologies and Design, Saint Petersburg, Russia

A. Makarov
Vice-Rector of Science, Saint Petersburg State University of Industrial Technologies and Design, Saint Petersburg, Russia

A. Demidov
Rector, Saint Petersburg State University of Industrial Technologies and Design, Saint Petersburg, Russia

V. Wagner
PhD, Associate Professor of the Department of Intelligent Systems and Information Security Saint Petersburg State University of Industrial Technologies and Design, Saint Petersburg, Russia

ABSTRACT: The article investigates into the type of distributions of relaxing and delay particles over their relaxation and delay times built upon the mathematical models of relaxation and creep of polymeric materials. The relaxation and delay times characterise the transition times of relaxing or delay particles from one stable energy state to another (Makarov et al., 2016).

The nature of such transitions can be different. It depends on both the rheology of a polymer material and the applied deformation or load value. It can be explained, on the one hand, by conformational energy transfers within the macromolecules of material when their shape changes during rearrangement, and on the other hand, there are shears of macromolecules and other changes caused by energy (Makarov et al., 2015a). The most satisfactory results considering the processes of deformation of polymeric materials can be obtained using rather complex models such as a consequent combination of a number of the Maxwell and the Kelvin-Voigt models (Pereborova et al., 2020a). The application of modelling for an accurate quantitative description of deformation or relaxation in the study of the properties of polymers encounters certain difficulties (Pereborova et al., 2020b). Different operational behaviour of polymers, structural changes during deformation depending on the sample background, temperature, duration of action, and stress-strain values, make it difficult to obtain the exact rheological characteristics of the process (Pereborova et al., 2020c). However, the relevance of modelling for a qualitative or approximate quantitative description of mechanical properties is obvious.

1 THE METHODS FOR DETERMINING THE SPECTRA OF RELAXATION AND DELAY

One of the methods for describing deformation and relaxation processes of polymer materials is the use of mechanical models. The limits and prospects of application of deformation processes modelling of polymers were considered in a number of studies carried out by V. A. Kargin (Pereborova et al., 2020d), G. L. Slonimskiy (Pereborova et al., 2020e), A .A. Askadskiy (Makarov et al., 2018a), I. Ward (Pereborova et al., 2019a) and other authors.

The study of relationships between various viscoelastic functions often deals with the relaxation and delay (creep) spectra. The essence of these spectra can be shown on the example of

the Generalised Maxwell model (for relaxation) and on the example of the Generalised Kelvin-Voigt model (Pereborova et al., 2018a).

The Generalised Maxwell model represents an infinite parallel set of Maxwell elements consisting of a dashpot and a spring connected in series (Figure 1.).

Consider the element at the i -th place. If the stiffness of a spring is denoted by E_i, and the viscosity of the liquid where a dashpot η_i is located, then the relaxation time of the i -th element is obtained by $\tau_i = \frac{\eta_i}{E_i}$ and is a measure of the time required for stress relaxation.

Any number of Maxwell's elements connected in series has the properties of both the element itself and other more complex properties. This fact leads to a discrete spectrum of relaxation times $\{\tau_i\}$ (Pereborova et al., 2018b).

A similar statement can be made for the delay (creep) spectrum on the example of the Generalised Kelvin-Voigt model which is an infinite parallel set of Kelvin-Voigt elements consisting of a dashpot and a spring connected in series (Figure 2.) (Egorov et al., 2020).

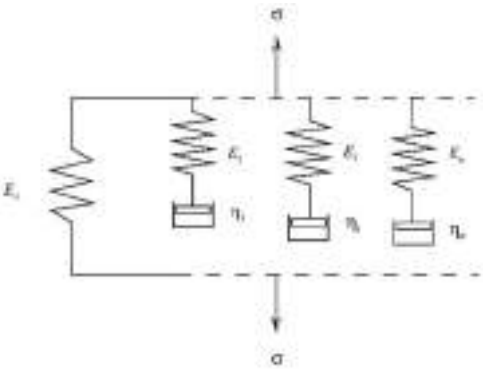

Figure 1. The Generalised Maxwell model.

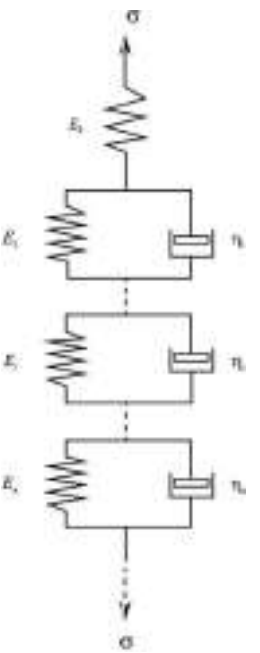

Figure 2. The Generalised Kelvin-Voigt model.

If the element is at the i -th place consists of a spring with stiffness Ei, and the viscosity of the liquid where a dashpot is located η_i, then the delay time of the i -th element is obtained by $\tau_i = \frac{\eta_i}{E_i}$ and is a measure of the time required for the spring to strain to its equilibrium length in the presence of the viscous element braking forces (Pereborova et al., 2019b).

2 OBTAINING OF THE RELAXATION SPECTRA OF POLYMERIC MATERIALS

Sufficient approximations of the relaxation and delay spectra can be found by processing the experimental sets of relaxation and creep, respectively. Obtaining the relaxation and delay spectra means finding the distribution of the relaxation times and delay times that cannot be found experimentally.

To obtain the analytical form of the relaxation spectrum of polymeric materials, a variant of the mathematical model of the relaxation process can be used in the form (Rymkevich et al., 2013).

$$\sigma_t = E_0\varepsilon_t - (E_0 - E_\infty)\cdot\int_0^t \varepsilon_\theta \cdot \varphi'_{\varepsilon;t-\theta}d\theta, \tag{1}$$

where
ε_t- time-dependent deformation t,
σ_t - time-dependent stress t,
E_0 - elastic modulus,
E_∞ - viscoelastic modulus,

$$\varphi_{\varepsilon t} = \frac{1}{2}\cdot\left(1 + th\left(\frac{A_\varepsilon}{2}\cdot\ln\left(\frac{t}{\tau_\varepsilon}\right)\right)\right) \tag{2}$$

normalised relaxation function that forms the basis of the mathematical model of relaxation (Pereborova et al., 2019c),

$$\begin{aligned}\varphi'_{\varepsilon t} = \bar{r}_{\varepsilon t} = \frac{\partial\varphi_{\varepsilon t}}{\partial(\ln t)} = \frac{A_\varepsilon}{4}\cdot\frac{1}{ch^2(W_{\varepsilon t})} = \\ = \frac{A_\varepsilon}{4}\cdot\left(1 - th^2(W_{\varepsilon t})\right) = A_\varepsilon\cdot\varphi_{\varepsilon t}\cdot(1-\varphi_{\varepsilon t})\end{aligned} \tag{3}$$

integral relaxation kernel,

$$W_{\varepsilon t} = \frac{A_\varepsilon}{2}\cdot\ln\frac{t}{\tau_\varepsilon} = \frac{A_\varepsilon}{2}\cdot\left(\ln\left(\frac{t}{t_1}\right) + \ln\left(\frac{t_1}{\tau_\varepsilon}\right)\right) \tag{4}$$

A_ε - parameter of the intensity of relaxation processes,

$$f_{\varepsilon,\tau_\varepsilon} = \ln\left(\frac{t}{\tau_\varepsilon}\right) \tag{5}$$

logarithmic function of the relaxation times.

The analytical form of the relaxation spectrum $\bar{H}_{\varepsilon\tilde{\tau}}$ can be obtained by the known formula (Pereborova et al., 2018c)

$$\int_0^{\infty} \bar{H}_{\varepsilon\tilde{\tau}} \cdot e^{-tx} \cdot dx = \frac{d\varphi_{\varepsilon t}}{dt} = r_{\varepsilon t} \tag{6}$$

by successive approximations.

The given formula (6) is the Laplace transform in which the relaxation spectrum $\bar{H}_{\varepsilon\tilde{\tau}}$ plays the role of the original, and the relaxation kernel $r_{\varepsilon t}$ plays the role of the figure in terms of operator calculus. This dependence (6) is obtained on the basis of the properties of the Generalised Maxwell model (Pereborova et al., 2018d).

The application of the hyperbolic tangent function as the normalised relaxation function (2) leads to the following logarithmic relaxation kernel

$$E'_{\varepsilon t} = \frac{\partial E_{\varepsilon t}}{\partial \ln t} = -(E_0 - E_\infty) \cdot \bar{r}_{\varepsilon t} = -\frac{A_\varepsilon}{4} \cdot (E_0 - E_\infty) \cdot \left(1 - th^2(W_{\varepsilon t})\right) \tag{7}$$

The deformation-time argument (4) of the relaxation kernel (3) takes into account the current time factor and the characteristically average internal relaxation times. In the known approximation, the relaxation kernel (3) characterises the distribution of relaxing particles over their micromechanical relaxation times (Pereborova et al., 2020f).

In order to obtain approximations of the normalised relaxation spectrum, the known recurrence formulas can be used (Gorshkov et al., 2013a) if $k = 1$

$$\overline{H}_1 = \frac{\partial \varphi_{\varepsilon t}}{\partial \ln t} = \varphi'_{\varepsilon t} = \bar{r}_{\varepsilon t}\Big|_{t=\tilde{\tau}} \tag{8}$$

and if $k \quad 2$

$$\bar{H}_k = \bar{H}_{k-1} - \frac{1}{k-1} \cdot \frac{d\bar{H}_{k-1}}{d\ln\tilde{\tau}}\Big|_{t=(k-1)\tilde{\tau}} \tag{9}$$

For calculating the values of the derivatives $\bar{r}_{\varepsilon t} = \frac{\partial \varphi_{\varepsilon t}}{\partial \ln t}, \ldots, \frac{\partial^k \varphi_{\varepsilon t}}{\partial \ln t^k}, \ldots$, where for the relaxation function $\varphi_{\varepsilon t} = \varphi$ the hyperbolic tangent (2) is chosen and $W_{\varepsilon t} = W$ is the structure-deformation-time argument-functional (4), we obtain

$$\varphi_{\varepsilon t} = \frac{1}{2} \cdot \left(1 + th\left(\frac{A_\varepsilon}{2} \cdot \ln\left(\frac{t}{\tau_\varepsilon}\right)\right)\right) \tag{10}$$

$$\varphi'_{\varepsilon t} = \bar{r}_{\varepsilon t} = \frac{\partial \varphi_{\varepsilon t}}{\partial(\ln t)} = \frac{A_\varepsilon}{4} \cdot \frac{1}{ch^2(W_{\varepsilon t})} = \frac{A_\varepsilon}{4} \cdot \left(1 - th^2(W_{\varepsilon t})\right) = A_\varepsilon \cdot \varphi_{\varepsilon t} \cdot (1 - \varphi_{\varepsilon t}) \tag{11}$$

$$\varphi''_{\varepsilon t} = \frac{\partial^2 \varphi_{\varepsilon t}}{\partial(\ln t)^2} = A_\varepsilon^2 \cdot \varphi_{\varepsilon t} \cdot (1 - \varphi_{\varepsilon t}) \cdot (1 - 2 \cdot \varphi_{\varepsilon t}) \tag{12}$$

$$\varphi'''_{\varepsilon t} = \frac{\partial^3 \varphi_{\varepsilon t}}{\partial(\ln t)^3} = A_\varepsilon^3 \cdot \varphi_{\varepsilon t} \cdot (1 - \varphi_{\varepsilon t}) \cdot \left(1 - 6 \cdot \varphi_{\varepsilon t} + 6 \cdot \varphi_{\varepsilon t}^2\right) \tag{13}$$

$$\varphi^{IV}_{\varepsilon t} = \frac{\partial^4 \varphi_{\varepsilon t}}{\partial(\ln t)^4} = A_\varepsilon^4 \cdot \varphi_{\varepsilon t} \cdot (1 - \varphi_{\varepsilon t}) \times \left(1 - 14 \cdot \varphi_{\varepsilon t} + 36 \cdot \varphi_{\varepsilon t}^2 - 24 \cdot \varphi_{\varepsilon t}^3\right) \tag{14}$$

$$\varphi^{v}_{\varepsilon t} = \frac{\partial^5 \varphi_{\varepsilon t}}{\partial(\ln t)^5} = A_\varepsilon^5 \cdot \varphi_{\varepsilon t} \cdot (1 - \varphi_{\varepsilon t}) \times \left(1 - 30 \cdot \varphi_{\varepsilon t} + 150 \cdot \varphi_{\varepsilon t}^2 - 240 \cdot \varphi_{\varepsilon t}^3 + 120 \cdot \varphi_{\varepsilon t}^4\right) \tag{15}$$

$$\varphi_{\varepsilon t}^{vi} = \frac{\partial^6 \varphi_{\varepsilon t}}{\partial (\ln t)^6} = A_\varepsilon^6 \cdot \varphi_{\varepsilon t} \cdot (1 - \varphi_{\varepsilon t}) \cdot (1 - 62 \cdot \varphi_{\varepsilon t} + \\ + 510 \cdot \varphi_{\varepsilon t}^2 - 1560 \cdot \varphi_{\varepsilon t}^3 + 1800 \cdot \varphi_{\varepsilon t}^4 - 720 \cdot \varphi_{\varepsilon t}^5) \tag{16}$$

$$\varphi_{\varepsilon t}^{vii} = \frac{\partial^7 \varphi_{\varepsilon t}}{\partial (\ln t)^7} = A_\varepsilon^6 \cdot \varphi_{\varepsilon t} \cdot (1 - \varphi_{\varepsilon t}) \cdot \left(1 - 126 \cdot \varphi_{\varepsilon t} + 1716 \cdot \varphi_{\varepsilon t}^2 - \right. \\ \left. - 8280 \cdot \varphi_{\varepsilon t}^3 + 16800 \cdot \varphi_{\varepsilon t}^4 - 15120 \cdot \varphi_{\varepsilon t}^5 + 5040 \cdot \varphi_{\varepsilon t}^6\right) \tag{17}$$

Using the recurrence formulas (8), (9) that in expanded form are given by

$$\overline{H}_1 = \frac{\partial \varphi}{\partial \ln t} = \varphi' = \overline{r_{\varepsilon t}}\Big|_{t=\tilde{\tau}} \tag{18}$$

$$\overline{H}_2 = \frac{\partial \varphi}{\partial \ln t} - \frac{\partial^2 \varphi}{\partial \ln t^2} = \varphi' - \varphi''\Big|_{t=\tilde{\tau}} \tag{19}$$

$$\overline{H}_3 = \varphi' - \frac{3}{2}\varphi'' + \frac{1}{2}\varphi'''\Big|_{t=2\tilde{\tau}} \tag{20}$$

$$\overline{H}_4 = \varphi' - \frac{11}{6}\varphi'' + \varphi''' - \frac{1}{6}\varphi^{iv}\Big|_{t=3\tilde{\tau}} \tag{21}$$

$$\overline{H}_5 = \varphi' - \frac{25}{12}\varphi'' + \frac{35}{24}\varphi''' - \frac{5}{12}\varphi^{iv} + \frac{1}{24}\varphi^{v}\Big|_{t=4\tilde{\tau}} \tag{22}$$

$$\overline{H}_6 = \varphi' - \frac{137}{60}\varphi'' + \frac{15}{8}\varphi''' - \frac{17}{24}\varphi^{iv} + \frac{3}{24}\varphi^{v} - \frac{1}{120}\varphi^{vi}\Big|_{t=5\tilde{\tau}} \tag{23}$$

$$\overline{H}_7 = \varphi' - \frac{49}{20}\varphi'' + \frac{203}{90}\varphi''' - \\ - \frac{49}{48}\varphi^{iv} + \frac{35}{144}\varphi^{v} - \frac{7}{240}\varphi^{vi} + \frac{1}{720}\varphi^{vii}\Big|_{t=6\tilde{\tau}} \tag{24}$$

we obtain expressions for approximations of the normalised relaxation spectrum

$$\overline{H}_1 = \frac{\partial \varphi_{\varepsilon t}}{\partial (\ln t)}\Big|_{t=\tilde{\tau}} = \varphi'_{\varepsilon t}|_{t=\tilde{\tau}} = A_\varepsilon \cdot \varphi_{\varepsilon t} \cdot (1 - \varphi_{\varepsilon t})\Big|_{t=\tilde{\tau}} \tag{25}$$

$$\overline{H}_2 = \varphi'_{\varepsilon t} - \varphi''_{\varepsilon t}|_{t=\tilde{\tau}} = A_\varepsilon \cdot \varphi_{\varepsilon t} \cdot (1 - \varphi_{\varepsilon t}) \cdot (1 - A_\varepsilon(1 - 2 \cdot \varphi_{\varepsilon t}))\big|_{t=\tilde{\tau}} \tag{26}$$

$$\overline{H}_3 = \varphi'_{\varepsilon t} - \frac{3}{2}\varphi''_{\varepsilon t} + \frac{1}{2}\varphi'''_{\varepsilon t}\Big|_{t=2\tilde{\tau}} = A_\varepsilon \cdot \varphi_{\varepsilon t} \cdot (1 - \varphi_{\varepsilon t}) \times \\ \times \left(1 - \frac{3}{2} \cdot A_\varepsilon \cdot (1 - 2 \cdot \varphi_{\varepsilon t}) + \frac{1}{2} \cdot A_\varepsilon^2 \cdot \left(1 - 6 \cdot \varphi_{\varepsilon t} + 6 \cdot \varphi_{\varepsilon t}^2\right)\right)\Big|_{t=2\tilde{\tau}} \tag{27}$$

$$\overline{H}_4 = \varphi'_{\varepsilon t} - \frac{11}{6}\varphi''_{\varepsilon t} + \varphi'''_{\varepsilon t} - \frac{1}{6}\varphi''''_{\varepsilon t}\Big|_{t=3\tilde{\tau}} = A_\varepsilon \cdot \varphi_{\varepsilon t} \cdot (1 - \varphi_{\varepsilon t}) \times \\ \times \left(1 - \frac{11}{6} \cdot A_\varepsilon \cdot (1 - 2 \cdot \varphi_{\varepsilon t}) + A_\varepsilon^2 \cdot \left(1 - 6 \cdot \varphi_{\varepsilon t} + 6 \cdot \varphi_{\varepsilon t}^2\right) - \right. \\ \left. - \frac{1}{6} \cdot A_\varepsilon^3 \cdot \left(1 - 14 \cdot \varphi_{\varepsilon t} + 36 \cdot \varphi_{\varepsilon t}^2 - 24 \cdot \varphi_{\varepsilon t}^3\right)\right)\Big|_{t=3\tilde{\tau}} \tag{28}$$

$$\overline{H}_5 = \varphi'_{\varepsilon t} - \frac{25}{12}\varphi''_{\varepsilon t} + \frac{35}{24}\varphi'''_{\varepsilon t} - \frac{5}{12}\varphi''''_{\varepsilon t} + \frac{1}{24}\varphi'''''_{\varepsilon t}\Big|_{t=4\tilde{\tau}} =$$
$$= A_\varepsilon \cdot \varphi_{\varepsilon t} \cdot (1 - \varphi_{\varepsilon t}) \cdot \left(1 - \frac{25}{12} \cdot A_\varepsilon \cdot (1 - 2 \cdot \varphi_{\varepsilon t}) + \frac{35}{24} \cdot A_\varepsilon^2 \times \right.$$
$$\times \left(1 - 6 \cdot \varphi_{\varepsilon t} + 6 \cdot \varphi_{\varepsilon t}^2\right) - \frac{5}{12} \cdot A_\varepsilon^3 \cdot \left(1 - 14 \cdot \varphi_{\varepsilon t} + 36 \cdot \varphi_{\varepsilon t}^2 - 24 \cdot \varphi_{\varepsilon t}^3\right) +$$
$$\left. + \frac{1}{24} \cdot A_\varepsilon^4 \cdot \left(1 - 30 \cdot \varphi_{\varepsilon t} + 150 \cdot \varphi_{\varepsilon t}^2 - 240 \cdot \varphi_{\varepsilon t}^3 + 120 \cdot \varphi_{\varepsilon t}^4\right)\right)\Big|_{t=4\tilde{\tau}} \tag{29}$$

$$\overline{H}_6 = \varphi'_{\varepsilon t} - \frac{137}{60}\varphi''_{\varepsilon t} + \frac{15}{8}\varphi'''_{\varepsilon t} - \frac{17}{24}\varphi^{IV}_{\varepsilon t} + \frac{1}{8}\varphi^{V}_{\varepsilon t} - \frac{1}{120}\varphi^{VI}_{\varepsilon t}\Big|_{t=5\tilde{\tau}} =$$
$$= A_\varepsilon \cdot \varphi_{\varepsilon t} \cdot (1 - \varphi_{\varepsilon t}) \cdot \left(1 - \frac{137}{60} \cdot A_\varepsilon \cdot (1 - 2 \cdot \varphi_{\varepsilon t}) + \frac{15}{8} \cdot A_\varepsilon^2 \times \right.$$
$$\times \left(1 - 6 \cdot \varphi_{\varepsilon t} + 6 \cdot \varphi_{\varepsilon t}^2\right) - \frac{17}{24} \cdot A_\varepsilon^3 \cdot \left(1 - 14 \cdot \varphi_{\varepsilon t} + 36 \cdot \varphi_{\varepsilon t}^2 - 24 \cdot \varphi_{\varepsilon t}^3\right) +$$
$$+ \frac{1}{8} \cdot A_\varepsilon^4 \cdot \left(1 - 30 \cdot \varphi_{\varepsilon t} + 150 \cdot \varphi_{\varepsilon t}^2 - 240 \cdot \varphi_{\varepsilon t}^3 + 120 \cdot \varphi_{\varepsilon t}^4\right) - \frac{1}{120} \cdot A_\varepsilon^5 \times$$
$$\left. \times \left(1 - 62 \cdot \varphi_{\varepsilon t} + 510 \cdot \varphi_{\varepsilon t}^2 - 1560 \cdot \varphi_{\varepsilon t}^3 + 1800 \cdot \varphi_{\varepsilon t}^4 - 720 \cdot \varphi_{\varepsilon t}^5\right)\right)\Big|_{t=5\tilde{\tau}} \tag{30}$$

$$\overline{H}_7 = \varphi'_{\varepsilon t} - \frac{49}{20}\varphi''_{\varepsilon t} + \frac{203}{90}\varphi'''_{\varepsilon t} - \frac{49}{48}\varphi^{IV}_{\varepsilon t} + \frac{35}{144}\varphi^{V}_{\varepsilon t} - \frac{7}{240}\varphi^{VI}_{\varepsilon t} +$$
$$+ \frac{1}{720}\varphi^{VII}_{\varepsilon t}\Big|_{t=6\tilde{\tau}} = A_\varepsilon \cdot \varphi_{\varepsilon t} \cdot (1 - \varphi_{\varepsilon t}) \cdot \left(1 - \frac{49}{20} \cdot A_\varepsilon \cdot (1 - 2 \cdot \varphi_{\varepsilon t}) + \right.$$
$$+ \frac{203}{90} \cdot A_\varepsilon^2 \cdot \left(1 - 6 \cdot \varphi_{\varepsilon t} + 6 \cdot \varphi_{\varepsilon t}^2\right) - \frac{49}{48} \cdot A_\varepsilon^3 \cdot \left(1 - 14 \cdot \varphi_{\varepsilon t} + 36 \cdot \varphi_{\varepsilon t}^2 - \right.$$
$$\left. - 24 \cdot \varphi_{\varepsilon t}^3\right) + \frac{35}{144} \cdot A_\varepsilon^4 \cdot \left(1 - 30 \cdot \varphi_{\varepsilon t} + 150 \cdot \varphi_{\varepsilon t}^2 - 240 \cdot \varphi_{\varepsilon t}^3 + 120 \cdot \varphi_{\varepsilon t}^4\right) -$$
$$- \frac{7}{240} \cdot A_\varepsilon^5 \cdot \left(1 - 62 \cdot \varphi_{\varepsilon t} + 510 \cdot \varphi_{\varepsilon t}^2 - 1560 \cdot \varphi_{\varepsilon t}^3 + \right.$$
$$+ 1800 \cdot \varphi_{\varepsilon t}^4 - 720 \cdot \varphi_{\varepsilon t}^5\left) + \frac{1}{720} \cdot A_\varepsilon^6 \cdot \left(1 - 126 \cdot \varphi_{\varepsilon t} + 1760 \cdot \varphi_{\varepsilon t}^2 - \right.\right.$$
$$\left.\left. - 8280 \cdot \varphi_{\varepsilon t}^3 + 16800 \cdot \varphi_{\varepsilon t}^4 - 15120 \cdot \varphi_{\varepsilon t}^5 + 5040 \cdot \varphi_{\varepsilon t}^6\right)\right)\Big|_{t=6\tilde{\tau}} \tag{31}$$

The obtained results (25) – (31) can be represented by a single formula (Makarov et al., 2017a).

$$\bar{H}_k = \bar{r}_{\varepsilon t} \cdot \sum_{i=1}^{k} \left(A_\varepsilon^{i-1} \cdot P_{ki}(\varphi_{\varepsilon t})\right)\Big|_{t=(k-1)\tilde{\tau}} \tag{32}$$

where $P_{ki}(\varphi_{\varepsilon t})$ - polynomials of a degree i-1 from $\varphi_{\varepsilon t}$. The type of the polynomials $P_{ki}(\varphi_{\varepsilon t})$ ← is shown in Table 1.

Therefore, the relaxation spectrum obtained on the basis of the mathematical model of the relaxation process (1) using the hyperbolic tangent (2) as the normalised relaxation function is completely determined by the structural coefficient A_ε depending on a polymer material and a type of the polynomials $P_{ki}(\varphi_{\varepsilon t})$ that do not depend on a polymer material but are characteristics of the mathematical model itself (Demidov et al., 2017).

From the analytical form of the relaxation spectrum approximations $\bar{H}_k$, it is evident that these approximations converge rather quickly to their limiting value $\bar{H}$ which characterises the stability of the chosen mathematical model of the relaxation process (1) based on the

Table 1. The type of polynomials $P_{ki}(\varphi_{\varepsilon t})$ included in the formulas for approximations of the relaxation spectra of polymer materials.

i\k	1	2	3	4	5
1	1	1	1	1	1
2	-	$2\varphi - 1$	$3\varphi - \frac{3}{2}$	$\frac{11}{3}\varphi - \frac{11}{6}$	$\frac{25}{6}\varphi - \frac{25}{12}$
3	-	-	$3\varphi^2 - 3\varphi + \frac{1}{2}$	$6\varphi^2 - 6\varphi + 1$	$\frac{35}{4}\varphi^2 - \frac{35}{4}\varphi + \frac{35}{24}$
4	-	-	-	$4\varphi^3 - 6\varphi^2 + \frac{7}{3}\varphi - \frac{1}{6}$	$10\varphi^3 - 15\varphi^2 + \frac{35}{6}\varphi - \frac{5}{12}$
5	-	-	-	-	$5\varphi^4 - 10\varphi^3 + \frac{25}{4}\varphi^2 - \frac{5}{4}\varphi + \frac{1}{24}$

i\k	6	7
1	1	1
2	$\frac{137}{30}\varphi - \frac{137}{60}$	$\frac{49}{10}\varphi - \frac{49}{20}$
3	$\frac{45}{4}\varphi^2 - \frac{45}{4}\varphi + \frac{15}{8}$	$\frac{203}{15}\varphi^2 - \frac{203}{15}\varphi + \frac{203}{90}$
4	$17\varphi^3 - \frac{51}{2}\varphi^2 + \frac{119}{12}\varphi - \frac{17}{24}$	$\frac{49}{2}\varphi^3 - \frac{147}{4}\varphi^2 + \frac{343}{24}\varphi - \frac{49}{48}$
5	$15\varphi^4 - 30\varphi^3 + \frac{75}{4}\varphi^2 - \frac{15}{4}\varphi + \frac{1}{8}$	$\frac{175}{6}\varphi^4 - \frac{175}{3}\varphi^3 + \frac{875}{24}\varphi^2 - \frac{175}{24}\varphi + \frac{35}{144}$
6	$6\varphi^5 - 15\varphi^4 + 13\varphi^3 - \frac{17}{4}\varphi^2 + \frac{31}{60}\varphi - \frac{1}{120}$	$21\varphi^5 - \frac{105}{2}\varphi^4 + \frac{91}{2}\varphi^3 - $ $- \frac{119}{8}\varphi^2 + \frac{217}{120}\varphi - \frac{7}{240}$
7	-	$7\varphi^6 - 21\varphi^5 + \frac{70}{3}\varphi^4 - \frac{23}{2}\varphi^3 + $ $+ \frac{110}{45}\varphi^2 - \frac{31}{180}\varphi + \frac{1}{720}$

hyperbolic tangent (2). This means that, with a small permissible error, as the relaxation spectrum its first approximation can be accepted, which is given by (Makarov et al., 2017b).

$$\overline{H}_1 = A_\varepsilon \cdot \varphi_{\varepsilon t} \cdot (1 - \varphi_{\varepsilon t})|_{t=\tilde{\tau}} \tag{33}$$

and depends only on the structural coefficient A_ε and on the relaxation function $\varphi_{\varepsilon t}$ (2).

Taking into account that the approximations of the spectrum of relaxation times $\bar{H}_{\varepsilon\tilde{\tau}}$ are obtained by the logarithmic time scale derivatives of the normalised relaxation function (2) and knowing the type of the relaxation spectrum, the inverse problem can be solved. It is possible to obtain the corresponding normalised relaxation function by integrating. That is the basis of the mathematical model of viscoelastic properties of polymeric materials (Pereborova, 2020g).

The example of the relaxation spectrum of a polyester thread 83 tex. is shown in Figure 3. And the corresponding spectrum of the relaxation times of a polyester fabric made from polyester threads 83 tex. is shown in Figure 4.

Analysing the graphs of the relaxation times spectra of a polyester thread 83 tex. and a polyester fabric made of polyester threads 83 tex., it can be noted that the intensity parameter corresponds to a polyester thread $A_\varepsilon = 0,14$, while in a polyester fabric it is much higher $A_\varepsilon = 0,92$ which leads to a more pronounced shape of the relaxation spectrum curve (Figure 3., Figure 4.) (Makarov et al., 2015b).

It should be noted that the modified logarithmic time scale contains the deformation-time function

$$\ln\frac{t}{\tau_\varepsilon} = \ln\frac{t}{t_1} + \ln\frac{t_1}{\tau_\varepsilon} \tag{34}$$

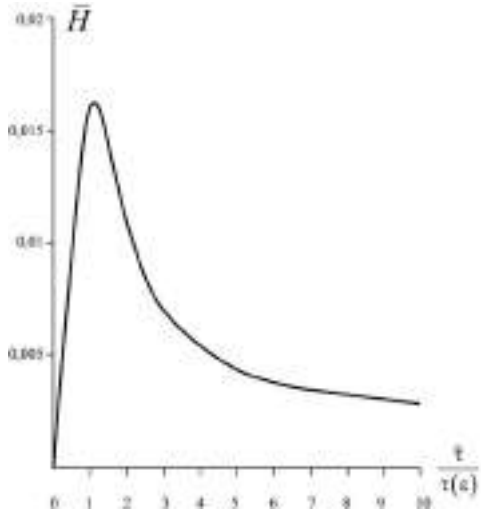

Figure 3. The graph of the spectrum of relaxation times of a polyester thread 83 tex., $T = 40°C$.

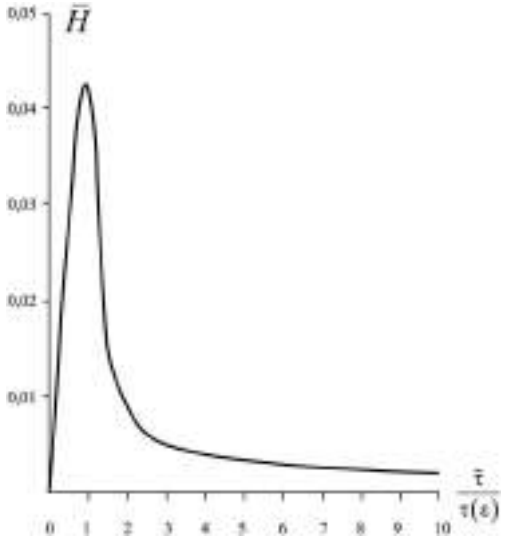

Figure 4. The graph of the spectrum of relaxation times of polyester fabric for technical purposes, $T = 40\,°C$.

reflecting the deformation-time analogy. Due to this time modification, the obtained relaxation spectra are generalised, that means, they extend to the entire initial range of non-destructive deformation (Makarov et al., 2014a).

3 OBTAINING OF THE DELAY SPECTRA OF POLYMERIC MATERIALS

To obtain the analytical form of the delay spectrum of polymeric materials, a variant of the mathematical model of the creep process can be used in the form (Demidov et al., 2006a).

where

$$\varepsilon_t = D_0\sigma_t + (D_\infty - D_0)\cdot\int_0^t \sigma_\theta \cdot \varphi'_{\sigma;t-\theta}d\theta \tag{35}$$

ε_t - time-dependent deformation t,
σ_t - time-dependent stress t,
D_0 - initial elastic compliance,
D_∞ - finite quasiequilibrium compliance,

$$\varphi_{\sigma t} = \frac{1}{2}\cdot\left(1 + th\left(\frac{A_\sigma}{2}\cdot\ln\left(\frac{t}{\tau_\sigma}\right)\right)\right) \tag{36}$$

normalised delay function that forms the basis of the mathematical model of creep (Demidov et al., 2009),

$$\varphi'_{\sigma t} = \bar{r}_{\sigma t} = \frac{\partial\varphi_{\sigma t}}{\partial(\ln t)} = \frac{A_\sigma}{4}\cdot\frac{1}{ch^2(W_{\sigma t})} = \frac{A_\sigma}{4}\cdot\left(1 - th^2(W_{\sigma t})\right) = A_\sigma\cdot\varphi_{\sigma t}\cdot(1-\varphi_{\sigma t}) \tag{37}$$

integral delay kernel,

$$W_{\sigma t} = \frac{A_\sigma}{2}\cdot\ln\frac{t}{\tau_\sigma} = \frac{A_\sigma}{2}\cdot\left(\ln\left(\frac{t}{t_1}\right) + \ln\left(\frac{t_1}{\tau_\sigma}\right)\right) \tag{38}$$

A_σ - parameter of the intensity of creep processes,

$$f_{\sigma,\tau_\sigma} = \ln\left(\frac{t}{\tau_\sigma}\right) \tag{39}$$

logarithmic function of the delay times.

The analytical form of the delay spectrum $\bar{Q}_{\sigma\tilde{\tau}}$ can be obtained by the known formula (Makarov et al., 2014b).

$$\int_0^\infty \bar{Q}_{\sigma\tilde{\tau}}\cdot e^{-tx}\cdot dx = \frac{d\varphi_{\sigma t}}{dt} = r_{\sigma t} \tag{40}$$

by successive approximations.

The given formula (41) is the Laplace transform in which the delay spectrum $\bar{Q}_{\sigma\tilde{\tau}}$ plays the role of the original, and the delay kernel $r_{\sigma t}$ plays the role of the figure in terms of operator calculus. This dependence (40) is obtained on the basis of the properties of the Generalised Kelvin-Voigt model (Demidov et al., 2007a).

The application of the hyperbolic tangent function as the normalised delay function (36), leads to the following logarithmic delay kernel (Makarov et al., 2020).

$$D'_{\sigma t} = \frac{\partial D_{\sigma t}}{\partial\ln t} = (D_\infty - D_0)\cdot\bar{r}_{\sigma t} = \frac{A_\sigma}{4}\cdot(D_\infty - D_0)\cdot\left(1 - th^2(W_{\sigma t})\right) \tag{41}$$

The force-time argument (38) of the delay kernel (37) takes into account the current time factor and the characteristically average internal delay times. In the known approximation, the delay kernel (37) characterises the distribution of relaxing particles over their micromechanical delay times (Demidov et al., 2006b).

In order to obtain approximations of the normalised delay spectrum, the known recurrence formulas can be used (Demidov et al., 2006c) if $k = 1$

$$\bar{Q}_1 = \frac{\partial \varphi_{\sigma t}}{\partial \ln t} = \varphi'_{\sigma t} = \bar{r}_{\sigma t}\Big|_{t=\tilde{\tau}} \tag{42}$$

and if $k2$

$$\bar{Q}_k = \bar{Q}_{k-1} - \frac{1}{k-1} \cdot \frac{d\bar{Q}_{k-1}}{d \ln \tilde{\tau}}\Big|_{t=(k-1)\tilde{\tau}} \tag{43}$$

For calculating the values of the derivatives $\bar{r}_{\sigma t} = \frac{\partial \varphi_{\sigma t}}{\partial \ln t}, \ldots, \frac{\partial^k \varphi_{\sigma t}}{\partial \ln t^k}, \ldots$, where for the delay function $\varphi_{\sigma t} = \varphi$ the hyperbolic tangent is chosen (36) and $W_{\sigma t} = W$ is the structure-force-time argument-functional (38), we obtain

$$\varphi_{\sigma t} = \frac{1}{2} \cdot \left(1 + th\left(\frac{A_\sigma}{2} \cdot \ln\left(\frac{t}{\tau_\sigma}\right)\right)\right) \tag{44}$$

$$\begin{aligned} \varphi'_{\sigma t} = \bar{r}_{\sigma t} &= \frac{\partial \varphi_{\sigma t}}{\partial (\ln t)} = \frac{A_\sigma}{4} \cdot \frac{1}{ch^2(W_{\sigma t})} = \\ &= \frac{A_\sigma}{4} \cdot \left(1 - th^2(W_{\sigma t})\right) = A_\sigma \cdot \varphi_{\sigma t} \cdot (1 - \varphi_{\sigma t}) \end{aligned} \tag{45}$$

$$\varphi''_{\sigma t} = \frac{\partial^2 \varphi_{\sigma t}}{\partial (\ln t)^2} = A_\sigma^2 \cdot \varphi_{\sigma t} \cdot (1 - \varphi_{\sigma t}) \cdot (1 - 2 \cdot \varphi_{\sigma t}) \tag{46}$$

$$\varphi'''_{\sigma t} = \frac{\partial^3 \varphi_{\sigma t}}{\partial (\ln t)^3} = A_\sigma^3 \cdot \varphi_{\sigma t} \cdot (1 - \varphi_{\sigma t}) \cdot \left(1 - 6 \cdot \varphi_{\sigma t} + 6 \cdot \varphi_{\sigma t}^2\right) \tag{47}$$

$$\begin{aligned} \varphi^{\iota v}_{\sigma t} = \frac{\partial^4 \varphi_{\sigma t}}{\partial (\ln t)^4} &= A_\sigma^4 \cdot \varphi_{\sigma t} \cdot (1 - \varphi_{\sigma t}) \times \\ &\times \left(1 - 14 \cdot \varphi_{\sigma t} + 36 \cdot \varphi_{\sigma t}^2 - 24 \cdot \varphi_{\sigma t}^3\right) \end{aligned} \tag{48}$$

$$\begin{aligned} \varphi^{v}_{\sigma t} = \frac{\partial^5 \varphi_{\sigma t}}{\partial (\ln t)^5} &= A_\sigma^5 \cdot \varphi_{\sigma t} \cdot (1 - \varphi_{\sigma t}) \times \\ &\times \left(1 - 30 \cdot \varphi_{\sigma t} + 150 \cdot \varphi_{\sigma t}^2 - 240 \cdot \varphi_{\sigma t}^3 + 120 \cdot \varphi_{\sigma t}^4\right) \end{aligned} \tag{49}$$

$$\begin{aligned} \varphi^{v\iota}_{\sigma t} = \frac{\partial^6 \varphi_{\sigma t}}{\partial (\ln t)^6} &= A_\sigma^6 \cdot \varphi_{\sigma t} \cdot (1 - \varphi_{\sigma t}) \cdot (1 - 62 \cdot \varphi_{\sigma t} + \\ &+ 510 \cdot \varphi_{\sigma t}^2 - 1560 \cdot \varphi_{\sigma t}^3 + 1800 \cdot \varphi_{\sigma t}^4 - 720 \cdot \varphi_{\sigma t}^5) \end{aligned} \tag{50}$$

$$\begin{aligned} \varphi^{v\iota\iota}_{\sigma t} = \frac{\partial^7 \varphi_{\sigma t}}{\partial (\ln t)^7} &= A_\sigma^6 \cdot \varphi_{\sigma t} \cdot (1 - \varphi_{\sigma t}) \cdot \left(1 - 126 \cdot \varphi_{\sigma t} + 1716 \cdot \varphi_{\sigma t}^2 - \right. \\ &\left. - 8280 \cdot \varphi_{\sigma t}^3 + 16800 \cdot \varphi_{\sigma t}^4 - 15120 \cdot \varphi_{\sigma t}^5 + 5040 \cdot \varphi_{\sigma t}^6\right) \end{aligned} \tag{51}$$

and using the recurrence formulas (42), (43), that in expanded form are given by

$$\bar{Q}_1 = \frac{\partial \varphi}{\partial \ln t} = \varphi' = \overline{r_{\sigma t}}\Big|_{t=\tilde{\tau}} \tag{52}$$

$$\bar{Q}_2 = \frac{\partial \varphi}{\partial \ln t} - \frac{\partial^2 \varphi}{\partial \ln t^2} = \varphi' - \varphi''\Big|_{t=\tilde{\tau}} \tag{53}$$

$$\bar{Q}_3 = \varphi' - \frac{3}{2}\varphi'' + \frac{1}{2}\varphi'''\Big|_{t=2\tilde{\tau}} \tag{54}$$

$$\bar{Q}_4 = \varphi' - \frac{11}{6}\varphi'' + \varphi''' - \frac{1}{6}\varphi^{IV}\Big|_{t=3\tilde{\tau}} \tag{55}$$

$$\bar{Q}_5 = \varphi' - \frac{25}{12}\varphi'' + \frac{35}{24}\varphi''' - \frac{5}{12}\varphi^{IV} + \frac{1}{24}\varphi^{V}\Big|_{t=4\tilde{\tau}} \tag{56}$$

$$\bar{Q}_6 = \varphi' - \frac{137}{60}\varphi'' + \frac{15}{8}\varphi''' - \frac{17}{24}\varphi^{IV} + \frac{3}{24}\varphi^{V} - \frac{1}{120}\varphi^{VI}\Big|_{t=5\tilde{\tau}} \tag{57}$$

$$\bar{Q}_7 = \varphi' - \frac{49}{20}\varphi'' + \frac{203}{90}\varphi''' - \frac{49}{48}\varphi^{IV} + \frac{35}{144}\varphi^{V} - \frac{7}{240}\varphi^{VI} + \frac{1}{720}\varphi^{VII}\Big|_{t=6\tilde{\tau}} \tag{58}$$

we obtain expressions for approximations of the normalised delay spectrum

$$\bar{Q}_1 = \frac{\partial \varphi_{\sigma t}}{\partial(\ln t)}\Big|_{t=\tilde{\tau}} = \varphi'_{\sigma t}|_{t=\tilde{\tau}} = A_\sigma \cdot \varphi_{\sigma t} \cdot (1 - \varphi_{\sigma t})\Big|_{t=\tilde{\tau}} \tag{59}$$

$$\bar{Q}_2 = \varphi'_{\sigma t} - \varphi''_{\sigma t}|_{t=\tilde{\tau}} = A_\sigma \cdot \varphi_{\sigma t} \cdot (1 - \varphi_{\sigma t}) \cdot (1 - A_\sigma(1 - 2 \cdot \varphi_{\sigma t}))\big|_{t=\tilde{\tau}} \tag{60}$$

$$\begin{aligned} \bar{Q}_3 &= \varphi'_{\sigma t} - \frac{3}{2}\varphi''_{\sigma t} + \frac{1}{2}\varphi'''_{\sigma t}\Big|_{t=2\tilde{\tau}} = A_\sigma \cdot \varphi_{\sigma t} \cdot (1 - \varphi_{\sigma t}) \times \\ &\times \left(1 - \frac{3}{2} \cdot A_\sigma \cdot (1 - 2 \cdot \varphi_{\sigma t}) + \frac{1}{2} \cdot A_\sigma^2 \cdot \left(1 - 6 \cdot \varphi_{\sigma t} + 6 \cdot \varphi_{\sigma t}^2\right)\right)\Big|_{t=2\tilde{\tau}} \end{aligned} \tag{61}$$

$$\begin{aligned} \bar{Q}_4 &= \varphi'_{\sigma t} - \frac{11}{6}\varphi''_{\sigma t} + \varphi'''_{\sigma t} - \frac{1}{6}\varphi''''_{\sigma t}\Big|_{t=3\tilde{\tau}} = A_\sigma \cdot \varphi_{\sigma t} \cdot (1 - \varphi_{\sigma t}) \times \\ &\times \left(1 - \frac{11}{6} \cdot A_\sigma \cdot (1 - 2 \cdot \varphi_{\sigma t}) + A_\sigma^2 \cdot \left(1 - 6 \cdot \varphi_{\sigma t} + 6 \cdot \varphi_{\sigma t}^2\right) - \right. \\ &\left. - \frac{1}{6} \cdot A_\sigma^3 \cdot \left(1 - 14 \cdot \varphi_{\sigma t} + 36 \cdot \varphi_{\sigma t}^2 - 24 \cdot \varphi_{\sigma t}^3\right)\right)\Big|_{t=3\tilde{\tau}} \end{aligned} \tag{62}$$

$$\begin{aligned} \bar{Q}_5 &= \varphi'_{\sigma t} - \frac{25}{12}\varphi''_{\sigma t} + \frac{35}{24}\varphi'''_{\sigma t} - \frac{5}{12}\varphi''''_{\sigma t} + \frac{1}{24}\varphi'''''_{\sigma t}\Big|_{t=4\tilde{\tau}} = \\ &= A_\sigma \cdot \varphi_{\sigma t} \cdot (1 - \varphi_{\sigma t}) \cdot \left(1 - \frac{25}{12} \cdot A_\sigma \cdot (1 - 2 \cdot \varphi_{\sigma t}) + \frac{35}{24} \cdot A_\sigma^2 \times \right. \\ &\times \left(1 - 6 \cdot \varphi_{\sigma t} + 6 \cdot \varphi_{\sigma t}^2\right) - \frac{5}{12} \cdot A_\sigma^3 \cdot \left(1 - 14 \cdot \varphi_{\sigma t} + 36 \cdot \varphi_{\sigma t}^2 - 24 \cdot \varphi_{\sigma t}^3\right) + \\ &\left. + \frac{1}{24} \cdot A_\sigma^4 \cdot \left(1 - 30 \cdot \varphi_{\sigma t} + 150 \cdot \varphi_{\sigma t}^2 - 240 \cdot \varphi_{\sigma t}^3 + 120 \cdot \varphi_{\sigma t}^4\right)\right)\Big|_{t=4\tilde{\tau}} \end{aligned} \tag{63}$$

$$\bar{Q}_6 = \varphi'_{\sigma t} - \frac{137}{60}\varphi''_{\sigma t} + \frac{15}{8}\varphi'''_{\sigma t} - \frac{17}{24}\varphi^{iv}_{\sigma t} + \frac{1}{8}\varphi^{v}_{\sigma t} - \frac{1}{120}\varphi^{vi}_{\sigma t}\Big|_{t=5\bar{\tau}} =$$
$$\times\left(1 - 62\cdot\varphi_{\sigma t} + 510\cdot\varphi^2_{\sigma t} - 1560\cdot\varphi^3_{\sigma t} + 1800\cdot\varphi^4_{\sigma t} - 720\cdot\varphi^5_{\sigma t}\right)\Big)\Big|_{t=5\bar{\tau}}$$
$$= A_\sigma\cdot\varphi_{\sigma t}\cdot(1-\varphi_{\sigma t})\cdot\left(1 - \frac{137}{60}\cdot A_\sigma\cdot(1-2\cdot\varphi_{\sigma t}) + \frac{15}{8}\cdot A^2_\sigma\times\right. \quad (64)$$
$$\times\left(1 - 6\cdot\varphi_{\sigma t} + 6\cdot\varphi^2_{\sigma t}\right) - \frac{17}{24}\cdot A^3_\sigma\cdot\left(1 - 14\cdot\varphi_{\sigma t} + 36\cdot\varphi^2_{\sigma t} - 24\cdot\varphi^3_{\sigma t}\right) +$$
$$+\frac{1}{8}\cdot A^4_\sigma\cdot\left(1 - 30\cdot\varphi_{\sigma t} + 150\cdot\varphi^2_{\sigma t} - 240\cdot\varphi^3_{\sigma t} + 120\cdot\varphi^4_{\sigma t}\right) - \frac{1}{120}\cdot A^5_\sigma\times$$

$$\bar{Q}_7 = \varphi'_{\sigma t} - \frac{49}{20}\varphi''_{\sigma t} + \frac{203}{90}\varphi'''_{\sigma t} - \frac{49}{48}\varphi^{iv}_{\sigma t} + \frac{35}{144}\varphi^{v}_{\sigma t} - \frac{7}{240}\varphi^{vi}_{\sigma t} +$$
$$+\frac{1}{720}\varphi^{vii}_{\sigma t}\Big|_{t=6\bar{\tau}} = A_\sigma\cdot\varphi_{\sigma t}\cdot(1-\varphi_{\sigma t})\cdot\left(1 - \frac{49}{20}\cdot A_\sigma\cdot(1-2\cdot\varphi_{\sigma t}) +\right.$$
$$+\frac{203}{90}\cdot A^2_\sigma\cdot\left(1 - 6\cdot\varphi_{\sigma t} + 6\cdot\varphi^2_{\sigma t}\right) - \frac{49}{48}\cdot A^3_\sigma\cdot\left(1 - 14\cdot\varphi_{\sigma t} + 36\cdot\varphi^2_{\sigma t} -\right. \quad (65)$$
$$\left.-24\cdot\varphi^3_{\sigma t}\right) + \frac{35}{144}\cdot A^4_\sigma\cdot\left(1 - 30\cdot\varphi_{\sigma t} + 150\cdot\varphi^2_{\sigma t} - 240\cdot\varphi^3_{\sigma t} + 120\cdot\varphi^4_{\sigma t}\right) -$$
$$-\frac{7}{240}\cdot A^5_\sigma\cdot\left(1 - 62\cdot\varphi_{\sigma t} + 510\cdot\varphi^2_{\sigma t} - 1560\cdot\varphi^3_{\sigma t} +\right.$$
$$\left.+1800\cdot\varphi^4_{\sigma t} - 720\cdot\varphi^5_{\sigma t}\right) + \frac{1}{720}\cdot A^6_\sigma\cdot\left(1 - 126\cdot\varphi_{\sigma t} + 1760\cdot\varphi^2_{\sigma t} -\right.$$
$$\left.-8280\cdot\varphi^3_{\sigma t} + 16800\cdot\varphi^4_{\sigma t} - 15120\cdot\varphi^5_{\sigma t} + 5040\cdot\varphi^6_{\sigma t}\right)\Big)\Big|_{t=6\bar{\tau}}$$

The obtained results (59) – (65) can be represented by a single formula (Demidov et al., 2006d).

$$\bar{Q}_k = \bar{r}_{\sigma t}\cdot\sum_{i=1}^{k}\left(A^{i-1}_\sigma\cdot P_{k\,i}(\varphi_{\sigma t})\right)\Big|_{t=(k-1)\bar{\tau}} \quad (66)$$

where $P_{k\,i}(\varphi_{\sigma t})\leftarrow$ polynomials of a degree $i-1$ from $\varphi_{\sigma t}$. The type of the polynomials $P_{k\,i}(\varphi_{\sigma t})$ is shown in Table 2.

Therefore, the delay spectrum obtained on the basis of the mathematical model of the creep process, using the hyperbolic tangent (36) as the normalised delay function is completely determined by the structural coefficient A_σ, depending on a polymer material and the type of the polynomials $P_{k\,i}(\varphi_{\sigma t})$ that do not depend on a polymer material but are the characteristics of the mathematical model itself (Demidov et al., 2007b).

From the analytical form of the delay spectrum approximations $\bar{Q}_k$, it is evident that these approximations converge rather quickly to their limiting value $\bar{Q}$which characterises the stability of the chosen mathematical model of the creep process based on the hyperbolic tangent (36). This means that, with a small permissible error, as the relaxation spectrum its first approximation can be accepted, which is given by (Stalevich et al., 2003)

$$\overline{\bar{Q}}_1 = A_\sigma\cdot\varphi_{\sigma t}\cdot(1-\varphi_{\sigma t})\big|_{t=\bar{\tau}} \quad (67)$$

and depends only on the structural coefficient A_σ and on the delay function $\varphi_{\sigma t}$ in the form of the hyperbolic tangent (36).

Taking into account that the approximations of the spectrum of delay times $\bar{Q}_{\sigma\bar{\tau}}$ are obtained by the logarithmic time scale derivatives of the normalised delay function (36), and knowing the type of the delay spectrum the inverse problem can be solved. It is possible to

Table 2. The type of polynomials $P_{ki}(\varphi_{\sigma t})$, included in the formulas for approximations of the relaxation spectra of polymer materials.

i\k	1	2	3	4	5
1	1	1	1	1	1
2	-	$2\varphi - 1$	$3\varphi - \frac{3}{2}$	$\frac{11}{3}\varphi - \frac{11}{6}$	$\frac{25}{6}\varphi - \frac{25}{12}$
3	-	-	$3\varphi^2 - 3\varphi + \frac{1}{2}$	$6\varphi^2 - 6\varphi + 1$	$\frac{35}{4}\varphi^2 - \frac{35}{4}\varphi + \frac{35}{24}$
4	-	-	-	$4\varphi^3 - 6\varphi^2 + \frac{7}{3}\varphi - \frac{1}{6}$	$10\varphi^3 - 15\varphi^2 + \frac{35}{6}\varphi - \frac{5}{12}$
5	-	-	-	-	$5\varphi^4 - 10\varphi^3 + \frac{25}{4}\varphi^2 - \frac{5}{4}\varphi + \frac{1}{24}$

i\k	6	7
1	1	1
2	$\frac{137}{30}\varphi - \frac{137}{60}$	$\frac{49}{10}\varphi - \frac{49}{20}$
3	$\frac{45}{4}\varphi^2 - \frac{45}{4}\varphi + \frac{15}{8}$	$\frac{203}{15}\varphi^2 - \frac{203}{15}\varphi + \frac{203}{90}$
4	$17\varphi^3 - \frac{51}{2}\varphi^2 + \frac{119}{12}\varphi - \frac{17}{24}$	$\frac{49}{2}\varphi^3 - \frac{147}{4}\varphi^2 + \frac{343}{24}\varphi - \frac{49}{48}$
5	$15\varphi^4 - 30\varphi^3 + \frac{75}{4}\varphi^2 - \frac{15}{4}\varphi + \frac{1}{8}$	$\frac{175}{6}\varphi^4 - \frac{175}{3}\varphi^3 + \frac{875}{24}\varphi^2 - \frac{175}{24}\varphi + \frac{35}{144}$
6	$6\varphi^5 - 15\varphi^4 + 13\varphi^3 - \frac{17}{4}\varphi^2 + \frac{31}{60}\varphi - \frac{1}{120}$	$21\varphi^5 - \frac{105}{2}\varphi^4 + \frac{91}{2}\varphi^3 - \frac{119}{8}\varphi^2 + \frac{217}{120}\varphi - \frac{7}{240}$
7	-	$7\varphi^6 - 21\varphi^5 + \frac{70}{3}\varphi^4 - \frac{23}{2}\varphi^3 + \frac{110}{45}\varphi^2 - \frac{31}{180}\varphi + \frac{1}{720}$

obtain the corresponding normalised relaxation function by integrating. That is the basis of the mathematical model of viscoelastic properties (Makarov 2002).

The example of the delay spectrum of a polyester thread 83 tex. is shown in Figure 5. And the corresponding spectrum of the delay times of a polyester fabric made from polyester threads 83 tex. is shown in Figure 6.

Analysing the graphs of the delay times spectra of a polyester thread 83 tex. and polyester fabric made of polyester threads 83 tex., it can be noted that the intensity parameter corresponds to a polyester thread $A_\sigma = 0,30$, while in a polyester fabric it is much higher $A_\sigma = 1,45$ which leads to a more pronounced shape of the relaxation spectrum curve (Figure 5., Figure 6.)

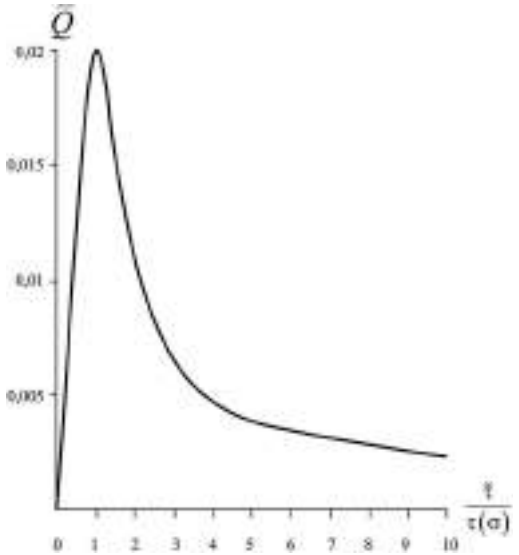

Figure 5. The graph of the spectrum of the delay times of a polyester thread 83 tex., $T = 40^\circ C$.

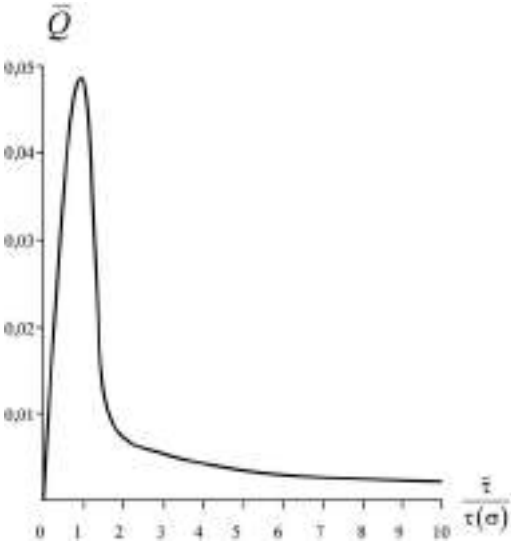

Figure 6. The graph of the spectrum of the delay times of polyester fabric made from polyester threads 83 tex., $T = 40^{\circ}C$.

It should be noted that the modified logarithmic time scale contains the force-time function

$$\ln\frac{t}{\tau_\sigma} = \ln\frac{t}{t_1} + \ln\frac{t_1}{\tau_\sigma} = \ln\frac{t}{t_1} + f_{\sigma_1\sigma} \tag{68}$$

reflecting the force-time analogy. Due to this time modification, the obtained delay spectra are generalised, that means, they extend to the entire initial range of non-destructive deformation (Stalevich et al., 2002a).

4 THE INTERRELATION OF VISCOELASTIC PARAMETERS-CHARACTERISTICS AND THE SPECTRA OF RELAXATION AND DELAY

As it is obvious from the previous study (2 and 3), the spectra of relaxation times and delay times are completely determined by the tasks of the mathematical model of relaxation and the mathematical model of creep, respectively, as well as the values of the intensity parameters A_ε and A_σ of these processes.

The approximations of the spectra of relaxation and delay times converge rather quickly to their limiting values. Therefore, according to its physical meaning, the normalised relaxation function is obtained by integrating the relaxation spectrum which characterises the distribution of particles over relaxation times and is completely determined by the average value of the relaxation times and the value of the structural coefficient A_ε. Similar results were achieved by obtaining the delay spectrum from the measured creep processes. If the preference is given to the average relaxation time τ_ε, depending on the deformation ε and the relaxation spectrum, this physical approach to nonlinear hereditary viscoelasticity can be called geometric (Stalevich et al., 2002b). If the average delay time τ_σ and the spectrum of the delay $\bar{Q}_{\sigma\tilde{\tau}}$ are taken as a basis, i.e. the distribution of the number of particles over the delay time, then this approach can be called the force one (Stalevich et al., 2000).

For complex deformation modes, these approaches correspond to equations of the hereditary type written in a logarithmic time scale as (Makarov et al., 2014c)

$$\sigma_t = E_o \cdot \varepsilon_t + \int_{-\infty}^{\ln t} \varepsilon_{t-s} \cdot \frac{\partial E_{\varepsilon s}}{\partial \ln s} \cdot d \ln s \tag{69}$$

$$\varepsilon_t = E_o^{-1} \cdot \sigma_t + \int_{-\infty}^{\ln t} \sigma_{t-s} \cdot \frac{\partial D_{\sigma s}}{\partial \ln s} \cdot d \ln s \tag{70}$$

The equation (69) describes a complex relaxation process when $\varepsilon \neq$const, and the equation (70) describes a complex creep process when $\sigma \neq$const.

The first approximations of the relaxation spectrum (Pereborovaet al., 2018e; Makarov et al., 2018b)

$$\frac{\partial \mathrm{E}_{\varepsilon s}}{\partial \ln s} \cong (E_o - E_\infty) \bar{H}_{\varepsilon \tilde{\tau}}|_{\tilde{\tau}=s} \tag{71}$$

$$\frac{\partial \mathrm{D}_{\sigma s}}{\partial \ln s} \cong \left(E_\infty^{-1} - E_o^{-1}\right) \bar{Q}_{\sigma \tilde{\tau}}|_{\tilde{\tau}=s} \tag{72}$$

characterise the spectral meaning of the equations kernels (69) and (70) and, as a result, the preferred type of notation (69) and (70) for practical analysis and calculations. For example, analysis or calculation of the stress-strain diagram by the formula (69) and the recovery deformation process by the formula (70) (Makarov et al., 2015c).

The physical validity of using the equations of state in the form (69) and (70) is also confirmed by the observed proportionality between the logarithm of the statistical relaxation or delay time and the activation energy according to the classical Arrhenius-Boltzmann formula (Demidov et al., 2007c)

$$U_\sigma = RT \cdot \left(\ln \frac{t_1}{\tau_0} - \ln \frac{t_1}{\tau_\sigma} \right) \tag{73}$$

$$U_\varepsilon = RT \cdot \left(\ln \frac{t_1}{\tau_0} - \ln \frac{t_1}{\tau_\varepsilon} \right) \tag{74}$$

where τ_0 - the parameter that has the meaning of the duration of the elementary rearrangement

of 'relaxing' particles of the material; $t_1 = 1$ minutes; $\ln \frac{t_1}{\tau_\sigma} = f_{\sigma_1 \sigma}$ - force function

where τ_σ- delay time; $\ln \frac{t_1}{\tau_\varepsilon} = f_{\varepsilon_1 \varepsilon}$ - deformation function where τ_ε - relaxation time;

T - temperature $T^\circ K$; $R = kA$ where k is the Boltzmann constant, A - the Avogadro number;

U_σ - activation energy as a function of stress; U_ε - activation energy as a function of deformation (Romashev et al., 2018).

This proportionality and equality of the initial values of the activation energies correspond to the adequacy of the equations (69) and (70), therefore, to the considered spectra in certain conditions (Blinov et al., 2018). The operability of the equations (69) and (70) means that the considered spectra of the distribution of particles over the relaxation or delay times reflects the nonlinear hereditary viscoelasticity of the considered polymer materials (Krasnyi et al., 2020).

5 CONCLUSION

The research showed that the relaxation spectra of polymeric materials are with satisfactory accuracy characterised by their first approximations which are the relaxation kernels, and the subsequent approximations quickly converge to the exact values of the spectra.

The same can be said about the delay spectra of polymeric materials which are also with satisfactory accuracy characterised by their first approximations, that are the delay kernels, and the subsequent approximations quickly converge to the exact values of the spectra.

The solution to the problem of analytical relationship between the nonlinear hereditary relaxation kernel and the deformation-time relaxation spectrum, as well as between the nonlinear hereditary creep kernel and the force-time creep spectrum, was substantiated by plotting the relaxation function and the delay function in the form of the hyperbolic tangent (2) and (36).

The features of the analysed polymeric materials, from the point of view of the considered mathematical models of viscoelasticity and their properties, include the fact that the relaxation kernel as a function of the logarithm almost coincides with the relaxation spectrum in a similar invariant form with reference to the deformation value, and the delay kernel as a function of time coincides with the delay spectrum in an invariant form with reference to the stress value.

It was found that the relaxation and delay spectra are completely determined by the average value of the relaxation and delay times, and the form of the corresponding curves is determined by the value of the structural coefficients A_ε and A_σ characterising the intensity of relaxation and creep processes.

According to the physical meaning, the normalised relaxation function and the delay function are obtained by integrating the relaxation spectrum and the delay spectrum, respectively.

The problems of determining the types of the relaxation spectra and delay spectra were reduced to obtaining the coefficients A_ε and A_σ depending on the structure of polymeric materials, the values of which can be found by express processing of the corresponding experimental sets of relaxation and delay. Therefore, it can be concluded that the relaxation and delay spectra are obtained by experimental data processing.

It should be mentioned that the relaxation and delay spectra are with satisfactory accuracy characterised by their first approximations which are the relaxation kernel and the delay kernel, and the subsequent approximations quickly converge to the limiting values of the spectra.

FUTURE RESEARCH AND ACKNOWLEDGEMENTS

The study was funded within the framework of the state assignment of the Ministry of Science and Higher Education of the Russian Federation, Project No. FSEZ-2020-0005.

REFERENCES

Blinov, P., Dvoynikov V., (2018) Rheological and Filtration Parameters of the Polymer Salt Drilling Fluids Based on Xanthan Gum. *Journal of Engineering and Applied Sciences*, 13: 5661–5664. DOI: 10.36478/2018.5661.5664

Demidov, A.V., Makarov, A.G., Stalevich, A.M. (2006a) The criteria of optimal selection of mathematical model of textile materials viscoelasticity. *Izvestiya Vysshikh Uchebnykh Zavedenii, Seriya Teknologiya Tekstil'noi Promyshlennosti*, Vol. 293, No 5, pp. 21–25. eid=2-s2.0-34247548784

Demidov, A.V., Makarov, A.G., Stalevich, A.M., Petrova, L.N., Chelishev, A.M. (2006b) Research of changes of deformation properties of polyester threads depending on twist amount. *Izvestiya Vysshikh Uchebnykh Zavedenii, Seriya Teknologiya Tekstil'noi Promyshlennosti*, Vol. 292, No 4, pp. 9–13. eid=2-s2.0-33845499474

Demidov, A.V., Makarov, A.G., Stalevich, A.M. (2006c) Methods of computer analysis of viscoelasticity of technical materials. *Izvestiya Vysshikh Uchebnykh Zavedenii, Seriya Teknologiya Tekstil'noi Promyshlennosti*, Vol. 291, No 3, pp. 13–17. eid=2-s2.0-37849188658

Demidov, A.V., Makarov, A.G., Stalevich, A.M. (2006d) Definition of the mechanical characteristics of textile stuffs at variable temperature. *Izvestiya Vysshikh Uchebnykh Zavedenii, Seriya Teknologiya Tekstil'noi Promyshlennosti*, Vol. 294, No 6, pp. 15–18. eid=2-s2.0-34250009041

Demidov, A.V., Makarov, A.G., Stalevich, A.M. (2007a) Definition of the computer forecasting trends of deformation properties of textile stuffs. *Izvestiya Vysshikh Uchebnykh Zavedenii, Seriya Teknologiya Tekstil'noi Promyshlennosti*, Vol. 297, No 2, pp. 14–17. eid=2-s2.0-38849203122

Demidov, A.V., Makarov, A.G., Stalevich, A.M. (2007b) Predicting the nonlinear hereditary viscoelasticity of polymers. *Journal of Applied Mechanics and Technical Physics*, Vol. 48, No 6, pp. 897–904. DOI: 10.1007/s10808-007-0114-8

Demidov, A.V., Makarov, A.G., Stalevich, A.M. (2007c) System analysis of viscoelasticity of textile stuffs. *Izvestiya Vysshikh Uchebnykh Zavedenii, Seriya Teknologiya Tekstil'noi Promyshlennosti*, Vol. 298, No 3, pp. 11–14. eid=2-s2.0-34648822922

Demidov, A.V., Makarov, A.G., Stalevich, A.M. (2009) A version of modeling of nonlinear-hereditary viscoelasticity of polymer materials. *Mechanics of Solids*, Vol. 44, No 1, pp. 122–130. DOI: 10.3103/S0025654409010130

Demidov, A.V., Makarov, A.G., Pereborova, N.V., Egorova, M.A. (2017) Forecasting of deformation-relaxation properties of poly amide fabric used to make the canopy. *Izvestiya Vysshikh Uchebnykh Zavedenii, Seriya Teknologiya Tekstil'noi Promyshlennosti*, Vol. 367, No 1, pp. 250–258. eid=2-s2.0-85033239149

Egorov, I.M., Makarov, A.G., Pereborova,N.V., Kiselev, S.V. (2020) Development of methods of system analysis of viscoelastic-plastic properties of polymeric ropes of marine purpose. *Vestnik of Saint Petersburg State University of Technologies and Design. Series 4. Industrial Technologies*, No 1, pp. 65–74. DOI 10.46418/2619-0729_2020_1_8

Gorshkov, A.S., Makarov, A.G., Romanova, A.A., Rymkevich, P.P. (2013a) Modelling of directed polymers deformation processes based on the description of the kinetics of supramolecular structures separated by energy barriers. *Magazine of Civil Engineering*, Vol. 44, No 9, pp. 76-83+103-104. DOI: 10.5862/MCE.44.10

Krasnyi, V. A., Maksarov, V. V. and Ol't, Y. (2020) "The use of polymer composite materials in the friction nodes downhole oil pumps", *Journal of Mining Institute*, 211, p. 71. Available at: http://pmi.spmi.ru/index.php/pmi/article/view/5250 (Accessed: 19 August 2020).

Makarov, A.G. (2002) Determining the analytical correlation between the standardized nuclei of relaxation and creep in textile materials. *Izvestiya Vysshikh Uchebnykh Zavedenii, Seriya Teknologiya Tekstil'noi Promyshlennosti*, Vol. 266, No 2, pp. 13–17. eid=2-s2.0-0036931214

Makarov, A.G., Pereborova, N.V., Egorova, M.A., Wagner, V.I. (2014a) Modeling and forecasting viscoelastic properties of textile materials with a complex structure. *Izvestiya Vysshikh Uchebnykh Zavedenii, Seriya Teknologiya Tekstil'noi Promyshlennosti*, Vol. 354, No 6, pp. 120–124. eid=2-s2.0-84937439497

Makarov, A.G., Pereborova, N.V., Egorova, M.A., Wagner, M.A. (2014b) Ways of modeling deformation and relaxation properties of textile materials with a complex structure. *Izvestiya Vysshikh Uchebnykh Zavedenii, Seriya Teknologiya Tekstil'noi Promyshlennosti*, Vol. 351, No 3, pp. 110–115. eid=2-s2.0-84937410003

Makarov, A.G., Pereborova, N.V., Wagner, V.I., Rymkevich, P.P., Gorshkov, A.S. (2014c) The Basis of Spectral-Temporal Analysis of Relaxation and Deformation Properties of Polymeric Materials in Textile and Ligt Industry. *Izvestiya Vysshikh Uchebnykh Zavedenii, Seriya Teknologiya Legkoi Promyshlennosti*, Vol. 23, No 1. pp. 24–29.

Makarov, A.G., Slutsker, G.Y., Drobotun, N.V. (2015a) Creep and fracture kinetics of polymers. *Technical Physics*, Vol. 60, No 2, pp. 240–245. DOI: 10.1134/S1063784215020152

Makarov, A.G., Pereborova, N.V., Wagner, V.I., Vasileva, E.K. (2015b) Development of methodology for the comparative analysis of deformation and relaxation properties of aramid yarns and textile materials based on them. *Izvestiya Vysshikh Uchebnykh Zavedenii, Seriya Teknologiya Tekstil'noi Promyshlennosti*, Vol. 359, No 5, pp. 48–58. eid=2-s2.0-84971636036

Makarov, A.G., Demidov, A.V., Pereborova, N.V., Egorova, M.A. (2015c) Modeling and prediction of estimated relaxation and deformation properties of the polymer parachute line. *Izvestiya Vysshikh Uchebnykh Zavedenii, Seriya Teknologiya Tekstil'noi Promyshlennosti*, Vol. 360, No 6, pp. 194–205. eid=2-s2.0-84976560627

Makarov, A.G., Slutsker, G.Y., Gofman, I.V., Vasil'eva, V.V. (2016) Initial stage of stress relaxation in oriented polymers. *Physics of the Solid State*, Vol. 58, No 4, pp. 840–846. DOI: 10.1134/S1063783416040132

Makarov, A.G., Pereborova, N.V., Egorova, M.A., Egorov, I.M. (2017a) Quality analysis of deformation-relaxation properties of aramid cords mountain rescue appointments. *Izvestiya Vysshikh Uchebnykh Zavedenii, Seriya Teknologiya Tekstil'noi Promyshlennosti*, Vol. 368, No 2, pp. 309–313. eid=2-s2.0-85035207042

Makarov, A.G., Pereborova, N.V., Egorova, M.A., Egorov, I.M. (2017b) Mathematical modeling of deformation-relaxation processes polymeric materials in conditions of variable temperatures. *Izvestiya Vysshikh Uchebnykh Zavedenii, Seriya Teknologiya Tekstil'noi Promyshlennosti*, Vol. 370, No 4, pp. 287–292. eid=2-s2.0-85057142312

Makarov, A.G., Pereborova N.V., Kozlov A.A., Shvankin A.M. (2018a) Computer-Assisted Prediction and Qualitative Analysis for Polymer Parachute Cords *Fibre Chemistry*, Vol. 50, No. 3, pp. 239–242. DOI 10.1007/s10692-018-9968-1

Makarov, A.G., Pereborova, N.V., Vagner, V.I., Egorova, M.A., Klimova, N.S. (2018b) Spectral Analysis of Viscoelastic Creep of Geotextiles. *Fibrie Chemistry*, Vol. 50, No 4, pp. 378–382. DOI 10.1007/s10692-019-09993-4

Makarov, A.G., Busygin, K.N. (2020) System analysis of functional properties of special application aramid materials. *Vestnik of Saint Petersburg State University of Technologies and Design. Series 4. Industrial Technologies*, No 2, pp. 84–94. DOI: 10.46418/2619–0729_2020_2_10

Pereborova, N.V., Makarov, A.G., Egorova, M.A., Kozlov, A.A., Konovalov, A.S. (2018a) Methods of simulation and comparative analysis of shadow and deformation-reducing properties of aramide textile materials. *Izvestiya Vysshikh Uchebnykh Zavedenii, Seriya Teknologiya Tekstil'noi Promyshlennosti*, Vol. 375, No 3, pp. 253–257. eid=2-s2.0-85059766891

Pereborova, N.V., Makarov, A.G., Kozlov, A.A., Vasil'eva, E.K. (2018b) Development of Integral Optimality Criteria for Mathematical Modeling of Relaxation/Recovery Processes in Polymer Textile Materials. *Fibrie Chemistry*, Vol. 50, No 4, pp. 306–309. DOI 10.1007/s10692-019-09981-8

Pereborova, N.V., Makarov, A.G., Egorova, M.A., Klimova, N.S. (2018c) Methods of increasing the competitiveness of domestic aramid textile materials based on complex analysis of their functional properties. *Izvestiya Vysshikh Uchebnykh Zavedenii, Seriya Teknologiya Tekstil'noi Promyshlennosti*, Vol. 378, No 6, pp. 267–272. eid=2-s2.0-85072335464

Pereborova, N.V., Demidov, A.V., Makarov, A.G., Klimova, N.S., Vasileva, E.K. (2018d) Methods of mathematical modeling and qualitative analysis of relaxation-deformation processes of aramide textile materials. *Izvestiya Vysshikh Uchebnykh Zavedenii, Seriya Teknologiya Tekstil'noi Promyshlennosti*, Vol. 374, No 2, pp. 251–255. eid=2-s2.0-85056451197

Pereborova, N.V., Demidov, A.V., Makarov, A.G., Klimova, N.S. (2018e) Modeling of Deformation-Relaxation Processes of Aramid Textile Materials – the Foundation for Analyzing Their Operational Properties. *Fibre Chemistry*, Vol. 50, No. 2, pp. 104–107. DOI 10.1007/s10692-018-9941-z

Pereborova, N.V., Makarov, A.G., Vasil'eva, E.K., Shvankin, A.M., Egorov, I.M. (2019a) Mathematical Modeling and Computed Prediction of Viscoelastic Creep in Geotextile Nonwoven Fabrics. *Fibre Chemistry*, Vol. 50, No. 6, pp. 487–490. DOI 10.1007/s10692-019-10015-6

Pereborova, N.V., Makarov, A.G., Egorova, M.A., Kozlov, A.A. (2019b) Mathematical Modeling and Comparative Analysis of Deformation/Recovery Properties and Shrinkage of Aramid Textile Materials. *Fibre Chemistry*, Vol. 50, No 5, pp. 468–472. DOI 10.1007/s10692-019-10010-x

Pereborova, N.V., Makarov, A.G., Egorova, M.A., Klimova, N.S. (2019c) Improving the Competitiveness of Aramid Textile Materials Based on Mathematical Modeling and Analysis of Their Performance Properties. *Fibre Chemistry*, Vol. 50, No 6, pp. 569–572. DOI 10.1007/s10692-019-10030-7

Pereborova, N.V., Makarov, A.G., Shvankin, A.M., Egorova, M.A., Abramova, I.V. (2020a) Modeling and Qualitative Analysis of Creep Processes of Geotextile Nonwovens -A Foundation for Enhancing their Competitiveness. *Fibre Chemistry*, Vol. 51, No. 5, pp. 397–400. DOI 10.1007/s10692-020-10119-4

Pereborova, N.V., Makarov, A.G., Shvankin, A. M., Egorova, M. A., Korobovtseva, A.A. (2020b) Predicting Creep and Deformation and Recovery Processes of Geotextile Nonwovens. *Fibre Chemistry*, Vol. 51, No. 5, pp. 401–403. DOI 10.1007/s10692-020-10120-x

Pereborova, N.V., Makarov, A.G., Egorova, M.A., Egorov, I.M. (2020c) Methods of Modeling and Computer-Aided Prediction of Relaxation of Medical-Purpose Textile Elastomers. *Fibre Chemistry*, Vol. 51, No. 6, pp. 467–470. DOI 10.1007/s10692-020-10136-3

Pereborova, N.V., Makarov, A.G., Egorova, M.A., Egorov, I.M. (2020d) Methods modeling and Computer-Aided Prediction of Strain and Relaxation Processes of Medical-Purpose Textile Elastomers. *Fibre Chemistry*, Vol. 51, No. 6, pp. 471–474. DOI 10.1007/s10692-020-10137-2

Pereborova, N.V., Makarov, A.G., Kiselev, S.V., Egorov, I.M. (2020e) System analysis of relaxation processes of polymeric textile materials of special purpose. *Vestnik of Saint Petersburg State University of Technologies and Design. Series 4. Industrial Technologies*, Vol. 47, No 1, pp. 53–64. DOI 10.46418/2619-0729_2020_1_7

Pereborova, N.V., Wagner, V.I., Kiselev, S.V., Kozlov, A.A. (2020f) Computer forecasting of relaxation processes of polymeric textile materials. *Vestnik of Saint Petersburg State University of Technologies and Design. Series 4. Industrial Technologies*, No 1, pp. 89–100. DOI 10.46418/2619-0729_2020_1_12

Pereborova, N.V. (2020g) Application of criteria for qualitative evaluation of relaxation properties of polymeric textile materials for evaluation of their functionality. *Vestnik of Saint Petersburg State University of Technologies and Design. Series 4. Industrial Technologies*, No 1, pp. 101–110. DOI 10.46418/2619-0729_2020_1_13

Romashev, A.O., Aleksandrova, T.N., Aleksandrov, A.V. (2018) Modelling of the relaxation properties of petroleum-bitumen suspension. *Information*, No 20, Vol. 9, pp. 6595–6603

Rymkevich, P.P., Romanova, A.A., Golovina, V.V., Makarov, A.G. (2013) The energy barriers model for the physical description of the viscoelasticity of synthetic polymers: Application to the uniaxial orientational drawing of polyamide films. *Journal of Macromolecular Science, Part B: Physics*, Vol. 52, No 12, pp. 1829–1847. DOI: 10.1080/00222348.2013.808906

Stalevich, A.M., Makarov, A.G. (2000) Determining the inherent viscoelastic relaxation spectrum for synthetic filaments. *Izvestiya Vysshikh Uchebnykh Zavedenii, Seriya Teknologiya Tekstil'noi Promyshlennost*i, Vol. 255, No 3, pp. 8–12. eid=2-s2.0-0034436083

Stalevich, A.M., Makarov, A.G. (2002a) Forecasting the deformation recovery process and the reverse relaxation in polymer materials. *Izvestiya Vysshikh Uchebnykh Zavedenii, Seriya Teknologiya Tekstil'noi Promyshlennosti*, Vol. 267, No 3, pp. 10–13. eid=2-s2.0-0038128574

Stalevich, A.M., Makarov, A.G., Saidov, E.D. (2002b) Elastic components in the stress/strain curve for a synthetic fibre yarn. *Izvestiya Vysshikh Uchebnykh Zavedenii, Seriya Teknologiya Tekstil'noi Promyshlennosti*, Vol. 268, No 4-5, pp. 15–18. eid=2-s2.0-0037742684

Stalevich, A.M., Makarov, A.G., Saidov, E.D. (2003) Relaxation spectrometry of synthetic yarns. *Izvestiya Vysshikh Uchebnykh Zavedenii, Seriya Teknologiya Tekstil'noi Promyshlennosti*, Vol. 270, No 1, pp. 16–22. eid=2-s2.0-2642532049

Advances in Raw Material Industries for Sustainable Development Goals – Litvinenko (Ed)

Ecotoxicological assessment of underwater welding impact during the construction of marine pipelines

K.Y. Kirichenko, K.S. Pikula, A.M. Zakharenko & A.V. Gridasov
Far Eastern Federal University, Vladivostok, Russian Federation

S.G. Parshin
Peter the Great St. Petersburg Polytechnic University, Saint Petersburg, Russian Federation

S.A. Medvedev
Stock Company «Izumrud», Vladivostok, Russian Federation

I.A. Vakhniuk
Far Eastern Federal University, Vladivostok, Russian Federation

K.S. Golokhvast
Far Eastern Federal University, Vladivostok, Russian Federation
N.I. Vavilov All-Russian Institute of Plant Genetic Resources, Saint-Petersburg, Russian Federation
Pacific Geographical Institute FEB RAS, Vladivostok, Russian Federation

ABSTRACT: Underwater welding is commonly used in joining pipelines and in underwater construction. Harmful and hazardous compounds are added to many flux cored wires for underwater welding and cutting, which can have a negative impact on marine life. This study is the first attempt to determine the influence of underwater welding on marine organisms using a standard model for assessing the changes in the early development of embryos of the sea urchin *Scaphechinus mirabilis* during short-term cultivation with the postulated toxicant.

Particles emitted during underwater welding pose toxicological threat to marine ecosystems. This fact requires the development of regulatory documents in the field of environmental protection and the introduction of compensatory measures to reduce the impact on marine organisms.

1 INTRODUCTION

The construction of long-distance subsea oil and gas pipelines has become a trend in the development of networks of large corporations. To date, several major underwater projects have been completed or currently are under development worldwide, including the Russian Federation:

1. Nord Stream (1,224 km) and Nord Stream 2 (1,200 km) – gas pipelines between Russia and Germany running over the bottom of the Baltic Sea;
2. The Blue Stream (1,213 km) and the Turkish Stream (1,100 km) – gas pipelines between Russia and Turkey running over the bottom of the Black Sea;
3. The Langeled pipeline (1,200 km) connecting the Norwegian Ormen Lange natural gas field with the U.K. Easington Gas Terminal;
4. Dzhubga – Lazarevskoye – Sochi (166 km) – a system of gas pipelines for energy supply in Sochi.

Underwater welding is commonly used in joining of the pipelines and in underwater construction (Labanowski et al., 2008). Underwater welding was first demonstrated in 1932 by the Soviet engineer K.K. Khrenov (Khrenov & Livshiz,1934).

The compositions, electrodes and methods of this technology are being improved till this day (Han et al., 2020; Park & Moon, 2020). Commonly, various additives are introduced to the flux cored wire to improve the technology (Xing et al., 2020). For working in deep water, toxic materials, for instance, chromium oxides, metallic chromium, and potassium dichromate ($K_2Cr_2O_7$) are added. The introduction of dichromate, for example, reduces the ionization potential and improves the stability of arcing under water, as well as increases the mechanical properties of welded joints during the underwater welding (Grishanov & Pankov, 1994a; Yushchenko et al., 1995; Duo et al., 2014).

As is known, $K_2Cr_2O_7$ is a strong oxidizing agent with a pronounced genotoxic effect and it is used as a reference toxicant in aquatic toxicity testing (Kikuchi et al., 2017; Patlolla et al., 2009; Pikula et al., 2019). When welding, potassium dichromate, as well as oxidizing metallic chromium, form toxic chromium oxides in a gas-vapor bubbles. Metal fluorides (lithium and cobalt) are also added to the composition of flux cored wire and electrodes for underwater welding (Grishanov & Pankov, 1994b).

A flux cored wire for welding steels under water is known, which includes a powder mixture containing loparite concentrate, cadmium oxide and nickel. The wire improves the quality and corrosion resistance of weld joints, however, it contains cadmium oxide and radioactive thorium oxide ThO_2 (in loparite concentrate) (Grishanov & Pankov, 1994c). Barium peroxide (Wang et al., 2012) and potassium chlorate $KClO_3$ (Duo et al., 2015) are also among the components of flux cored wire for underwater arc cutting. In summary, many flux cored wires for underwater welding and cutting contain harmful and hazardous compounds that can have a negative effect on marine life.

Previously we have shown a dependence of aquatic toxicity of welding fume particles on the welding electrode type and the welding regime parameters using a microalgae growth-inhibition approach (Kirichenko et al., 2019). In this study, we assessed the environmental impact of the SEAWELD electrode (Arcair) used for underwater welding on early development of the sea urchin embryos *Scaphechinus mirabilis* during short-term cultivation.

2 MATERIALS AND METHODS

2.1 *Sample preparation*

The practical application of underwater welding is complicated by several factors, including poor visibility, which in turn makes it difficult to make butt joints as the welding path is easily lost. In this regard, during the experiment, a fillet weld of lap joint was performed, and the edges of plates were used as guides for the electrode.

As it known, water-cooled electrode covering melts slower than the core wire forming a "fingernail" at the end of the electrode, which, in turn, ensures the stability of gas bubble and arc burning. Therefore, the welding was done by supported electrode while moving the electrode along the weld line and touching the metal surface with the protruding edge of the "fingernail" at the end of electrode. We moved the electrode along the welding path without lateral oscillations and with the speed that provided the desired cross section of weld metal.

In the welding experiment, we used 5-mm thick metal plates from commercial quality carbon steel, Russian standard VSt3sp according to GOST 19903-74. Chemical composition of used steal represented in Table 1.

The welding was done in the lower position at direct-current straight polarity ($I_{welding}$ = 120 A) with the Arcair Sea-Weld electrodes (Victor Technologies, USA), 3.2 mm in diameter, 356 mm in length (1/8 "x14"). The electrode covering has three layers: iron oxide, aluminum, and plasticized vinyl (Figure 1).

Seawater for the experiment was taken in the Ajax Bay (Russky Island, Vladivostok) in 40-liter sterile containers. We filtered the collected water through 0.45 μm filters and poured it into a 160-liter glass aquarium (Figure 2).

Table 1. Chemical composition (%) of steel VSt3sp.

C	Si	Mn	Ni	S	P	Cr	Cu	As	Fe
0.14–0.22	0.12–0.3	0.4– 0.65	< 0.3	< 0.05	< 0.04	< 0.3	< 0.3	< 0.08	< 100

Figure 1. The structure of the Arcair Sea-Weld electrode; a – electrode core wire, b – iron oxide layer, c – aluminum covering, d – plasticized vinyl.

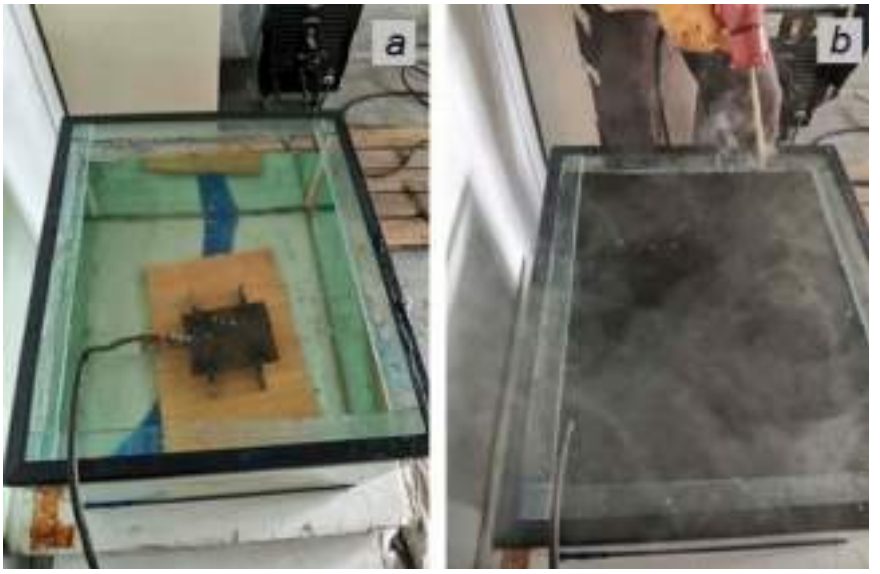

Figure 2. The experimental aquarium used for simulating underwater welding; a – before burning of an electrode, b – after burning of an electrode (60 sec).

We measured the particle size distribution of the welding fume generated above the aquarium using a TSI 9306 V2 particle counter (Aerotrack, USA) at time intervals of 15, 30, 45, and 60 seconds.

We collected sea water samples from the experimental aquarium at 15, 30, 45, and 60 seconds after the start of the underwater welding experiment. The particle size analysis of the obtained sea water samples was performed in the particle range of 1–700 μm using the Analysette 22 NanoTec plus laser particle sizer (Fritsch GmbH, Germany). Additionally, we carried out particle size analysis of seawater in the range of 100-900 nm by the CytoFLEX flow cytometer (Beckman Coulter, USA) using the data of forward scattering of violet laser (405 nm).

The experiments were carried out in the Department of Welding and in the Education and Scientific Center of Nanotechnology, School of Engineering of the Far Eastern Federal University.

2.2 *Aquatic toxicity assessment*

Aquatic toxicity of underwater welding suspensions was evaluated by standard early embryo growth toxicity test (Nacci et al., 1986) using the sea urchin *S. mirabilis* A. Agassiz, 1864

(Kroh and Mooi, 2015). Sea urchin embryos were incubated in 24-well plates at 17–17.5 °C, water salinity of 33.7 ‰, and pH of 8.18. The aliquot of embryonic cells in seawater was 1000 µl. We added the welding suspension, which was obtained after 60 seconds of simulating the underwater welding, in volumes of 1, 10, 100, 250, 500, and 1000 µl. In all cases, the volume of added liquid was brought to 1000 µl using seawater filtered by the method described above. Accordingly, at the maximum concentration, only welding suspension was added to the aliquot of sea urchin embryos, and seawater without welding suspension was used as a control.

We observed early changes in the development of sea urchin embryos using the Axio Observer A1 optical microscope (Carl Zeiss, Germany) for 48 hours. Control points were recorded after 2, 4, 6, 24, and 48 hours of exposure of the eggs and sperm of the sea urchin in the tested suspensions of underwater welding particles.

3 RESULTS AND DISCUSSION

One of the drawbacks of the model used is the small depth of the aquarium compared to the real underwater welding conditions. As a result, a certain amount of welding aerosol was emitted into the air, which obviously would remain in the water medium when welding at great depths. The particle size composition of the welding aerosol emitted into the air above the aquarium during the experiment presented in Table 2.

According to the data presented in Table 2, there was a significant increase in the concentration of particles with the diameter of 0.3 to 3 µm in the air above the underwater welding process. The concentration of 0.3 µm particles increased 100 times in 60 seconds after the start of the experiment compared to the control concentration. At the same time, the concentrations of 0.5 µm and 1 µm particles increased 500 times. Obviously, when welding at a depth, all these particles will remain in the water.

Even though a part of the welding aerosol was emitted into the air, most of the solid particles emitted during the underwater welding remained in sea water. The particle size distribution of the welding suspensions in the range of 1–700 µm represented in Table 3.

As we can see, seawater is an extremely heterogeneous and complex system. The laser diffraction method does not allow us to clearly verify the nano- and microparticles of welding suspension, therefore we additionally used flow cytometry to identify the particle sizes with higher precision. The particle size distribution of suspensions obtained using the CytoFLEX flow cytometer is shown in Figure 3.

Firstly, we can draw a preliminary conclusion about the necessity to create a combined precision method for measuring the dimensions, concentration and fractional ratio of welding aerosol particles in sea water. Since, to date, none of the methods can accurately determine both the concentration and dimensions of nanoparticles in sea water.

Table 2. Particle size composition of the aerosol emitted during the simulation of underwater welding.

Particle size, µm	Control (air before the experiment), particles in m^3	Welding aerosol during the experiment, particles in m^3			
		15 sec	30 sec	45 sec	60 sec
0.3	22880	90598	263575	720336	2302992
0.5	3406	16091	146790	488030	1750635
1	1365	7615	26060	100030	715639
3	376	2742	785	1541	54096
5	201	1467	366	568	9424
10	35	351	63	100	71

Table 3. Particle size composition of the welding aerosol suspension in sea water obtained using the Fritch laser particle sizer.

Particle size, μm	Control (sea water), % of particles	The distribution of solid particles in the welding suspension during the experiment, %			
		15 sec	30 sec	45 sec	60 sec
< 1	0.3	1.9	2.7	3.5	3.4
10	11.9	21.1	9.4	8.1	6.5
50	0.3	9.7	9.8	11.9	38.3
100	0	3.8	0.5	0.7	0.8
400	0.9	15.6	2.7	19.8	18
700	37	23.8	36.2	22.8	22.5
> 700	49.6	24.1	38.7	23.2	10.7

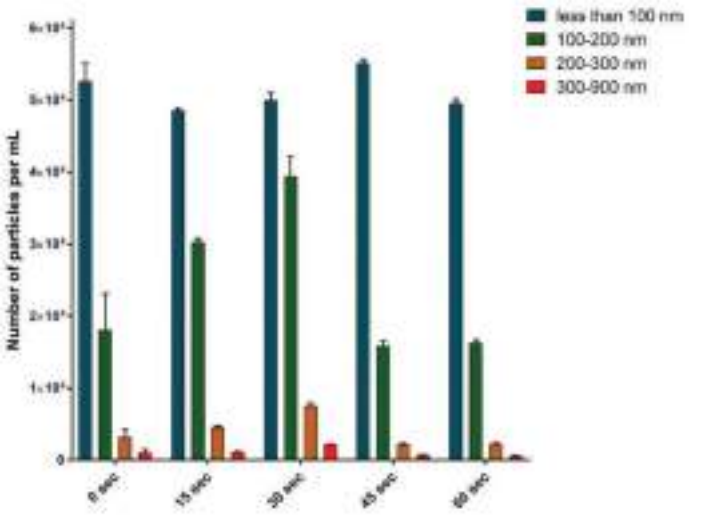

Figure 3. Particle size composition of the welding aerosol suspension in sea water obtained using the CytoFLEX flow cytometer.

Secondly, we can highlight the prevalence of 50 μm and 400 μm particles in the micron range (Table 3) and the intensive formation of the most toxic 100–200 nm particles (Engin et al., 2017) in the submicron range (Figure 3).

We assumed that underwater welding emission may be toxic to aquatic organisms, and we verified the assumption using the classic embryotoxicity test on sea urchin larvae. The data on the effect of the welding suspension on changes in the development and the viability of sea urchin embryos is presented in Figure 4.

The results demonstrate a linear increase in toxicity of the welding suspension for embryos of sea urchins *S. mirabilis*. We should note an intensive stimulation of development disorders of the embryos that does not lead to a significant increase in mortality up to 24 hours of exposure (Figure 4a–c). After 48 hours of exposure to the maximum concentration of the welding suspension, about a third of the cells died (Figure 4e). Visually, it can be seen in Figure 5.

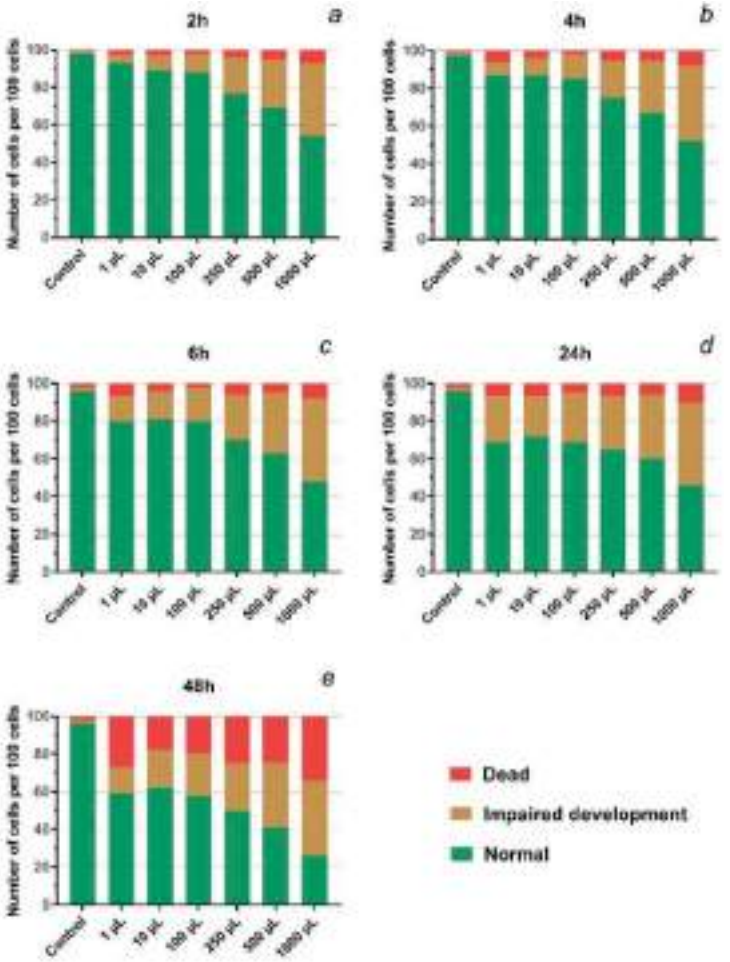

Figure 4. The changes in the development and viability of *S. mirabilis* embryos after the exposure to the welding suspension; a – 2-hours treatment, b – 4-hours treatment, c – 6-hours treatment, d – 24-hours treatment, e – 48-hours treatment.

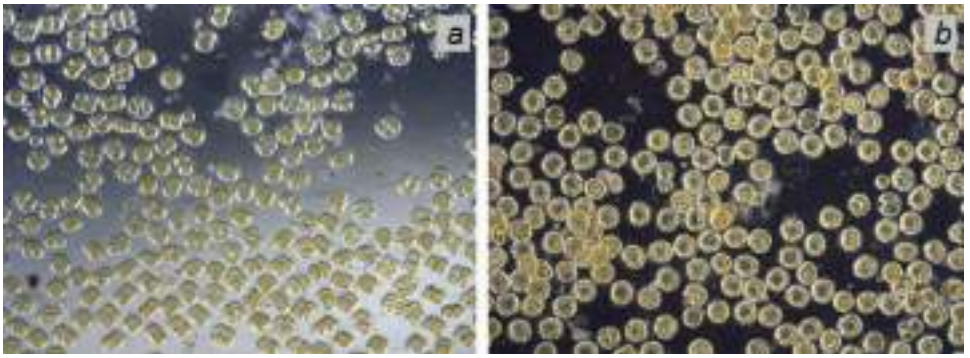

Figure 5. The effect of underwater welding suspension at the concentration of 1000 mg/L on the embryos of *S. mirabilis*; a –2-hours treatment, b – 48-hours treatment.

4 CONCLUSIONS

The results of this study enable us to state with confidence that underwater welding poses a serious threat to marine ecosystems. Given the growing volume of work on underwater pipelines, which are used for the transportation of natural resources, one should predict an increase of the negative impact on representatives of aquatic organisms. Therefore, this fact requires a timely response. The process of underwater welding needs to be further studied in order to develop ecological standards and effective measures that will ensure safety for the environment and humans.

ACKNOWLEDGEMENTS

The study was funded by RFBR, project number 19-05-50010, and by the grant from the President of the Russian Federation for young candidates of sciences (PhD) MK-2461.2019.5.

REFERENCES

Duo, L., Hongliang, L. & Jical, F. 2015. Chemical core cutting wire for underwater wet method electric arc cutting. *Patent* CN104858565 (A).

Duo, L., Ning, G., Yibo, L., Jical, F. & Xin, Y. 2014. Self-protection flux-cored wire for underwater wet-method welding. *Patent* CN104057214 (A).

Engin, A.B., Neagu, M., Nikitovic, D., Henrich-Noack, P., Docea, A.O., Shtilman, M.I. Golokhvast, K. S. & Tsatsakis, A.M. 2017. Mechanistic understanding of nanoparticles' interactions with extracellular matrix: the cell and immune system. *Particle and Fibre Toxicology* 14(1): 22. doi: 10.1186/s12989-017-0199-z

Grishanov, A.A. & Pankov V.I. 1994b. Flux cored wire for welding steels. *Patent of the Russian Federation* No. 2012469, B23K35/368 (In Russian).

Grishanov, A.A. & Pankov, V.I. 1994a. Flux cored wire for welding steels. *Patent of the Russian Federation* No. 2012471, B23K35/368 (In Russian).

Grishanov, A.A. & Pankov, V.I. 1994c. Flux cored wire for welding steels. *Patent of the Russian Federation* No. 2012470, B23K35/368 (In Russian).

Han, Y., Dong, S., Zhang, M., Jia, C., Zhang, M. & Wu, C. 2020. A novel underwater submerged-arc welding acquires sound quality joints for high strength marine steel. *Materials Letters* 261: 127075. doi:10.1016/j.matlet.2019.127075.

Khrenov, K.K. & Livshiz, M.L. 1934. Underwater electric arc welding. *Svarshchik* 6: 26–31. (In Russian).

Kikuchi, M., Syudo, A., Hukumori, M., Naito, C. & Sawai, J. 2017. Changes in aquatic toxicity of potassium dichromate as a function of water quality parameters. *Chemosphere* 170: 113–117. doi: 10.1016/j.chemosphere.2016.11.158.

Kirichenko, K., Zakharenko, A., Pikula, K., Chaika, V., Markina, Z., Orlova, T., Medvedev, S., Waissi, G., Kholodov, A., Tsatsakis, A. & Golokhvast, K. 2019. Dependence of welding fume particle toxicity on electrode type and current intensity assessed by microalgae growth inhibition test. *Environmental research* 179: 108818. doi: 10.1016/j.envres.2019.108818.

Kroh, A. & Mooi, R. 2015. The World Echinoidea Database. http://www.marinespecies.org/Echinoidea/.

Labanowski, J., Fydrych, D. & Rogalski, G. 2008. Underwater welding-a review. *Advances in Materials Sciences* 8(3): 11–22. doi: 10.2478/v10077-008-0040-3.

Nacci, D., Jackim, E. & Walsh, R. 1986. Comparative evaluation of three rapid marine toxicity tests: sea urchin early embryo growth test, sea urchin sperm cell toxicity test and Microtox. *Environmental Toxicology and Chemistry: An International Journal* 5(6): 521–525. doi: 10.1002/etc.5620050603.

Park, J. H., & Moon, H. S. 2020. Advanced Automatic Welding System for Offshore Pipeline System with Seam Tracking Function. *Applied Sciences* 10(1): 324. doi: 10.3390/app10010324.

Patlolla, A.K., Barnes, C., Hackett, D. & Tchounwou, P.B. 2009. Potassium dichromate induced cytotoxicity, genotoxicity and oxidative stress in human liver carcinoma (HepG2) cells. *International Journal of Environmental Research and Public Health* 6(2): 643–653. doi: 10.3390/ijerph6020643.

Pikula, K.S., Zakharenko, A.M., Chaika, V.V., Stratidakis, A.K., Kokkinakis, M., Waissi, G., Rakitskii, V.N., Sarigiannis, D.A., Hayes A.W., Coleman, M.D., Tsatsakis, A. & Golokhvast, K.S.,

2019. Toxicity bioassay of waste cooking oil-based biodiesel on marine microalgae. *Toxicology Reports* 6: 111–117. doi: 10.1016/j.toxrep.2018.12.007.

Wang J., Li W. & Zhu J. 2012. Flux-cored cutting wire for underwater wet-type arc cutting and preparation method thereof. *Patent* CN102554520 (A).

Xing, C., Jia, C., Han, Y., Dong, S., Yang, J. & Wu, C. 2020. Numerical Analysis of the Metal Transfer and Welding Arc Behaviors in Underwater Flux-cored Arc Welding. *International Journal of Heat and Mass Transfer* 153, 119570. doi: 10.1016/j.ijheatmasstransfer.2020.119570.

Yushchenko, K.A., Fadeeva, G.V., Kakhovsky, Yu.N. & Savchenko V.S. 1995. Composition of cored wire. *Patent of the Russian Federation* No. 1605451, bull. No. 3. (In Russian).

Advances in Raw Material Industries for Sustainable Development Goals – Litvinenko (Ed)
© 2021 Taylor & Francis Group, London, ISBN 978-0-367-75881-3

Assessment of coal dust particles influence on marine mollusk *Modiolus modiolus*

K.Y. Kirichenko, K.S. Pikula, V.V. Chaika, A.M. Zakharenko, A.S. Kholodov, V.V. Chernyshev, M.O. Tretyakova & K.S. Golokhvast
Far Eastern Federal University, Vladivostok, Russian Federation

A.S. Kholodov
Far East Geological Institute Far Eastern Branch RAS, Vladivostok, Russian Federation

K.S. Golokhvast
N.I. Vavilov All-Russian Institute of Plant Genetic Resources, Saint-Petersburg, Russian Federation

ABSTRACT: Among the multiple anthropogenic factors, air pollution is associated with the influence of pedosphere and its components on humans and environment. The disturbance of natural balance is facilitated by large-scale development of mineral deposits and associated environmental pollution by harmful components. The increasing anthropogenic impact require scientific and technical examination, introduction of air pollution monitoring systems, amendments to state regulatory acts, and practical solutions to the problems of mineral resources management. This study deals with the ecotoxicological assessment of the influence of coal dust microparticles on a typical representative of marine biota, namely mollusk *Modiolus modiolus*. We did not detect acute toxicological hazard of coal dust particles to the representatives of marine biota, however, the observed changes in the state of hemocytes of mollusk *M. modiolus* suggest that there is a chronic exposure.

1 INTRODUCTION

The port complex of Nakhodka city is located in thse southwestern part of Primorsky Krai on the shores of Nakhodka Bay and Vostok Bay, Sea of Japan. This port complex ranks first in the Russian Far East and second in Russia in terms of cargo turnover (Naumov, 2016). There is a steady dynamic in cargo turnover, from 59.6 million tons in 2012 to 80 million tons in 2015. Vostochny Port, the largest in the Far East, demonstrates annual growth in coal transshipment volumes (http://www.vostport.ru/company/statistics). Continuously growing volumes of coal transshipment (tens of millions of tons) through the port infrastructure of the Nakhodka city district, which is not designed for these purposes (no sanitary protection zones or dust suppression systems), have led to the increased emissions of coal dust into the atmosphere and degradation of the environment in the region.

The state of ambient air is one of the most significant environmental factors affecting the health of people in urban areas (Lelieveld et al., 2015; Zhang et al., 2017). However, the data on the content of nano- and microparticles of coal dust in the air of cities is insufficient. It is commonly known that particles with aerodynamic diameter of less than 200 nm settle at low speed (in mm or cm per hour), and particles less than 100 nm practically do not obey the law of gravity remaining suspended for a long time (Christian et al., 2008; Kumar et al., 2010).

The circulation of suspended particles of coal dust on the territory of enterprises and in the adjacent coastal sea water area leads to their accumulation and redistribution in the "air-human -biota-sea" system, where the air migration plays a leading role (Johnson and Bustin, 2006). The content of toxic elements in the rocks of coal-bearing strata largely determines the nature and the level of pollution of atmospheric air and water area adjacent to the transport terminals. The

most common pollutants of coals are water-soluble compounds of heavy metals, including nickel, cobalt, lead, copper, arsenic, vanadium, manganese, chromium, beryllium, molybdenum, bismuth, zinc, niobium, lithium, and fluorine (Tang et. al., 2017; Kurilenko, 2019). In earlier study, a significant content of coal dust particles was found in seawater samples from Nakhodka Bay, ranging from 7% to 53% depending on the distance from the coal terminal (Lebedev et al., 2017). The research of Pacific Oceanology Institute of the Far Eastern Branch RAS revealed that the content of petroleum products and heavy metals in the marine area of Nakhodka Bay exceeded the threshold limit values (Naumov, 2016).

Water contamination by coal cause mortality and growth inhibition of marine organisms (Gibson, 2005; Berry et al., 2016; Berry et al., 2017). A disturbance in early embryogenesis and growth inhibition of embryos and larvae were observed in all samples of developing embryos of marine mussels in Nakhodka Bay under the influence of coal-dust particles (Naumov and Naidenko, 1997). Given the continuous increase of anthropogenic pressure on the environment, practical steps are needed to timely solve the problems of pollution of the atmosphere, hydrosphere, and pedosphere by nano- and microparticles (Golokhvast et al., 2017; Honarvar and Sami, 2019; Pikula et al., 2020a).

The aim of this work is a comprehensive study of the quantitative and qualitative composition of coal dust microparticles in Nakhodka city, and assessment of the environmental impact of coal dust microparticles on representatives of marine biota. In this study, we evaluated the toxicological effects of coal dust particles on representatives of marine aquatic organisms, namely the hemocytes of marine mollusks *Modiolus modiolus*.

2 MATERIALS AND METHODS

The samples of lignite coal (grade 1B) were collected at the Novoshakhtinsk open pit mine (seam IV PK64) located in Primorsky Krai, Mikhailovsky district, Novoshakhtinsky settlement. This lignite coal is used at energy enterprises of the Primorsky Krai during the heating season and it is exported to the Asia-Pacific region countries.

Morphological analysis of coal dust particles was performed using the Malvern Morphologi G3-ID equipment (Malvern Instruments Ltd., UK). The unit features sample dispergation system and automated static imaging with chemical identification of individual particles using morphologically directed Raman spectroscopy at the resolution of 4 cm^{-1}. The analysis was performed using the diode laser with a wavelength of 785 nm and the resulting laser power of 4 mW in the low power mode. The use of micro-Raman spectroscopy made it possible to determine the size and basic chemical composition of each individual particle in samples (Kholodov, Golokhvast, 2016). Additionally, we analyzed the particle size distribution of coal in solution with the CytoFLEX flow cytometer (Beckman Coulter, USA): in the submicron range with direct light scattering of the violet laser (405 nm), and in the micron range with light scattering of the blue laser (488 nm). The cytometer was pre-calibrated with sets of particles in the ranges of 0.1–1 μm and 1–50 μm (Molecular Probes, USA).

We collected marine mollusks *M. modiolus* for the experiment in the Fedorov Bay (Vladivostok). The hemocytes of molluscs were isolated using a standard technique and incubated in 96-well plates with the addition of coal suspension. The suspension prepared by diluting a coal sample in artificial seawater was added to the mollusk hemocytes to obtain the concentrations of coal particles of 1, 10, 100, and 1000 mg/L. The control group consisted of cells in sea water without the coal particles. The experiment was repeated three times for each concentration and for the control group. All measurements were carried out after 2, 4, and 6 hours from the start of mollusk hemocytes incubation with the coal suspension.

We measured the changes in the state of cells exposed to the coal particles by the CytoFLEX flow cytometer (Beckman Coulter, USA) using fluorescent dyes. We recorded the change in the viability and integrity of cell walls, the change in the enzyme activity, and the changes in cell membrane polarization of *M. modiolus* hemocytes. The blue laser of the flow cytometer with a wavelength of 488 nm was used as a source of fluorescence excitation with all dyes. Cell size was determined by measuring the intensity of the forward scatter of blue laser (488 nm).